ATATURK
UNIVERSITY
PUBLICATIONS

Journal *of* Anatolian Physics *and* Astronomy

Official Journal of Atatürk University Faculty of Science

Volume 4 Issue 1 June 2025

EISSN 2791-8718
https://dergipark.org.tr/en/pub/japa

Journal *of* Anatolian Physics *and* Astronomy

About the Journal of Anatolian Physics and Astronomy

Journal of Anatolian Physics and Astronomy is a peer-reviewed, open-access, online-only journal published by Atatürk University.

The journal is published biannual in both Turkish, and English, with articles released in June, and December.

Abstracting and Indexing

Journal of Anatolian Physics and Astronomy is covered in the following abstracting and indexing databases;

- EBSCO
- Gale Cengage
- DOAJ

Aims

Journal of Anatolian Physics and Astronomy aims to contribute to the literature by publishing manuscripts at the highest scientific level in physics and astronomy. The journal publishes original articles, and reviews that are prepared in accordance with ethical guidelines.

Scope and Audience

The scope of the journal includes but not limited to relevant to the topics of atomic and molecular physics, condensed matter physics, nuclear physics, particle, physics, quantum physics, optical physics, biophysics, thermodynamics, astrophysics, astronomical techniques and methods, galaxies, gravitation and cosmology, planets, comets, solar and stellar physics, space and all other related interdisciplinary theoretical researches.

The target audience of the journal includes researchers and specialists who are interested or working in all fields in the journal's scope.

Disclaimer

Statements or opinions expressed in the manuscripts published in the journal reflect the views of the author(s) and not the opinions of the editors, editorial board, and/or publisher; the editors, editorial board, and publisher disclaim any responsibility or liability for such materials.

Open Access Statement

You can find the current version of the Instructions to Authors at https://dergipark.org.tr/en/pub/japa/writing-rules

Contact (Editor in Chief) / İletişim (Baş Editör)
Melek FİDAN
Science Faculty, Department of Physics,
Atatürk University, Erzurum, Turkey
Fen Fakültesi, Fizik Bölümü, Atatürk Üniversitesi,
Erzurum, Türkiye
✉ mbahadir@atauni.edu.tr
✉ japa@atauni.edu.tr
🌍 https://dergipark.org.tr/en/pub/japa
☎ +90 442 231 40 76

Contact (Publisher) / İletişim (Yayıncı)
Atatürk University
Atatürk University, Erzurum, Turkey
Atatürk Üniversitesi Rektörlüğü 25240 Erzurum, Türkiye
✉ ataunijournals@atauni.edu.tr
🌍 https://bilimseldergiler.atauni.edu.tr
☎ +90 442 231 15 16

Journal of Anatolian Physics and Astronomy Hakkında

Journal of Anatolian Physics and Astronomy, Atatürk Üniversitesi tarafından yayınlanan hakemli, açık erişimli, yalnızca çevrimiçi bir dergidir.

Dergi, Haziran ve Aralık aylarında olmak üzere Türkçe ve İngilizce olarak yılda iki kez yayınlanmaktadır.

Özetleme ve İndeksleme

Journal of Anatolian Physics and Astronomy aşağıdaki özetleme ve indeksleme veri tabanlarında yer almaktadır:

- EBSCO
- Gale Cengage
- DOAJ

Amaç

Journal of Anatolian Physics and Astronomy, fizik ve astronomi alanında en yüksek bilimsel düzeyde makaleler yayınlayarak literatüre katkıda bulunmayı amaçlamaktadır. Dergide etik kurallara uygun olarak hazırlanmış özgün makaleler ve derlemeler yayınlanmaktadır.

Kapsam ve Hedef Kitle

Derginin kapsamına atom ve moleküler fizik, yoğun madde fiziği, nükleer fizik, parçacık, fizik, kuantum fiziği, optik fizik, biyofizik, termodinamik, astrofizik, astronomik teknik ve yöntemler, galaksiler, galaksiler, yerçekimi ve kozmoloji, gezegenler, kuyruklu yıldızlar, güneş ve yıldız fiziği, uzay ve ilgili tüm disiplinler arası teorik araştırmalar girmektedir.

Derginin hedef kitlesi, derginin kapsamına giren tüm alanlarla ilgilenen veya çalışan araştırmacı ve uzmanları içermektedir.

Sorumluluk Reddi

Dergide yayınlanan yazılarda ifade edilen ifadeler veya görüşler, editörlerin, yayın kurulunun ve/veya yayıncının görüşlerini değil, yazar(lar)ın görüşlerini yansıtır; editörler, yayın kurulu ve yayıncı bu tür materyaller için herhangi bir sorumluluk veya yükümlülük kabul etmemektedir.

Açık Erişim Bildirimi

Yazarlara Bilgi'nin güncel versiyonuna https://dergipark.org.tr/tr/pub/japa/writing-rules adresinden ulaşabilirsiniz.

Contact (Editor in Chief) / İletişim (Baş Editör)
Melek FİDAN
Science Faculty, Department of Physics,
Atatürk University, Erzurum, Turkey
Fen Fakültesi, Fizik Bölümü, Atatürk Üniversitesi, Erzurum, Türkiye
mbahadir@atauni.edu.tr
japa@atauni.edu.tr
https://dergipark.org.tr/en/pub/japa
+90 442 231 40 76

Contact (Publisher) / İletişim (Yayıncı)
Atatürk University
Atatürk University, Erzurum, Turkey
Atatürk Üniversitesi Rektörlüğü 25240 Erzurum, Türkiye
ataunijournals@atauni.edu.tr
https://bilimseldergiler.atauni.edu.tr
+90 442 231 15 16

CONTENTS / İÇİNDEKİLER

Research Articles/Araştırma Makaleleri

ATATÜRK ÜNİVERSİTESİ YAYINLARI
ATATURK UNIVERSITY PUBLICATIONS

Research Article *Araştırma Makalesi* DOI: 10.5281/zenodo.15739317

Investigation of The Standardization Method with Scattered X-Rays in Matrices Prepared with Different Diluters

Farklı Seyrelticilerle Hazırlanan Matrislerde Saçılan X-Işınları ile Standardizasyon Yönteminin İncelenmesi

Adem KORKMAZ
Department of Physics, Faculty of Sciences, Atatürk University, Erzurum, Türkiye

Demet YILMAZ
Department of Physics, Faculty of Sciences, Atatürk University, Erzurum, Türkiye

Abstract

In this study, it is considered to evaluate the spectral intensity ratios for different matrices to be prepared using MnO_2 and boric acid, sugar, starch, and cellulose as binders. The areas under the Compton and coherent scattering peaks with Mn Kα x-ray were calculated, and the relationship between different intensity ratios and the mean atomic number of diluted samples was investigated. 100 mCi Am-241 point radioactive source was used to excite the targets. The emitted and scattered x-rays from targets were counted by a ULEGe detector. The changes in the scattering intensity ratios of the mean atomic numbers of the matrices prepared using different diluters were plotted graphically, and the calibration curves and correlation coefficients obtained were interpreted. In addition, there is a third-degree polynomial relationship between $I_{coh}+I_{Comp}/(\mu/\rho)_{(K\alpha)}$ intensity ratio of the prepared sample group and mean atomic number. The obtained calibration curves can be used for qualitative analysis in sample groups with the same matrix.

Keywords: Qualitative analysis, Normalized scattering intensities, EDXRF, ULEGe detector.

Öz

Bu çalışmada, MnO_2 ile bağlayıcı olarak borik asit, şeker, nişasta ve selüloz kullanılarak hazırlanan farklı matrisler için spektral şiddet oranlarının değerlendirilmesi amaçlanmıştır. Mn Kα x-ışını piki ile Compton ve koherent saçılmış piklerin altındaki alanlar hesaplanarak farklı şiddet oranları ile seyreltilen numunelerin ortalama atom numarası arasındaki ilişki incelenmiştir. Hedefleri uyarmak için 100 mCi Am-241 nokta radyoaktif kaynak kullanılmıştır. Numunelerden yayınlanan ve saçılan x-ışınları ULEGe dedektörü ile sayılmıştır. Farklı seyrelticilerle hazırlanan matrislerin ortalama atom numaralarına göre saçılma şiddet oranlarındaki değişimler grafiksel olarak elde edilmiş, kalibrasyon eğrileri ve korelasyon katsayıları yorumlanmıştır. Ayrıca, hazırlanan numune grubunun $I_{coh}+I_{Comp}/(\mu/\rho)_{(K\alpha)}$ şiddet oranı ile ortalama atom numarası arasında üçüncü dereceden polinomal bir ilişki olduğu belirlenmiştir. Elde edilen kalibrasyon eğrileri, aynı matris yapısına sahip numune gruplarında kalitatif analiz amacıyla kullanılabilir.

Anahtar Kelimeler: Kalitatif analiz, Normalize edilmiş saçılma şiddetleri, EDXRF, ULEGe dedektör.

Sorumlu Yazar/Corresponding Author: Demet Yılmaz
E-mail: ddemir@atauni.edu.tr

Geliş Tarihi/Received 02.02.2025
Kabul Tarihi/Accepted 08.05.2025
Yayın Tarihi/ Publication Date 27.06.2025

Cite this article
Kormaz A. & Yılmaz D. (2025) Investigation of the standardization method with scattered x-rays in matrices prepared with different dilutere. *Journal of Anatolian Physics and Astronomy,* 4(1), 1-12.

Introduction

The main principles of sample preparation technique in XRF are: reproducibility, sensitivity, simplicity, cheapness, and reliability. The proper placement of the sample is usually sufficient for qualitative X-ray spectrometric analysis. There are many parameters in the study of alloys, glasses, cements, polymers, and geological materials that have been fused, pressed, or assessed untreated. In these analyses, X-ray fluorescence spectrometry (XRF) is frequently used.

Additions to the sample, absorption, and scattering effects can be controlled by diluting the sample if they are high. When binders or diluents are used, unbound binders provide better homogeneity in irregular particle sizes and densities. It provides high packing density and a smooth surface and reduces absorption and scattering effects by dilution. Disadvantages of the binder are that light elements may have absorbing effects on analyte intensity and may give high background count due to scattering effects. Therefore, binder should be used in a minimum amount (sample should not be bound to a pure binder tray or holder). Standardization method with scattered X-rays provides compensation for tailing regions originating from multiple scattering and especially located in low energy regions of Compton scattering peaks in XRF. In addition, intensity ratios of characteristic and scattering peaks also correct the geometry factor affecting the counting efficiency of the detector. Determination of the effect of different binders used in XRF on intensity ratios of characteristic and scattering peaks will be an achievement for the literature. The purpose of determining the effect of the binders used in XRF analyses on the intensity ratios of characteristic and scattering peaks is to increase the accuracy and reliability of the measurements, to make the analysis results more precise and reliable, to improve the calibration and standardization processes of XRF devices and to ensure that the devices provide consistent results in different sample types. In addition, the compensation of tailing regions and multiple scattering in low-energy regions increases the measurement sensitivity and provides an advantage in the detection of low-concentration elements. The study contributes to the development of XRF analysis methods, enables the development of new binders and analysis techniques, and expands the applications in different industries. It provides a significant contribution to academic literature and industrial applications, and provides great benefits in XRF analyses used in fields such as material science, chemistry, and geology. More accurate and reliable analyses reduce the need for re-measurements, provide cost and time savings, and increase the efficiency of laboratories and industrial facilities. These justifications clearly show why it is important to examine the effect of the different binders used in XRF analyses on the intensity ratios of characteristic and scattering peaks and how this study will contribute to the literature.

In the literature, there are studies by absorption correction methods in XRF (Mantouvalou, 2017). Bauer developed the absorption correction approach (Bauer et al., 2024). This method makes it possible to investigate the diffusion of elements at the tooth-filling contact in three dimensions with greater accuracy. The mass absorption coefficient is used in the model. Rousseau (2006) created a mathematical adjustment for matrix effects in the analysis of X-ray fluorescence. Bowers (2019) used a simple influence factor model to rectify the matrix effect. Chebakova et al. (2021) investigated XRF properties of micro- and nanoscale particle compositions. The authors' quantitative analytical results depend on the thickness, morphology, and characteristics of the coatings. When analyzing heterogeneous materials, so-called particle size effects may be the cause of a substantial mistake. When examining samples with drastically diverse particle size distributions and light components, extreme results can even be >30% relative. In the microscale region, X-ray fluorescence intensity rose as particle size shrank (Finkel'shtein & Gunicheva, 2008). Sitko (2009) investigated matrix effects in samples of less than infinite thickness. Yılmaz and Boydaş (2018) studied the scattering peaks for matrix effect correction in WDXRF analysis. For quantitative X-ray spectrometry, Uzunoğlu et al. (2015) suggested employing the characteristic and scattering peaks. Tee et al. (2024) studied the method to fit Compton profiles in X-ray fluorescence (XRF) spectroscopy. In assessing the areas under the Compton peaks acquired at various energies, researchers in this work underlined the significance of identifying the background region and its energy dependence. The background form of an XRF spectrum and the line shape of the fluorescence peaks may also be influenced by the scattered X-rays, as a very small fraction of fluorescent X-rays scatter in the sample or instrument before they reach the detector. A model for Compton peaks in energy-dispersive X-ray fluorescence spectra was created by Van Gysel et al. (2003). The model uses Monte Carlo simulations to systematically investigate peak morphology. Perez et al. (2024) looked into wine adulteration using the effective atomic number and the Compton/Rayleigh intensity ratio. Büyükyıldız (2016) determined effective atomic numbers (Z_{eff}) of Fe_xCu_{1-x} binary ferro alloys by using the Rayleigh to Compton scattering ratio. Hodoroaba and Rackwitz (2014) used the Compton to Rayleigh intensity ratio, which has a high specificity to the mean atomic number, to obtain additional information about the chemical composition of the sample using XRF).

In this work, we used the scattered peak ratio method. It is planned to evaluate the spectral intensity ratios for different matrices to be prepared using the oxidized compound (MnO_2) of an element with medium atomic number and boric acid, sugar, starch and cellulose as binders. The calibration curves drawn from the intensity ratios $I_{sc_{(K\alpha)}} = I_{coh}/2(\mu/\rho)_{K_{\alpha_1}} + I_{Comp}/2(\mu/\rho)_{K_{\alpha_1}} + (\mu/\rho)_{59,54}$ and $(\mathrm{I_{coh}} + \mathrm{I}_{Comp})/(\mu / \rho)_{K_\alpha}$ versus mean atomic number in EDXRF system. Targets of various concentrations were excited by 59.54 keV γ-rays from a 100 mCi Am-241 point radioactive source. The emitted and scattered X-rays by samples were counted by an ULEGe detector.

Experimental

In this study, a conical lead collimator was used to provide the source and detector to see the sample in the 45^o geometry in Figure 1. The experimental system used includes a ULEGe (Ultra Low Energy Germanium Detector), and the photograph of the experimental system is shown in Figure 2. The physical and electrical characteristics of the ULEGe detector is given in Table 1. The hydraulic press used in the production of the samples is given. The samples were pressed using a 13 mm die set using 7 tons of pressure. A spectrum taken from a MnO_2 sample diluted with H_3BO_3 in the EDXRF system is given in Figure 3. The radioactive source used is a 100 mCi Am-241 source.

Table 1. Physical and electrical characteristic of the ULEGe detector

Window	Beryllium; 25 µm
Energy resolution (FWHM)	140 eV at 5.9 keV, 520 eV at 122 keV
Active diameter	8 mm
Active area	50 mm^2
Thickness	5 mm
Distance from window	5 mm
Bias voltage	-500 Vdc
Depletion voltage	-300 Vdc

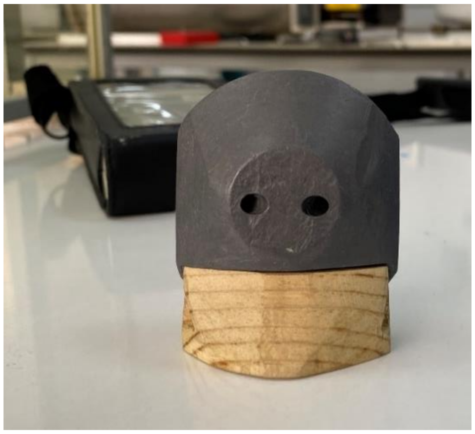

Figure 1. Lead collimator.

Figure 2. Experimental system.

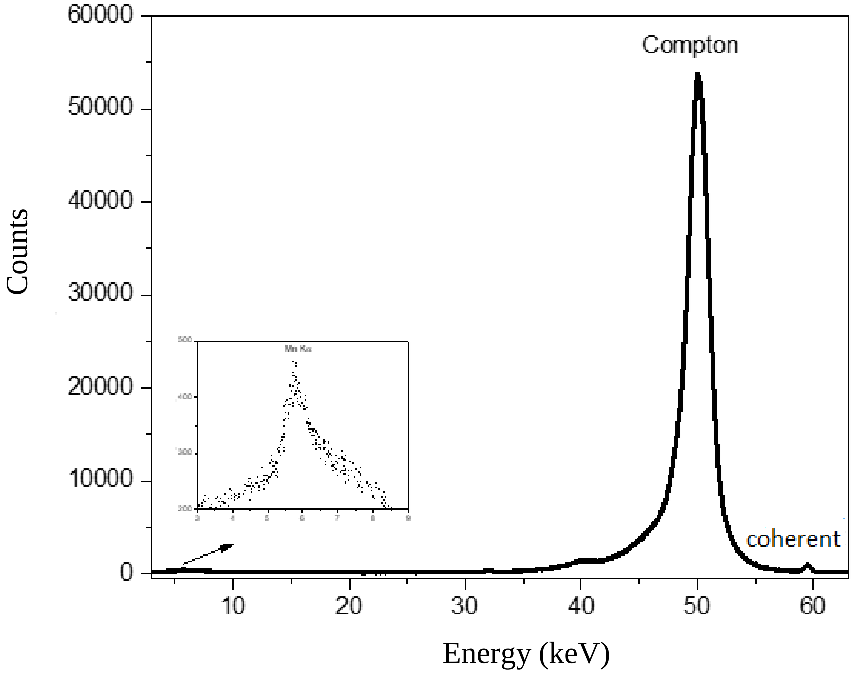

Figure 3. The XRF spectrum of MnO_2 diluted by H_3BO_3.

Preparation of samples

In this study, the chemical compound MnO_2 was diluted with sugar, starch, cellulose and boric acid using the dilution technique. Samples with different mean atomic numbers were obtained with each diluent. The mean atomic number of the diluents used is found with the expression

$$\bar{Z}_c = \frac{\sum_i n_i Z_i}{n} \tag{1}$$

where n is the total number of atoms in the diluent, n_i is the atomic number of the ith element in the diluent, and Z_i is the atomic number of the ith element in the diluent. The percentage concentrations of the diluent forming the sample and the chemical compound used (MnO_2) were calculated with the expression:

$$C_{b(c)}\% = \frac{m_{b(c)}}{m_b+m_c} \times 100 \tag{2}$$

where m_b is the mass of the compound and m_c is the mass of the diluent. The mean atomic number of the samples can be calculated from the expression:

$$\bar{Z}_s = \bar{Z}_b \times C_b + \bar{Z}_c \times C_c \tag{3}$$

Here, $\bar{Z}_s$ is the mean atomic number of the sample, $\bar{Z}_b$ and $\bar{Z}_c$ are the mean atomic number of the compound and diluent used, C_b and C_c are the percentage concentrations of the compound and diluent. The mass amounts, percentage concentrations, sample thicknesses, and mean atomic numbers of the samples prepared with the MnO_2 compound diluted with fourteen different diluents to be used in the study are given in Tables 2 -5. The total scattered intensity at a specific wavelength is expressed as follows (E.P. Bertin, 1975):

$$I_{sc} = \frac{I_{coh}}{2(\mu/\rho)_\lambda} + \frac{I_{Comp}}{2(\mu/\rho)_\lambda+(\mu/\rho)_{\lambda-\Delta\lambda}} \tag{4}$$

I_{coh} ve I_{Comp} in the expression indicate the areas under the coherent and Compton peaks. $(\mu/\rho)_\lambda$ is the mass absorption coefficient of the sample at a specific wavelength (e.g. K_α) and $(\mu/\rho)_{\lambda-\Delta\lambda}$) is the mass absorption coefficient of the sample at the excitation photon energy. In this work, the total scattering intensity was calculated.

$$I_{sc(K\alpha)} = \frac{I_{coh}}{2(\mu/\rho)_{K\alpha_1}} + \frac{I_{Comp}}{2(\mu/\rho)_{K\alpha_1}+(\mu/\rho)_{59,54}} \tag{5}$$

In addition, the intensity ratios $(\mathrm{I_{coh}} + \mathrm{I}_{Comp})/(\mu/\rho)_{K_\alpha}$ were also calculated. The mass absorption coefficients of the samples prepared at a specific X-ray energy were calculated from the EpiXS program (Hila et al., 2021). The changes in the mean atomic number and scattering intensity of the samples obtained with the MnO_2 compound diluted with different diluents are given in Figure 4-11.

Table 2. The properties of prepared samples (MnO_2/H_3BO_3)

Sample No	m_b (g)	m_c (g)	C_b (%)	C_c (%)	Mass Thickness (g/cm²)	$(\mu/\rho)_{6\ keV}$ (cm²/g)	$(\mu/\rho)_{59.54\ keV}$ (cm²/g)	$\bar{Z}_s$
1	0.60	0.00	1.00	0.00	0.93	5.62	0.755	13.66
2	0.57	0.03	0.95	0.05	0.99	5.45	0.727	12.32
3	0.54	0.06	0.90	0.10	1.00	5.29	0.699	11.23
4	0.51	0.09	0.85	0.15	0.97	5.11	0.671	10.33
5	0.48	0.12	0.80	0.20	1.00	4.95	0.643	9.030
6	0.00	0.60	0.75	0.25	2.60	4.78	0.615	4.090

Table 3. The properties of prepared samples (MnO_2/starch)

Sample No	m_b (g)	m_c (g)	C_b (%)	C_c (%)	Mass Thickness (g/cm²)	$(\mu/\rho)_{6\ \mathrm{keV}}$ (cm²/g)	$(\mu/\rho)_{59.54\ \mathrm{keV}}$ (cm²/g)	$\bar{Z}_s$
1	0.60	0.00	1.00	0.00	0.93	5.62	0.755	13.66
2	0.57	0.03	0.95	0.05	0.96	5.44	0.727	11.31
3	0.54	0.06	0.90	0.10	0.96	5.25	0.699	10.85
4	0.51	0.09	0.85	0.15	0.94	5.09	0.671	9.880
5	0.48	0.12	0.80	0.20	0.55	4.88	0.643	9.220
6	0.00	0.60	0.75	0.25	2.40	4.69	0.615	4.090

Table 4. The properties of prepared samples (MnO_2/sugar)

Sample No	m_b (g)	m_c (g)	C_b (%)	C_c (%)	Mass thickness (g/cm²)	$(\mu/\rho)_{6\ \mathrm{keV}}$ (cm²/g)	$(\mu/\rho)_{59.54\ \mathrm{keV}}$ (cm²/g)	$\bar{Z}_s$
1	0.60	0.00	1.00	0.00	0.93	5.62	0.755	13.66
2	0.57	0.03	0.95	0.05	1.00	5.44	0.727	11.31
3	0.54	0.06	0.90	0.10	1.00	5.25	0.699	10.85
4	0.51	0.09	0.85	0.15	0.88	5.09	0.671	9.880
5	0.48	0.12	0.80	0.20	0.96	4.88	0.643	9.220
6	0.00	0.60	0.75	0.25	2.00	4.69	0.615	4.090

Table 5. The properties of prepared samples (MnO_2/cellulose)

Sample No	m_b (g)	m_c (g)	C_b (%)	C_c (%)	Mass thickness (g/cm²)	$(\mu/\rho)_{6\ \mathrm{keV}}$ (cm²/g)	$(\mu/\rho)_{59.54\ \mathrm{keV}}$ (cm²/g)	$\bar{Z}_s$
1	0.60	0.00	1.00	0.00	0.93	5.62	0.755	13.66
2	0.57	0.03	0.95	0.05	0.77	5.43	0.727	11.31
3	0.54	0.06	0.90	0.10	1.00	5.25	0.699	10.85
4	0.51	0.09	0.85	0.15	0.78	5.06	0.671	9.880
5	0.48	0.12	0.80	0.20	0.69	4.87	0.643	9.220
6	0.00	0.60	0.75	0.25	3.00	4.68	0.615	4.090

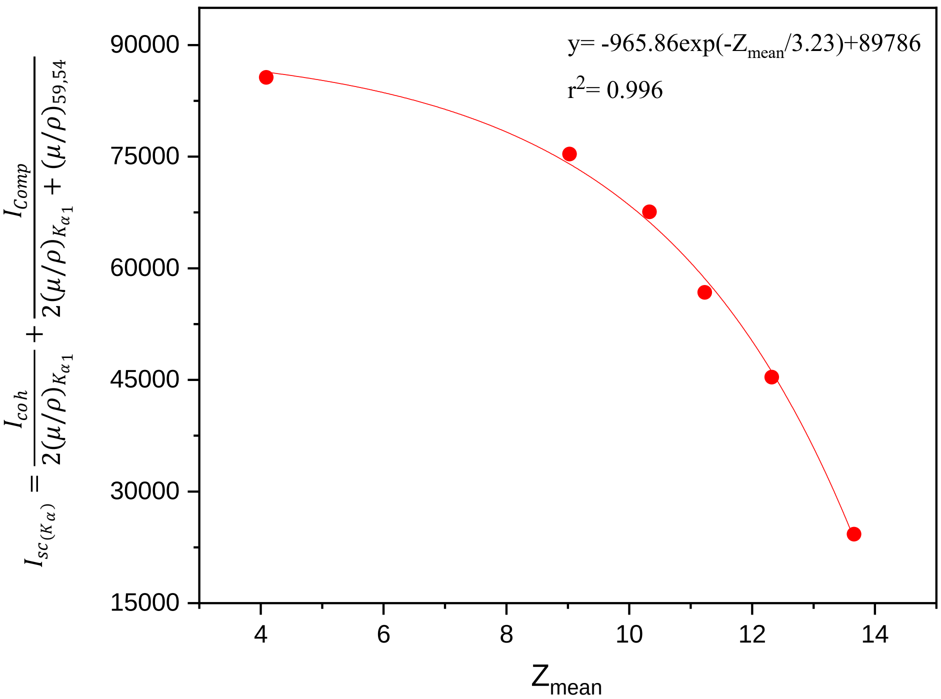

Figure 4. Variation of the total scattering intensity ratio with the mean atomic number for the MnO_2/H_3BO_3 sample group.

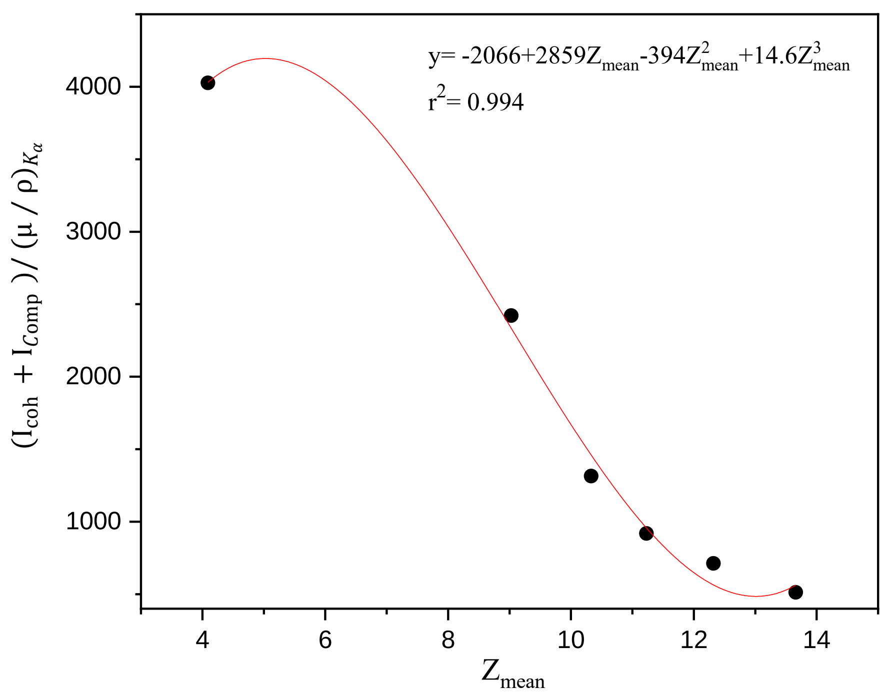

Figure 5. Variation of the intensity ratio $(I_{coh}+I_{Comp})/(\mu/\rho)_{(K\alpha)}$ with the mean atomic number for the MnO_2/H_3BO_3 sample group.

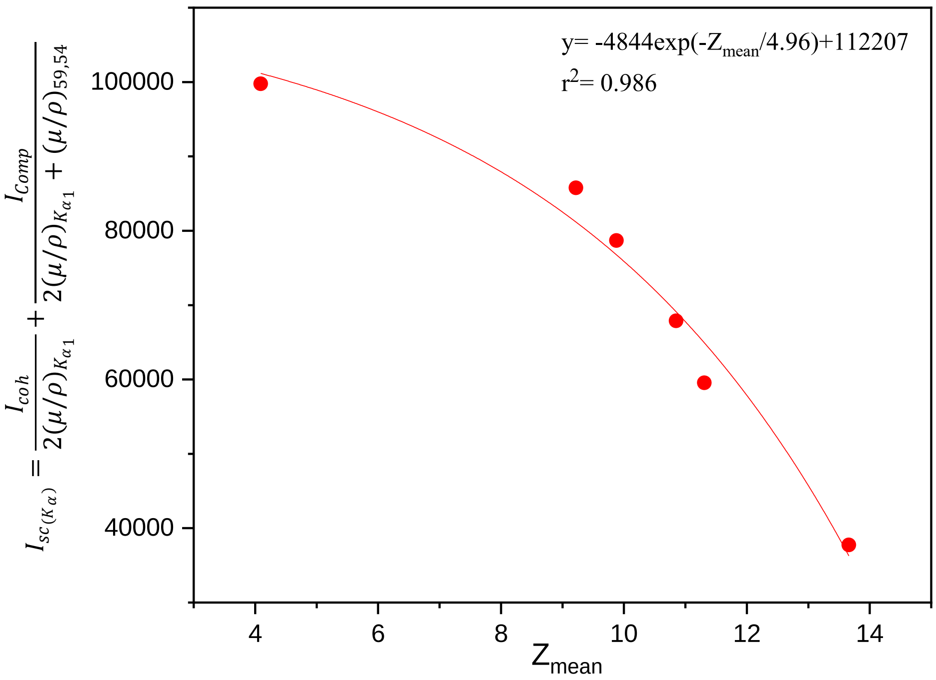

Figure 6. Variation of the total scattering intensity ratio with the mean atomic number for the MnO_2/starch sample group.

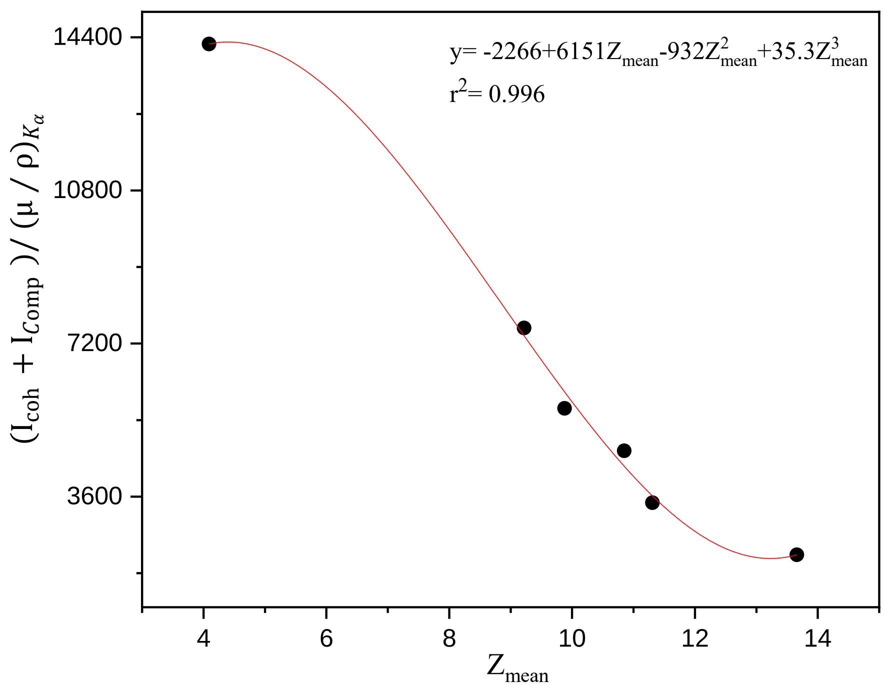

Figure 7. Variation of the intensity ratio $(I_{coh}+I_{Comp})/(\mu/\rho)_{(K\alpha)}$ with the mean atomic number for the MnO_2/starch sample group.

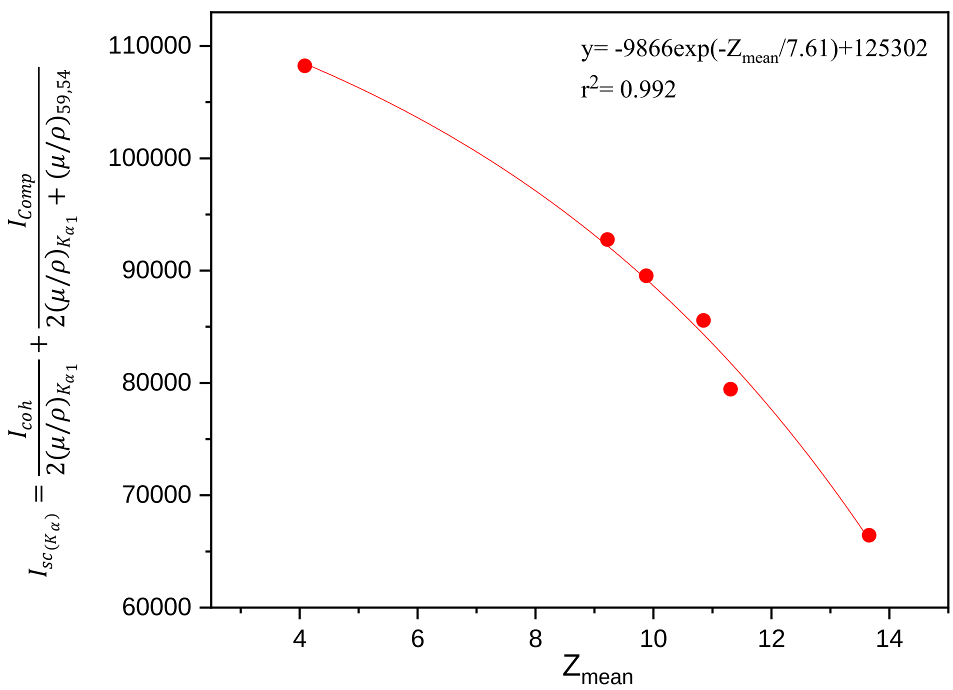

Figure 8. Variation of the total scattering intensity ratio with the mean atomic number for the MnO_2/sugar sample group.

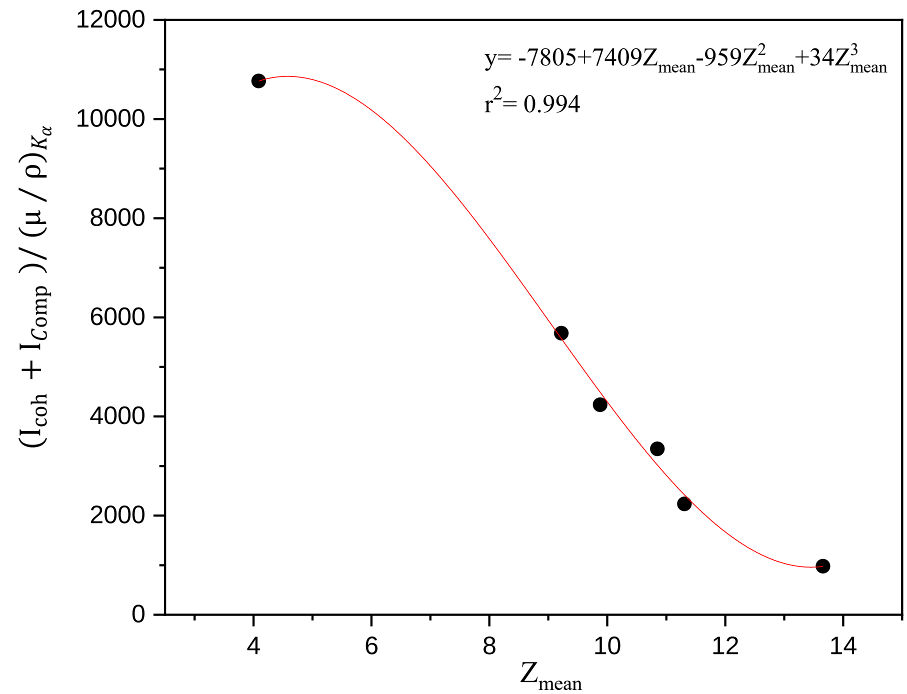

Figure 9. Variation of the intensity ratio $(I_{coh}+I_{Comp})/(\mu/\rho)_{(K\alpha)}$ with the mean atomic number for the MnO_2/sugar sample group.

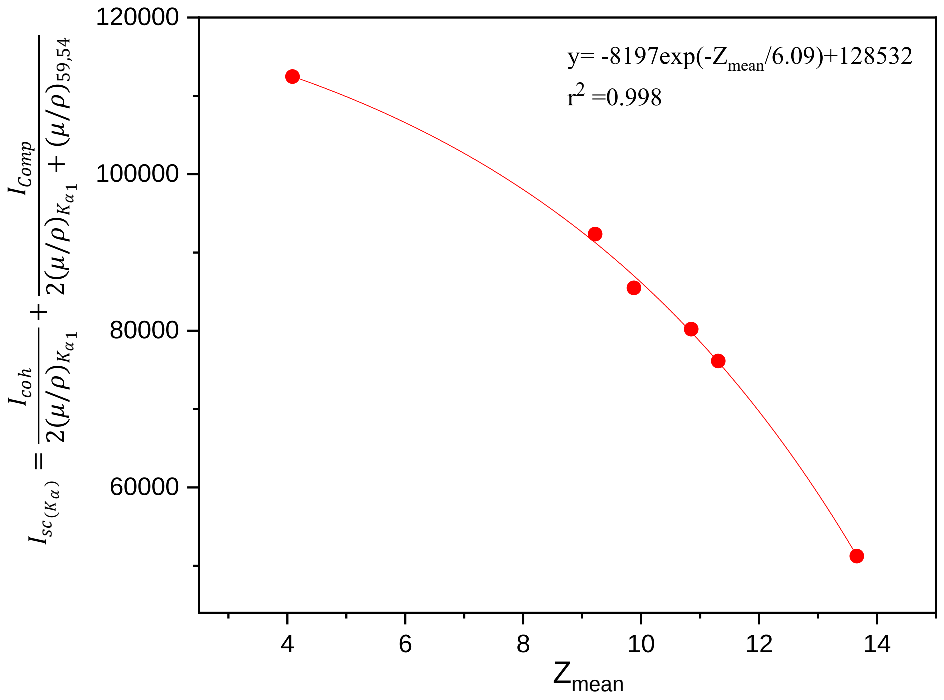

Figure 10. Variation of the total scattering intensity ratio with the mean atomic number for the MnO_2/cellulose sample group.

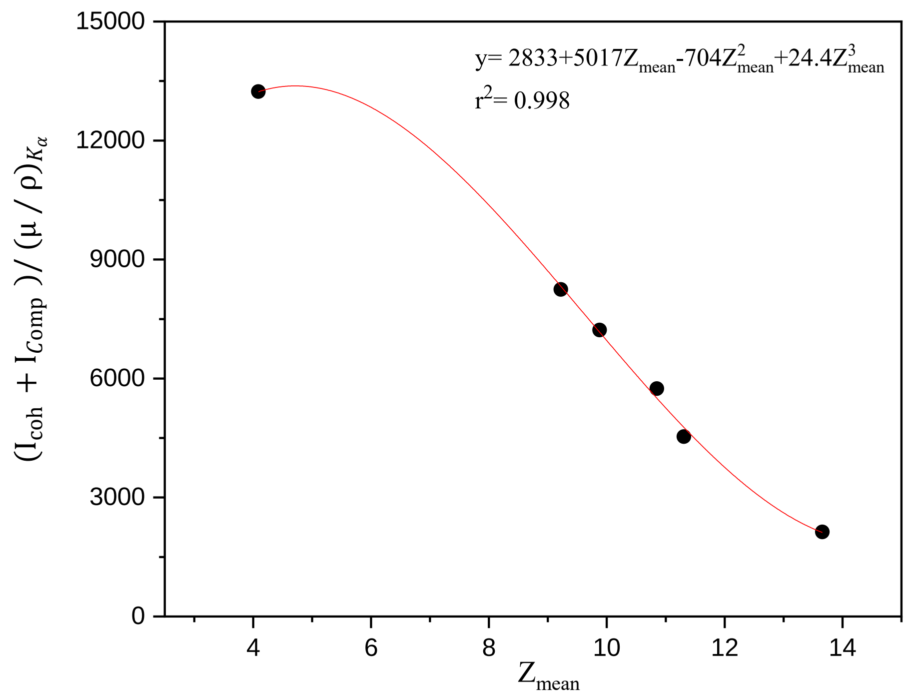

Figure 11. Variation of the intensity ratio $(I_{coh}+I_{Comp})/(\mu/\rho)_{(K\alpha)}$ with the mean atomic number for the MnO_2/cellulose sample group.

Results and Discussion

The main principles of sample preparation technique in XRF are reproducibility, sensitivity, simplicity, cheapness, and rapidity. For qualitative X-ray spectrometric analysis, it is usually sufficient to place the sample in the appropriate place. However, for quantitative analysis, many conditions and methods are important in preparation and form. For example, sample errors (homogeneity, surface texture, particle size, and inhomogeneity in distribution, amount of porosity, surface representativeness of the sample, etc.) should be reduced. Additions should be made to the sample. If absorption-intensification effects are high, internal standards should be added, matrix masking agents should be added, or the sample should be diluted, internal control standards or intensity-reference standards should be added, or standard-addition or standard-dilution methods should be used. The sample dilution method was used in this study. Binders that can be used in XRF to reduce absorption and amplification effects or to compensate for deviations from linearity that may arise from these effects are given in the literature as cellulose, Li_2CO_3, boric acid (H_3BO_3), carbon, stearic acid ($C_{17}H_{35}COOH$), polyvinyl alcohol (PVA), commercial soap and detergent powders, Al, starch, sugar and filter or chromatographic paper. Binders should be used as little as possible, and their addition to the sample should not exceed 5-20%. Based on this literature information, in this study, cellulose, boric acid (H_3BO_3), starch, and granulated sugar were used as binders in order to create different matrices with MnO_2 compound. The effect of binders on scattering and characteristic peaks was investigated using different peak ratio methods (standardization with scattered X-rays) against the mean atomic number. When Figure 4, 6, 8 and 10, where the changes in the total scattering intensity ratio in Mn Kα energy with the mean atomic number are given for the MnO_2/H_3BO_3, MnO_2/starch, MnO_2/sugar and MnO_2/cellulose sample groups, are examined, it is seen that there is an exponential relationship between the total scattering intensity ratios and the mean atomic number of the formed samples and this relationship is compatible with the correlation coefficient given in the graphs. However, when Figure 5, 7, 9 and 11, where the changes in the $(\mathrm{I_{coh}} + \mathrm{I}_{Comp})/\,(\mu\,/\,\rho)_{K_\alpha}$ intensity ratio with the mean atomic number are given for the MnO_2/H_3BO_3, MnO_2/starch, MnO_2/sugar and MnO_2/cellulose sample groups, are examined, it is seen that there is a third-degree polynomial relationship between the total scattering intensity ratios and the mean atomic number of the formed samples and this relationship is compatible with the correlation coefficients given in the graphs. The correlation coefficients obtained show that the relevant calibration curves can be used in qualitative analyses.

While preparing the sample, the smaller particles with the same density are located at the bottom. The binders used in this study were sieved to minimize the errors that will come from the particle size effect. Since a light matrix sample was created, it was not possible to look at the L_α/K_α or M_α/K_α intensity ratios of the samples given in the literature. However, it is an achievement for the literature to determine that the particle size effect is minimized in light matrix samples by looking at the characteristic and scattering peak intensity ratios ($I_{K\alpha}/I_{Comp}$).

Conclusion

All binders used in this study are organic structures composed of light elements. Compton scattering is always dominant in light elements. The additional concentration of the binder added to the samples should not exceed 20%, which is known in the literature. In the study, Mn Kα and Compton scattering peak intensity ratios were controlled at each dilution stage. Since the increase in binder concentration will increase the amplification effect in the sample, this will bring an unwanted error to the spectra in XRF analyses. Although binders other than H_3BO_3 have the same chemical structure ($C_6H_{10}O_5$), their crystal structures are different, so their packing fractions are different from each other. Although the briquetting pressure was kept the same in all samples in this study, the changing intensity ratios show that the analyte-line intensity measured in the diluted samples changes with the sample packing fraction of the measured wavelength path length. The existence of this effect in compounds with the same chemical structure was revealed in the same matrix samples prepared by the dilution method. In XRF, there is a concentration range where the binder types used are effective in analyte line intensity, such that the analyte-line intensity increases with decreasing particle size at a given briquetting pressure, and the intensity increases with increasing briquetting pressure at the same particle size. This makes a significant contribution to the analyte intensification effect of the sample. However, since the software programs that give absorption coefficients do not contain physical information about chemical bonds, although they give the same absorption coefficient value to similar chemical structures, the fact that different contributions are obtained in intensity ratios in the examination of XRF spectra also points to the deficiency in the existing programs.

Hakem Değerlendirmesi: *Dış bağımsız.*
Yazar Katkıları: *Fikir-DY; Tasarım-DY; Denetleme DY-; Kaynaklar-AK; Veri Toplanması ve/veya İşlemesi AK; Analiz ve/ veya Yorum DY; Literatür Taraması AK; Yazıyı Yazan-DY; Eleştirel İnceleme-DY.*
Çıkar Çatışması: *Yazarlar, çıkar çatışması olmadığını beyan etmiştir.*
Finansal Destek: *Bu çalışma için herhangi bir kurumdan finansal destek alınmamıştır.*
Peer-review: *Externally peer-reviewed.*
Author Contributions: Concept - DY; Design - DY; Supervision - DY; Resources - DY; Materials - AK; Data Collection and/or Processing - AK; Analysis and/or Interpretation - DY; Literature Search - AK; Writing Manuscript - DY; Critical Review - DY;
Conflict of Interest: *The authors have no conflicts of interest to declare.*
Financial Disclosure: *No financial support was received from any institution for this study.*

References

Bauer, L.J., Wieder, F., Truong, V., Förste, F., Wagener, Y., Jonas, A., Praetz, S., Schlesiger, C., Kupsch, A., Müller, B.R., Kanngießer, B., Zaslansky, P. & Mantouvalou, I. (2024). Absorption Correction for 3D Elemental Distributions of Dental Composite Materials Using Laboratory Confocal Micro-X-ray Fluorescence Spectroscopy. *Analytical Chemistry*, 96, 8441–8449. https://doi.org/10.1021/acs.analchem.4c00116.

Bowers, C. (2019). Matrix Effect Corrections in X-ray Fluorescence Spectrometry. *Journal of Chemical Education,* 96, 2597–2599. https://doi.org/10.1021/acs.jchemed.9b00630.

Büyükyıldız, M. (2016). Determination of the effective atomic numbers of Fe_xCu_{1-x} binary ferroalloys using a nondestructive technique: Rayleigh-to-Compton scattering ratio. *Turk J. Phys.,* 40, 278-286. 10.3906/fiz-1603-25.

Bertin, E.P. (1975). Principles and Practice of X-Ray Spectrometric Analysis. Plenum Press.

Chebakova, K.A., Dzidziguri, E.L., Sidorova, E.N., Vasiliev, A.A., Ozherelkov, D.Y., Pelevin, I.A., Gromov, A.A. & Nalivaiko, A.Y. (2021). X-ray Fluorescence Spectroscopy Features of Micro- and Nanoscale Copper and Nickel Particle Compositions. *Nanomaterials,* 11, 2388. https://doi.org/10.3390/nano11092388.

Finkel'shtein, A.L. & Gunicheva, T.N. (2008). Description of the dependence of intensity of x-ray fluorescence on the particle size of powder samples and pulp during x-ray fluorescent analysis. *Inorganic Materials,* 44, 1567–1571. https://doi.org/10.1134/S0020168508140136.

Hila, F.C., Asuncion-Astronomo, A., Dingle, C.A.M., Jecong, J.F.M., Javier-Hila, A.M. V., Gili, M.B.Z., Balderas, C. V., Lopez, G.E.P., Guillermo, N.R.D. & Amorsolo, A. V. (2021). EpiXS: A Windows-based program for photon attenuation, dosimetry and shielding based on EPICS2017 (ENDF/B-VIII) and EPDL97 (ENDF/B-VI.8). *Radiation Physics and Chemistry,* 182, 109331. https://doi.org/10.1016/j.radphyschem.2020.109331.

Hodoroaba, V.D. & Rackwitz, V. (2014). Gaining improved chemical composition by exploitation of Compton-to-Rayleigh intensity ratio in XRF analysis. *Anal. Chem.,* 86, 6858-6864. https://doi.org/10.1021/ac5000619.

Mantouvalou, I., Lachmann, T., Singh, S.P., Vogel-Mikuš, K. & Kanngießer, B. (2017). Advanced Absorption Correction for 3D Elemental Images Applied to the Analysis of Pearl Millet Seeds Obtained with a Laboratory Confocal Micro X-ray Fluorescence Spectrometer. *Analytical Chemistry,* 89, 5453–5460. https://doi.org/10.1021/acs.analchem.7b00373.

Pérez, S., Vasquez, R., Pascual, G., Araya, J., Neira, J. & Cespedes-Acuña, C.L. (2024). Toward the authentication of wines of Itata valley denomination of origin through total reflection x-ray fluorescence (TXRF) method for testing adulteration. A novel valuable tool by using Compton/Rayleigh scattering signals in wines. *Food Bioscience,* 61, 104475. https://doi.org/10.1016/j.fbio.2024.104475.

Rousseau, R.M. (2006). Corrections for matrix effects in X-ray fluorescence analysis—A tutorial. *Spectrochimica Acta Part B: Atomic Spectroscopy,* 61, 759–777. https://doi.org/10.1016/j.sab.2006.06.014.

Sitko, R. (2009). Quantitative X-ray fluorescence analysis of samples of less than 'infinite thickness': Difficulties and possibilities. *Spectrochimica Acta Part B: Atomic Spectroscopy,* 64, 1161–1172. https://doi.org/10.1016/j.sab.2009.09.005.

Tee, B.P.E., Ganly, B., McIlquham, J.D., Giang, P. & Van Haarlem, Y. (2024). Fitting Compton peaks from first principles in x-ray fluorescence spectra. *X-Ray Spectrometry*, https://doi.org/10.1002/xrs.3441.

Uzunoğlu, Z., Yilmaz, D. & Şahin, Y. (2015). Quantitative x-ray spectrometric analysis with peak to Compton ratios. *Radiation Physics and Chemistry,* 112. https://doi.org/10.1016/j.radphyschem.2015.03.039.

Van Gysel, M., Lemberge, P. & Van Espen, P. (2003). Description of Compton peaks in energy-dispersive x-ray fluorescence spectra. *X-Ray Spectrometry,* 32, 139–147. https://doi.org/10.1002/xrs.628.

Yılmaz, D. & Boydaş, E. (2018). The use of scattering peaks for matrix effect correction in WDXRF analysis. *Radiation Physics and Chemistry,* 153, 17–20. https://doi.org/10.1016/j.radphyschem.2018.08.035.

ATATÜRK ÜNİVERSİTESİ YAYINLARI
ATATURK UNIVERSITY PUBLICATIONS

Research Article *Araştırma Makalesi* DOI: 10.5281/zenodo.15739387

Fundamentals and Data Analysis of Neutron Monitor Systems

Nötron Monitör Sistemlerinin Temelleri ve Verilerinin Analizi

Mahmut GÜDEN

Atatürk University, Graduate School of Natural and Applied Sciences, Department of Astronomy and Astrophysics, Erzurum, Türkiye

Abstract

Cosmic Rays (CRs) carry important information for understanding the energetic processes of the universe and space weather events, and Neutron Monitors (NM) are the primary tools for continuously measuring the flux of these particles at ground level. However, NM data are significantly affected by atmospheric pressure changes. This study presents the process and results of removing this atmospheric effect from multi-station data obtained from the global Neutron Monitor Database (NMDB) network. The study utilised raw count and pressure data from 5 different NM stations for the period 2010–2025. The data processing and analysis process was carried out using the Python programming language and the pandas and NumPy libraries; barometric pressure correction was applied to the raw data using the standard Dorman equation. The findings showed that the correction process successfully eliminated pressure-induced noise and sudden fluctuations in the raw data. The corrected data produced much more stable time series and made important signals, such as potential Ground Level Events (GLE) and Forbush Decrease (FD) that were masked in the raw data, more prominent. These results confirm that barometric correction is a critical and necessary pre-processing step for reliable analysis in space weather events and long-term solar modulation studies.

Keywords: Cosmic Rays, Neutron Monitors, NMDB, Pressure Correction, Ground Level Enhancement (GLE), Forbush Decrease (FD)

Öz

Kozmik Işınlar (CRs), evrenin enerjik süreçlerini ve uzay havası olaylarını anlamak için önemli bilgiler taşır ve Nötron Monitörleri (NM) bu parçacıkların yer seviyesindeki akısını sürekli olarak ölçen temel araçlardır. Ancak, NM verileri atmosferik basınç değişimlerinden ciddi şekilde etkilenir. Bu çalışma, küresel Nötron Monitörü Veritabanı (NMDB) ağından alınan çoklu istasyon verilerindeki bu atmosferik etkinin giderilmesi sürecini ve sonuçlarını sunmaktadır. Çalışmada, 2010-2025 periyodu için 5 farklı NM istasyonundan alınan ham sayım ve basınç verileri kullanılmıştır. Veri işleme ve analiz süreci, Python programlama dili ile pandas ve NumPy kütüphaneleri kullanılarak yürütülmüş; ham verilere, standart Dorman denklemi ile barometrik basınç düzeltmesi uygulanmıştır. Bulgular, düzeltme işleminin, ham verilerdeki basınç kaynaklı gürültüyü ve ani dalgalanmaları başarılı bir şekilde ortadan kaldırdığını göstermiştir. Düzeltilmiş veriler, çok daha kararlı zaman serileri ortaya koymuş ve ham veride maskelenmiş olan potansiyel Yer Seviyesi Olayları (GLE) ve Forbush Azalması (FD) gibi önemli sinyallerin belirgin hale gelmesini sağlamıştır. Bu sonuçlar, barometrik düzeltmenin, uzay havası olayları ve uzun vadeli Güneş modülasyonu çalışmalarında güvenilir analizler yapabilmek için kritik ve zorunlu bir ön işleme adımı olduğunu doğrulamaktadır.

Anahtar Kelimeler: Kozmik Işınlar, Nötron Monitörler, NMDB, Basınç Düzeltmesi, Yer Seviyesi Artışları (GLE), Forbush Azalması (FD).

Sorumlu Yazar/Corresponding Author: Mahmut Güden
E-mail: gudenmahmut@gmail.com

Geliş Tarihi/Received 03.05.2025
Kabul Tarihi/Accepted 04.06.2025
Yayın Tarihi/Publication Date 27.06.2025

Cite this article
Guden M. (2025) Fundamentals and Data Analysis of Neutron Monitor Systems. *Journal of Anatolian Physics and Astronomy, 4*(1), 13-23.

Introduction

Neutron Monitors (NM) are sensitive detectors designed to indirectly measure the flux of cosmic rays (CRs), which are high-energy particles continuously reaching the Earth's atmosphere from outer space, at ground-based stations. These CRs are products of the most energetic processes in the universe and are essentially a high-energy particle flux. The majority of the flux consists of protons (90%), helium nuclei (alpha particles) (9%), and heavier atomic nuclei (1%) (Gaisser et al., 2016; Polatoğlu & Yeşilyaprak, 2023). The CR spectrum contains very small amounts of electrons and gamma rays. These particles are accelerated to enormous energies in supernova remnants, active galactic nuclei, and other energetic astrophysical phenomena; travel long distances through intergalactic space, and reach Earth (Blasi, 2013). Since they are composed of charged particles, they are affected by magnetic fields within the galaxy and the heliosphere during their journey; this alters their direction of arrival, making it difficult to directly identify their source.

CR research was largely limited to high-altitude balloon measurements until the mid-1940s. The most significant scientific and technological breakthrough in this field occurred in 1948 with the invention of the neutron monitor by physicist John A. Simpson. Simpson's design enabled the continuous and systematic measurement of the secondary neutron flux resulting from CRs' interaction with the atmosphere at the Earth's surface (Simpson, 1951). This invention is considered a turning point in CR physics, as it became a fundamental tool for tracking time-dependent changes in CRs and solar-induced events. This laid the foundations for space weather research, and today, the Neutron Monitor Database (NMDB), used in dozens of observatories around the world, has become an indispensable component of modern astrophysics and geomagnetic research.

The working principle of NMs is based on the indirect detection of ‘Primary Cosmic Rays’ not directly, but through secondary neutrons, which are products of Secondary Cosmic Rays resulting from the interaction of these rays with the atmosphere. Primary cosmic rays are high-energy charged particles of galactic or extragalactic origin, primarily consisting of protons and helium nuclei. When these particles reach the Earth's atmosphere, they collide with air atoms, particularly nitrogen and oxygen, at high energies, initiating particle cascades known as ‘Extensive Air Showers (EAS)’ (Auger et al., 1939). As a result of these chain reactions, a large number of secondary particles (pions, muons, neutrons, electron-positron pairs, neutrinos, etc.) are produced, depending on the energy of the primary particle (Kampert & Unger, 2012). Neutrons, which have a lifetime of 878.4±0.5 seconds and are electrically neutral, are produced in this process through nuclear fission and hadronic interactions (Particle Data Group et al., 2022). Since they do not carry an electric charge, they can travel relatively long distances (approximately 3–10 km) in the atmosphere without being affected by the Earth's magnetic field (Gaisser et al., 2016). This property makes them detectable by NM instruments located at ground level. Monte Carlo simulations have shown that the scattering processes responsible for secondary neutron production are sensitive to the kinetic energy of incoming primary CRs and changes in the density profile of the atmosphere (Heck et al., 1998).

These continuous and sensitive observations play a critical role in understanding the dynamics of space weather events. NM instruments typically record long-term variations in Galactic Cosmic Rays (GCR), such as those associated with the Sun's 11-year sunspot cycle and 22-year magnetic cycle (Potgieter, 2013). In addition, they successfully detect sudden and transient events. When coronal mass ejections (CME) originating from the Sun and the magnetic clouds they create reach Earth, they block CRs from accessing our planet, causing sudden and temporary drops in their density; these events are known as Forbush Decreases (FD) (Cane, 2000). In much rarer cases, the Sun produces such intense events that the accelerated particles increase the radiation level at ground level to a degree that can be easily detected by NM. These events, known as Ground Level Enhancement (GLE) (Plainaki et al., 2007; Polatoğlu, 2025), serve as evidence of the most energetic solar events.

The scientific impacts of CR research are diverse. These studies enhance our understanding of both fundamental physics and interstellar environment dynamics by testing theories regarding particle acceleration and propagation in astrophysical environments. CRs serve as natural probes for obtaining information about magnetic fields and turbulence structures in the galaxy and provide valuable clues about the interstellar medium and galactic wind formation. From a technological perspective, CRs have direct impacts on fields such as space engineering and radiation safety. Secondary particles produced in atmospheric showers pose a serious risk by causing Event Effects (SEEs) in sensitive electronic devices used in space missions and high-altitude aviation (Normand, 1996). Therefore, research on CRs and their atmospheric interactions has also pioneered the development of new detection techniques, advanced simulation tools, and machine learning methods, finding a wide range of applications in both scientific research and applied technologies (Polatoğlu, 2024). In this regard, CRs are both a cornerstone of our efforts to understand the universe and an important area of research that encourages innovative solutions in the fight against their effects on modern technologies.

Table 1. Features of NM64 and IGY monitors.

Feature	IGY Standard	NM64 Standard
Introduction Year	1957	1964
Alias	Simpson Monitor	Super monitor
Counting Efficiency	Standard	High (~3.3 times more than IGY)
Reflector/Moderator	Paraffin	Polyethylene
Design Purpose	First global standard network	To increase sensitivity and counting rate
Current Use	Very rare, mostly for historical data	The main standard for the worldwide network

Working Principles of Neutron Monitors

A standard NM design is typically the International Geophysical Year (IGY) or the IGY monitor developed by Hatton and Carmichael in 1964 to increase the Simpson's International Geophysical Year (IGY) design or the NM64 standard developed by Hatton and Carmichael in 1964 to increase the efficiency and counting rate of the IGY monitor, and is configured to maximise sensitivity to secondary neutrons produced in widespread air showers created by primary cosmic rays with energies above the local geomagnetic cutoff (Hatton, 1971). The characteristics of the NM64 and IGY monitors are shown in Table 1. The basic function of the device is to efficiently capture and count these neutrons produced in the atmosphere and convert them into electrical signals. This detection process occurs as a multi-stage chain of physical reactions through several basic components that work together, and is summarised schematically in Figure 2. An example of an NM chamber (ROME) is shown in Figure 1.

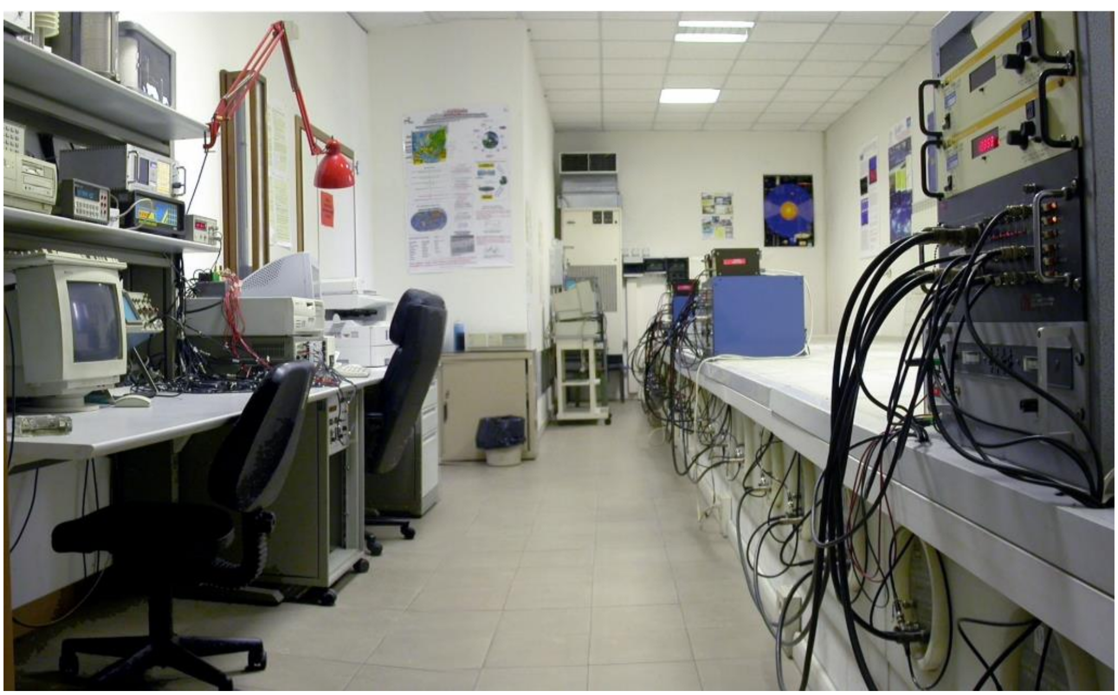

Figure 1. Interior view of the ROME Neutron Monitor station. It is a 20-NM64 type neutron monitor consisting of a total of 20 counter tubes. This structure consists of different units, including three 3-counter units, one 5-counter unit, and one 6-counter unit (NMDB, 2025) (https://www.nmdb.eu/station/rome).

The neutron detection process begins when a secondary neutron from the atmosphere enters the detector and follows these steps:

i. Neutron Multiplication (Lead Producer): A high-energy neutron entering the detector first interacts with the multiplier layer, which consists of thick lead blocks. The collision of the incoming neutron with lead nuclei triggers nuclear reactions known as spallation. As a result of these reactions, a large number of new, lower-energy neutrons are scattered from the single incoming neutron, and the initial signal is amplified (Bauer, 2001).

ii. Neutron Slowdown (Polyethylene Moderator): The fast neutrons emitted by the generator then enter the moderator layer, which surrounds the detector tubes and is typically made of polyethylene. This material, rich in hydrogen atoms, effectively causes fast neutrons to lose their energy through elastic collisions and slows them down to thermal energy levels. This moderation process is of critical importance as it maximises the probability of neutron capture in the next stage (Clem & Dorman, 2000).

iii. Neutron Detection and Signal Generation (Proportional Counter): When a neutron reaches thermal velocity, it loses its energy through numerous elastic collisions with its surroundings (particularly with atoms in the medium) and eventually reaches an average kinetic energy (i.e., thermal equilibrium) corresponding to the temperature of the medium it is in. Thermalised neutrons enter gas-filled proportional counter tubes, which are the heart of the detector and are typically filled with Boron Trifluoride (BF3) or Helium-3 gas. A thermal neutron is captured by the nucleus of a gas atom inside the tube. For example, in the case of BF3 gas, a neutron is captured by a Boron-10 nucleus, triggering the ^{10}B (n, α) reaction. This nuclear reaction produces energetic charged particles (an alpha particle and a Lithium nucleus) capable of ionising the gas. This ionisation creates an electrical pulse within the tube; this pulse is amplified by electronic circuits and counted as a valid ‘count’ if it exceeds a certain threshold value. These count rates reflect temporal changes in the incoming CR flux (Clem & Dorman, 2000).

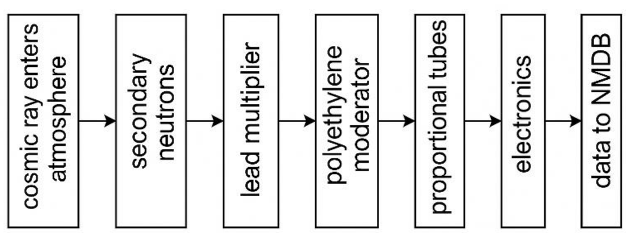

Figure 2. Neutron Monitor (NM) System Working Diagram

The recorded raw count rates are sensitive to changes in CRs flux as well as various local atmospheric and environmental conditions. Therefore, raw data must undergo calibration and correction protocols to ensure reliability before being used in scientific analyses. The main factors affecting data quality are as follows:

- Atmospheric Pressure: This is the most dominant environmental effect on measurements. An increase in air pressure at the station increases the mass thickness of the atmosphere, leading to greater absorption or scattering of secondary neutrons. This reduces the net neutron flux reaching the detector and, consequently, the count rate.

- Temperature and Environmental Conditions: Changes in ambient temperature can affect detector efficiency by altering the density of the moderator material and the reaction kinetics of the counter gases. In addition, structures such as snow, puddles, or buildings in the immediate vicinity of the detector can scatter or absorb incoming neutrons, thereby altering the measured count rate.

Neutron Monitor Database (NMDB) and NM Applications

The NMDB was established to collect, standardise, and make available secondary neutron data on a global scale. The NMDB is a central data repository that stores high-time-resolution data from NM stations located around the world. Funded as an e-Infrastructure project under the European Commission's Seventh Framework Programme (FP7), the NMDB is an international collaboration bringing together research institutions from various countries. Thanks to this initiative, stations in the global network, which have been collecting data for over 60 years, have begun to transmit their data in a standard format and in real time to a centralised system.

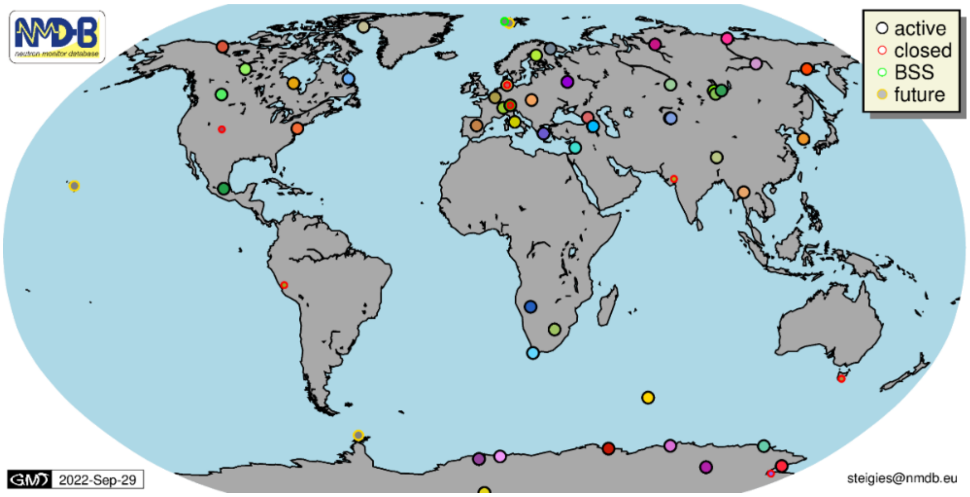

Figure 3. Neutron monitoring stations in the world (NMDB, 2025)

NMDB collects its data from a globally distributed network of NM stations. These stations are geographically distributed from the poles to the equator. Historically, 63 NM stations have been established worldwide. As shown in Figure 3, some of these stations continue to actively collect data today, while others are closed. 56 are active, while 6 are closed. One of these 63 stations is the ‘UFSZ’ station. This station is slightly different from the others. The UFSZ station operates using ‘Bonner spheres.’ These spheres, which serve as moderator material within the NM, count neutrons by separating them according to their energy levels. In other words, each neutron interacts with spheres of different sizes inside the station based on its energy level (Thomas & Alevra, 2002).

NM data have versatile applications for understanding Sun-Earth interactions by examining changes in CR density. These applications can be broadly categorised into two main categories: monitoring long-term changes associated with solar activity and detecting and analysing sudden, transient space weather events. Continuous NM data series spanning decades enable the quantitative assessment of long-term relationships, such as the modulation observed in GCR flux during the Sun's 11-year activity cycle. This provides a critical foundation for modelling particle transport processes in the heliosphere and the effects of solar activity on Earth's radiation environment. The most critical application of NM data is the analysis of sudden and potentially dangerous space weather events. Among these events, Solar Energetic Particle (SEP) events originating from the Sun and reaching energies of GeV levels are at the forefront. These most intense SEP events can only be detected at ground level by the global NM network and are referred to as Ground Level Enhancements (GLEs). The confirmation of an event as a GLE is based on the observation of a simultaneous and statistically significant increase in counts at multiple stations in different geographical locations. These rare events, which occur only a few times per solar cycle, serve as natural laboratories for understanding how particles are accelerated to such high energies and propagated in the Sun and heliosphere. The analysis of GLE events requires various advanced techniques that leverage the power of the global NM network:

Time Series Analysis: By examining the temporal variation of count rates at each station, temporal characteristics such as the sudden onset time of the event, the time to reach maximum, and the decay profile are precisely determined.

Spectral and Angular Distribution Analysis: Since each station in the global network has a different cut-off energy and a different ‘view’ direction, the energy spectrum and angular distribution (anisotropy) of incoming particles can be modelled. This analysis is crucial for revealing the spatial and temporal structure of SEP events and provides direct data for testing particle acceleration models (Plainaki et al., 2007).

Real-Time Warning Systems: NM data is fed in real time into systems that automatically detect GLE events in their initial stages and generate space weather warnings. Systems such as the developed ‘GLE Alert Plus’ play a critical role in providing timely warnings against radiation risks for technological systems such as high-altitude aviation and satellite operations.

NM data are also used to investigate the characteristics of Forbush Decreases (FD) caused by magnetic clouds associated with coronal mass ejections (CME) from the Sun. The analysis of these events provides fundamental data for the development and validation of space weather prediction models. The effectiveness of all these applications has been enhanced by integrating the data into central databases such as NMDB. These platforms facilitate multi-station analyses, thereby improving the reliability of space weather predictions and deepening our scientific understanding of solar physics.

Thanks to the data provided by the NMDB platform and the atmospheric cascade models developed, significant applications have been developed in the field of cosmic radiation dosimetry in aviation. Among the prominent applications are AVIDOS (Aviation Dosimetry System) (Latocha et al., 2009), designed to calculate and record the radiation doses to which pilots and flight crew are exposed, and EPCARD (European Program Package for the Calculation of Aviation Route Doses) (Schraube et al., 2000), which performs effective dose calculations for flight routes across Europe. These systems model the radiation environment, which varies depending on solar activity and geomagnetic conditions, providing critical information for flight safety and personnel health.

Data and Method

The data used in this study were obtained from the Neutron Monitor Database (NMDB), which provides researchers with high-temporal-resolution CRs data (https://www.nmdb.eu). The NMDB offers great flexibility in data access by providing both user-friendly web interfaces and application programming interfaces (APIs) that enable programmatic access. The raw neutron count rates with a 1-month resolution and the corresponding atmospheric pressure values used in the study were obtained through this platform. The geographical locations and technical specifications of the analysed stations are summarised in Table 2. The study period covers the time interval from 01.01.2010 to 01.01.2025.

Table 2. Neutron monitors and their features

Abbreviation	Station Name	Latitude (°)	Longitude (°)	Altitude (m)	Cut- off Rigidity (GV)
TERA	Terre Adélie	–66.66	140.00	32	0.01
OULU	Oulu	65.05	25.47	15	0.81
NEWK	Newark	39.68	–75.75	50	2.40
ROME	Rome	41.90	12.52	0	6.27
ATHN	Athens	37.97	23.78	260	8.53

The latitude, longitude, altitude, and cut-off rigidity values given in Table 2 are important factors affecting the recorded CR flux. Stations at high magnetic latitudes detect lower-energy CRs, while higher altitudes generally measure higher fluxes due to reduced atmospheric absorption (Gaisser et al., 2016). Cut-off Rigidity defines the minimum rigidity required for a particle to pass through the magnetic field (Simpson et al., 1953) and is lower in regions closer to the poles. This situation leads to stations with low cut-off rigidity detecting a broader energy spectrum. Longitude, on the other hand, can cause stations at the same latitude to have different cut-off rigidity due to the non-homogeneity of the Earth's magnetic field.

In order to follow a repeatable and automated process for data access, NMDB's RESTful API infrastructure was utilised. This approach enabled queries to be created for specific stations and time intervals, and data to be pulled directly into the analysis environment using the Python programming language and the ‘requests’ library. The data provided by NMDB is in a standard plain text (ASCII/CSV) format that is compatible with various computational tools. This allows the data to be efficiently converted into structured data frames using Python libraries such as pandas, NumPy, plot, etc.

These raw census rates, which form the basis of the analyses, contain fluctuations caused by atmospheric pressure changes that can mask the actual signal. Therefore, processing the raw data before using it in subsequent stages is a critical step. The barometric correction procedures and other methodological steps applied to the data are explained in detail in the next section.

Method

The methodology followed in this study involves analysing data obtained from NMDB using a workflow developed in Python. The entire data processing process was carried out programmatically to ensure the reproducibility and accuracy of the results. The raw neutron count rates obtained from the NMDB and the corresponding instantaneous atmospheric pressure (P) data form our basic data set. These data were transferred to a DataFrame object using the pandas library, which provides a powerful and flexible structure for time series analyses. This structure facilitated the organisation, management, and preparation of the dataset for subsequent steps.

One of the most critical pre-processing steps in the analysis of NM data is the correction of atmospheric pressure changes, which are the primary source of non-astrophysical fluctuations. To eliminate this effect, a barometric correction procedure based on the Dorman Equation, which is accepted as standard in the literature, was applied (Dorman, 1991). The relevant formulation is given in Equation 1:

$$N_{corr} = N_{raw} \cdot e^{-\beta(P-P0)} \tag{1}$$

The parameters in the equation are defined and applied as follows. Ncorr: The final count rate corrected for pressure effects and ready for analysis. Nraw: Raw count data. β: The barometric coefficient specific to each observation station, obtained from the literature. P: The instantaneous atmospheric pressure value. P0: The reference pressure is calculated as the average of the pressure series to establish a stable baseline throughout the observation period. This value was calculated using pandas' statistical functions. Numerical calculations such as exponential functions were efficiently performed using the NumPy library, which offers high performance in scientific calculations. At the end of this methodological process, a reliable time series was obtained, free from atmospheric pressure effects, which will serve as the basis for subsequent scientific analyses.

Research Findings

Raw data obtained from NMDB stations, atmospheric conditions affecting these data, and refined results obtained after applying the procedures described in the Method section are presented and interpreted.

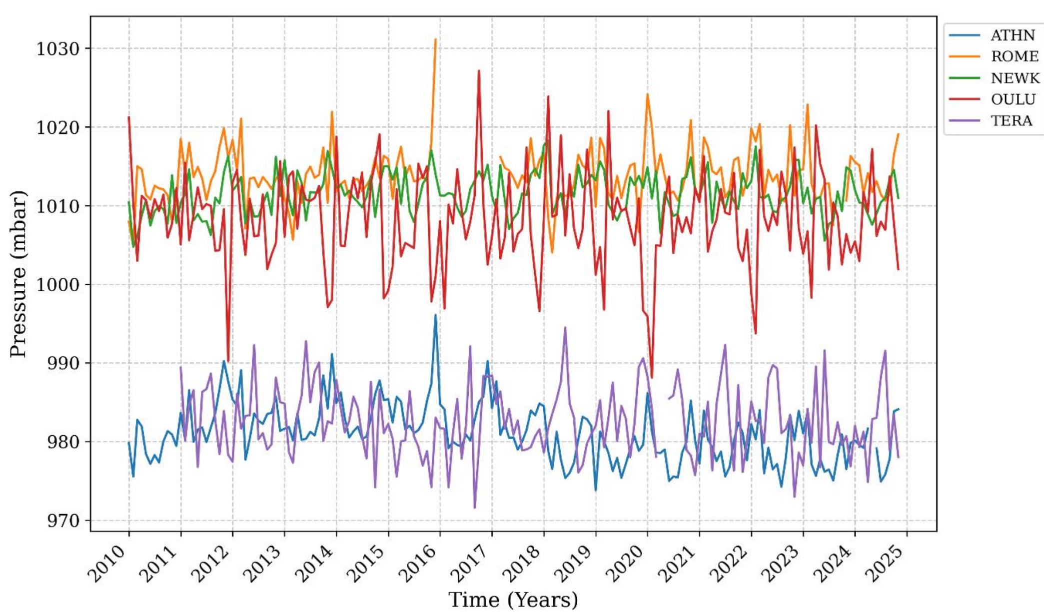

Figure 4. Atmospheric pressure time series for NM stations

Atmospheric pressure is the most important meteorological parameter directly affecting CR count rates at ground level. An increase in pressure increases the mass of the atmosphere, causing more absorption of secondary particles from CRs and thus a decrease in the count rate. Conversely, a decrease in pressure causes an artificial increase in the count rate. As shown in Figure 4, pressure values at stations exhibit significant seasonal and daily fluctuations. These fluctuations create noise in raw CR data, making it difficult to detect real signals.

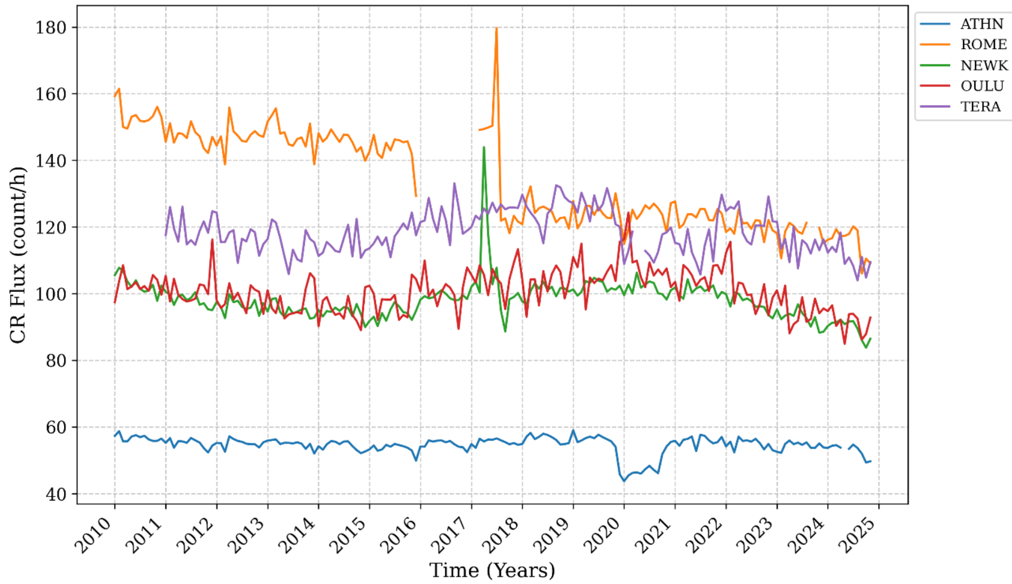

Figure 5. NM raw cosmic ray count time series

The raw data contains both changes caused by real astrophysical processes, such as solar activity, and noise created by atmospheric pressure fluctuations, as shown in Figure 5. The short-term and sharp ups and downs in the graph are largely a reflection of the pressure effect. The sudden spikes and drops observed at many stations are more likely due to changes in local weather conditions than to a real CR event.

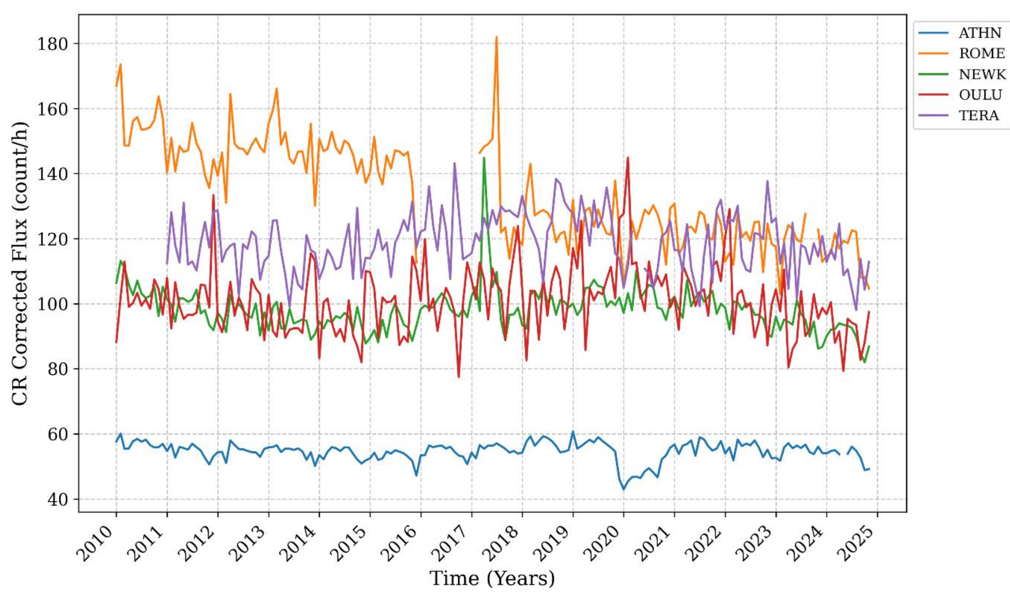

Figure 6. Final CRs time series obtained after applying pressure correction

After applying barometric correction, it can be observed that some of the short-term fluctuations in Figure 5, which are thought to be pressure-related, have decreased or disappeared. The corrected data has the potential to better reflect the actual physical changes in CR flow. For example, a sharp drop or increase observed at a particular station in Figure 5 may turn into a smoother trend or disappear completely when the pressure effect is eliminated in Figure 6. This situation demonstrates that barometric correction is an important step in increasing the comparability and reliability of data obtained from detectors in different geographical locations. When both figures are examined together, the effect of atmospheric pressure on CR measurements and how this effect can be minimised using appropriate correction methods is clearly demonstrated.

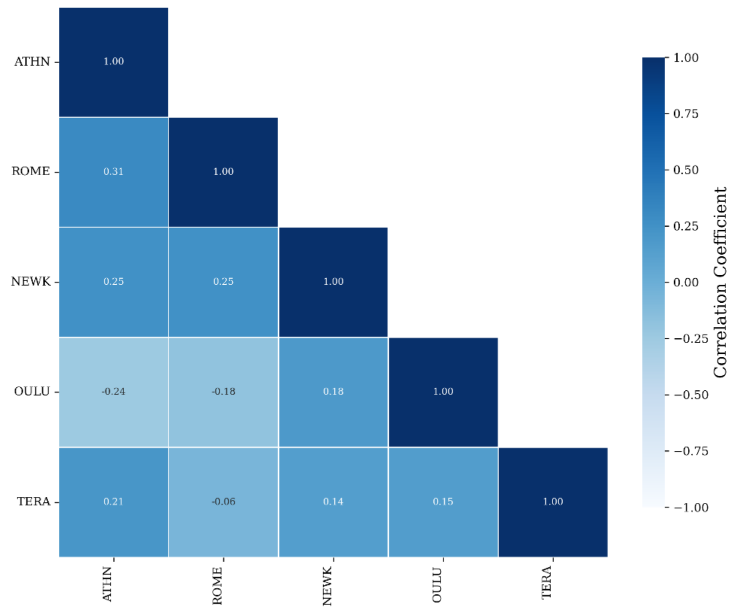

Figure 7. Correlation matrix created for stations

The correlation matrix presented in Figure 7 shows the linear relationship between the corrected CR flux data obtained from five different stations: ATHN, ROME, NEWK, OULU, and TERA. The strongest positive correlation, with a value of 0.31, is observed between the ATHN and ROME stations, and these two stations also exhibit similar positive correlations with NEWK, with values of 0.25, respectively. On the other hand, the OULU station exhibits a negative correlation with ATHN (-0.24) and ROME (-0.18). This situation is due to the stations being located in different locations and at different altitudes, as well as the data not being continuous.

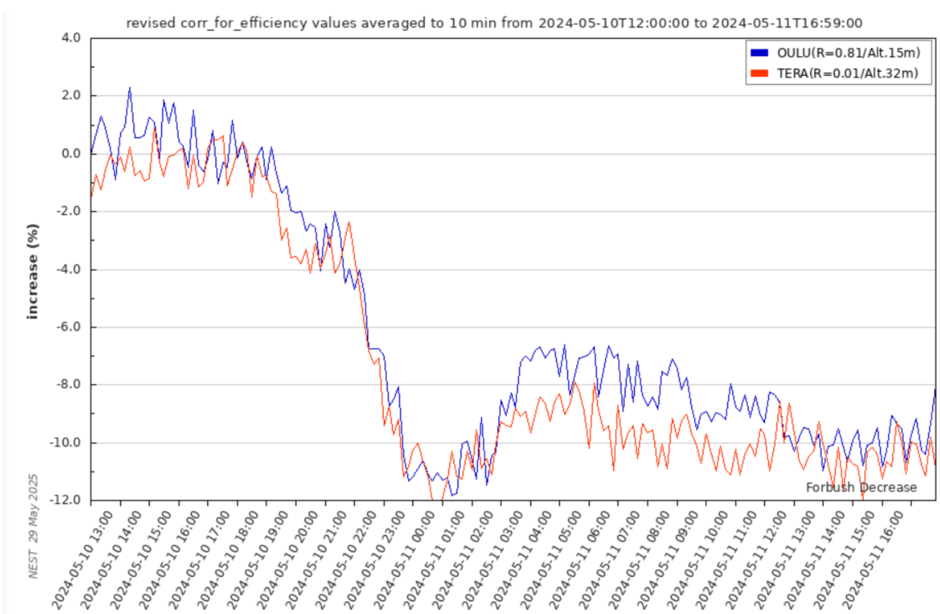

Figure 8. Forbush Decrease (FD) observed from OULU and TERA stations

There was also a significant decrease in CRs at the OULU and TERA stations, which began to become apparent between 19:00 and 20:00 on 10 May 2024 and intensified towards midnight (Figure 8). The largest decrease in CRs flux was recorded in the early hours of 11 May 2024 (00:00-01:00). The flux at the OULU station dropped to approximately -11%, while at the TERA station it reached -12% levels.

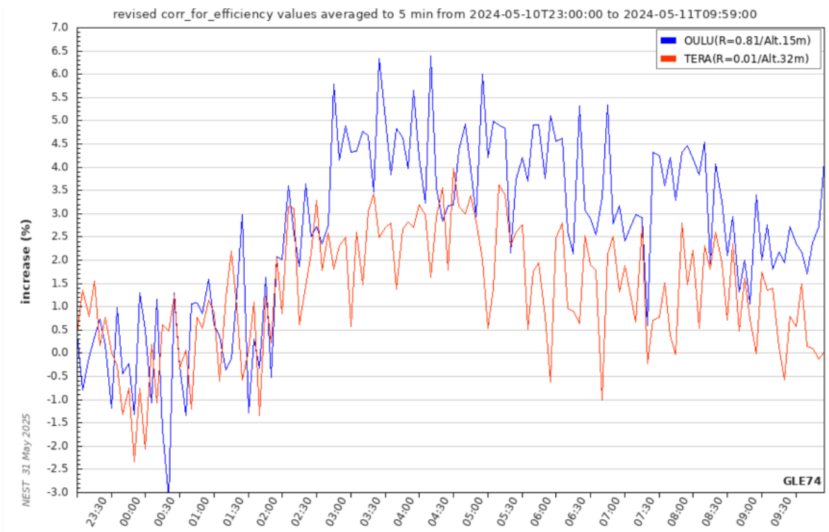

Figure 9. 74th Ground Level Enhancements (GLE) meeting held on 10 May 2024

Figure 9 shows a sudden and significant increase in the CR flux at both stations above the general background fluctuation, which is the most distinctive feature of a typical GLE event. GLE events are characterised by the entry of very high-energy particles from the Sun into the Earth's atmosphere, creating secondary particle showers, which are recorded as a sudden increase in counts by NM or muon detectors on the ground.

Conclusion

In this study, CR count values, and pressure data obtained from NMDB were examined. NM systems, which have been active since the 1960s, provide very important information for solar events, atmospheric air, and space studies. In our study, a correction process was applied to remove the effects of atmospheric pressure from the raw CR data, and the results of this process were evaluated. The research findings clearly show that raw CRs data are significantly affected by irregular fluctuations in atmospheric pressure, which reduces data quality. By applying the barometric correction based on the Dorman equation in the Python environment, it was found that this atmospheric noise was successfully eliminated, resulting in much more stable and smooth time series. This situation unequivocally confirms that atmospheric correction is an indispensable pre-processing step for the reliable investigation of space weather events (such as FD and GLEs) and long-term changes related to solar activity. Correlation analysis performed on the corrected CRs data revealed that the relationships between stations vary depending on factors such as geographical location and cut-off rigidity. However, only the increasing or decreasing trends show similarities in long-term measurements.

Research on CRs and NM systems in Turkey is still in its infancy. Although there are scintillator-based muon detectors in Turkey, there is no active NM station yet. Nevertheless, scientific and academic studies in this field are increasing. In the future, establishing an NM station by leveraging Turkey's geographical location advantage will enable the country to integrate into international space weather and astrophysics research networks, thereby enhancing national scientific capacity and contributing significantly to global data.

Acknowledgements: I acknowledge the NMDB database www.nmdb.eu, founded under the European Union's FP7 programme (contract no. 213007) for providing data and ATHN, ROME, NEWK, OULU ve TERA stations.

Hakem Değerlendirmesi: Dış bağımsız.
Çıkar Çatışması: Mahmut GÜDEN, çıkar çatışması olmadığını beyan etmiştir.
Finansal Destek: Bu çalışma için herhangi bir kurumdan finansal destek alınmamıştır.
Peer-review: Externally peer-reviewed.
Conflict of Interest: Mahmut GÜDEN has no conflicts of interest to declare.
Financial Disclosure: No financial support was received from any institution for this study.

References

Auger, P., Ehrenfest, P., Maze, R., Daudin, J., & Fréon, R. A. (1939). Extensive Cosmic-Ray Showers. *Reviews of Modern Physics*, 11(3-4), 288-291. https://doi.org/10.1103/RevModPhys.11.288

Bauer, G. S. (2001). Physics and technology of spallation neutron sources. Nuclear Instruments and Methods in Physics Research Section A: Accelerators, Spectrometers, *Detectors and Associated Equipment*, 463(3), 505-543. https://doi.org/10.1016/S0168-9002(01)00167-X

Blasi, P. (2013). The origin of galactic cosmic rays. *The Astronomy and Astrophysics Review*, 21(1), 70. https://doi.org/10.1007/s00159-013-0070-7

Cane, H. V. (2000). Coronal Mass Ejections and Forbush Decreases. *Space Science Reviews*, 93(1/2), 55-77. https://doi.org/10.1023/A:1026532125747

Clem, J. M., & Dorman, L. I. (2000). Neutron monitor response functions. *Cosmic Rays and Earth: Proceedings of an ISSI Workshop*, 21–26 March 1999, Bern, Switzerland, 335-359.

Dorman, L. I. (1991). Cosmic ray modulation. *Nuclear Physics B - Proceedings Supplements*, 22(2), 21-45. https://doi.org/10.1016/0920-5632(91)90005-Y

Gaisser, T. K., Engel, R., & Resconi, E. (2016). Cosmic Rays and Particle Physics (2. bs). *Cambridge University Press*. https://doi.org/10.1017/CBO9781139192194

Hatton, C. J. (1971). The neutron monitor. *Progress in elementary particle and cosmic ray physics*, 1-100.

Heck, D., Knapp, J., Capdevielle, J. N., Schatz, G., & Thouw, T. (1998). CORSIKA: A Monte Carlo code to simulate extensive air showers. *CORSIKA*: a Monte Carlo code to simulate extensive air showers.

Kampert, K.-H., & Unger, M. (2012). Measurements of the cosmic ray composition with air shower experiments. *Astroparticle Physics*, 35(10), 660-678. https://doi.org/10.1016/j.astropartphys.2012.02.004

Normand, E. (1996). Single-event effects in avionics. *IEEE Transactions on Nuclear Science*, 43(2), 461-474. https://doi.org/10.1109/23.490893

Plainaki, C., Belov, A., Eroshenko, E., Mavromichalaki, H., & Yanke, V. (2007). Modeling ground level enhancements: Event of 20/01/2005. J. of Geophys. *Research: Space Phys*., 112(A4), 2006JA011926. https://doi.org/10.1029/2006JA011926

Potgieter, M. (2013). Solar Modulation of Cosmic Rays. *Living Reviews in Solar Physics*, 10. https://doi.org/10.12942/lrsp-2013-3

Simpson, J. A. (1951). Neutrons Produced in the Atmosphere by the Cosmic Radiations. *Physical Review*, 83(6), 1175-1188. https://doi.org/10.1103/PhysRev.83.1175

Latocha, M., Beck, P., & Rollet, S. (2009). AVIDOS--a software package for European accredited aviation dosimetry. *Radiation Protection Dosimetry*, 136(4), 286-290. https://doi.org/10.1093/rpd/ncp126

NMDB. (2025). *NMDB*. https://www.nmdb.eu/

Particle Data Group, Workman, R. L., Burkert, V. D., Crede, V., Klempt, E., Thoma, U., Tiator, L., Agashe, K., Aielli, G., & Allanach, B. C. (2022). Review of particle physics. *Progress of theoretical and experimental physics,* 2022(8), 083C01.

Polatoğlu, A. (2024). Temporal Dynamics of Cosmic Rays and Sunspot Numbers: Insights from SARIMA Analysis. *International Journal of Innovative Research and Reviews*, 8(2), 35-41.

Polatoğlu, A. (2025). A thorough examination of concurrent measurements cosmic ray radiation and meteorological parameters with the support of machine learning. *Radiation Measurements*, 181, 107375. https://doi.org/10.1016/j.radmeas.2025.107375

Polatoğlu, A., & Yeşilyaprak, C. (2023). Using and Testing Camera Sensors with Different Devices at Cosmic Ray Detection. *Erzincan Üniversitesi Fen Bilimleri Enstitüsü Dergisi*, 16(2), 590-597. https://doi.org/10.18185/erzifbed.1167041

Schraube, H., Heinrich, W., Leuthold, G., Mares, V., & Roesler, S. (2000). Aviation route dose calculation and its numerical basis. *Aviation*, 4(4), 1a-45.

Simpson, J. A., Fonger, W., & Treiman, S. B. (1953). Cosmic Radiation Intensity-Time Variations and Their Origin. I. Neutron Intensity Variation Method and Meteorological Factors. *Physical Review*, 90(5), 934-950. https://doi.org/10.1103/PhysRev.90.934

Thomas, D. J., & Alevra, A. V. (2002). Bonner sphere spectrometers—A critical review. Nuclear Instruments and Methods in Physics Research Section A: Accelerators, Spectrometers, *Detectors and Associated Equipment*, 476(1-2), 12-20. https://doi.org/10.1016/S0168-9002(01)01379-1

ATATÜRK ÜNİVERSİTESİ YAYINLARI
ATATURK UNIVERSITY PUBLICATIONS

Research Article *Araştırma Makalesi* DOI: 10.5281/zenodo.15739462

Differentiation of Gallbladder Stones According to Their External Structure and Cross-Sectional Morphological Features such as Color, Size and Shape

Safra Kesesi Taşlarının Dış Yapılarına ve Renk, Boyut ve Şekil Gibi Kesitsel Morfolojik Özelliklerine Göre Ayırt Edilmesi

Orhan ÇİMEN[1]
[1]*Erzincan Binali Yıldırım University, Faculty of Medicine, Department of Surgical Medical Sciences, Department of General Surgery, Erzincan, Türkiye*

Ferda KESKİN ÇİMEN[2]
[2]*Erzincan Binali Yıldırım University, Faculty of Medicine, Department of Surgical Medical Sciences, Department of Medical Pathology, Erzincan, Türkiye*

Sevil DURDAĞI[3]
[3]*Erzincan Binali Yıldırım University, Faculty of Arts and Sciences, Department of Physics, Erzincan, Türkiye*

Hatice GEDİK[3]
[3]*Erzincan Binali Yıldırım University, Faculty of Arts and Sciences, Department of Physics, Erzincan, Türkiye*

Abstract
Gallstones are gravel-like substances that form over time inside the gallbladder and are one of the most painful biliary tract diseases in adults, and are known to have a high incidence. Bile is composed of water, cholesterol, fats, bile salts, proteins, and bilirubin. While bile can usually dissolve cholesterol, crystals that can eventually turn into stones can form in the presence of too much cholesterol. It is difficult to define a clear classification system according to the types of an ideal gallstone, but we can generally group them according to their main chemical composition. Key factors in the etiopathogenesis of gallstone disease can be determined by chemical, structural, and elemental composition analyses. Different complementary analytical techniques, both microscopic and spectroscopic, can be applied, and the ultrastructure of gallstones and the identification of trace elements can also be done. The aim of this study was to investigate the structural features of gallstones in sixty patients accepted for cholecystectomy from Erzincan and surrounding regions. In this study, gallstone samples were collected from 60 patients who were hospitalized in Erzincan Binali Yıldırım University Mengücek Gazi Training and Research Hospital General Surgery Clinic and underwent cholecystectomy due to symptomatic gallbladder disease without evidence of gallbladder malignancy between February 2025 and April 2025. The external and cross-sectional morphological features of gallstones, such as color, size, shape, and number of stones, were examined with the naked eye, and their photographs were taken with high sensitivity and resolution. Selected gallstones showing distinct stratification as core, middle layer, and shell were separated according to these factors. In addition, when the structure of the stones was examined, concentric layers containing alternating dark and light-colored bands were observed, emphasizing the importance of compositional changes in bile during the formation of gallstones.

Keywords: Gallbladder stone, External structure, Cross-sectional morphological feature.

Öz
Safra kesesinin içinde zamanla oluşan çakıl benzeri maddeler olan safra taşları, yetişkinlerde en ağrılı safra yolu hastalıklarından biridir ve yüksek oranda görüldüğü bilinmektedir. Safra, su, kolesterol, yağlar, safra tuzları, proteinler ve bilirubinden oluşur. Safra genellikle kolesterolü çözebilirken, çok fazla kolesterol varlığında sonunda taşa dönüşebilen kristaller oluşabilir. Safra kesesi taşı hastalığının etiyopatogenezindeki temel faktörler kimyasal, yapısal ve elementel kompozisyon analizleri ile belirlenebilir. Hem mikroskobik hem de spektroskopik olmak üzere farklı tamamlayıcı analitik teknikler uygulanabilir ve safra kesesi taşlarının ultra yapısı ve eser elementlerin tanımlanması da yapılabilir. Bu çalışmada Erzincan ve çevre bölgelerden kolesistektomi için kabul edilen altmış hastanın safra taşının yapısal özelliklerini araştırma amaçlanmıştır. Bu çalışmada Şubat 2025 ile Nisan 2025 tarihleri arasında Erzincan Binali Yıldırım Üniversitesi Mengücek Gazi Eğitim ve Araştırma Hastanesi Genel Cerrahi Kliniğinde yatan ve safra kesesi malignitesi kanıtı olmaksızın semptomatik safra kesesi hastalığı nedeniyle kolesistektomi yapılan 60 hastadan safra taşı örnekleri toplandı. Safra kesesi taşlarının renk, boyut, şekil ve taş sayısı gibi dış ve kesitsel morfolojik özellikleri çıplak gözle incelendi ve fotoğrafları yüksek hassasiyet ve çözünürlükle çekildi. Çekirdek, orta tabaka ve kabuk olarak belirgin katmanlaşma gösteren seçilmiş safra taşları bu faktörlere göre ayrıldı. Ayrıca taşların yapısı incelendiğinde koyu ve açık renkli bantları dönüşümlü olarak içeren eş merkezli katmanlar gözlenmiş olup, safra taşlarının oluşumu sırasında safradaki bileşimsel değişimlerin önemi vurgulandı.

Anahtar Kelimeler: Safra kesesi taşı, Dış yapı, Kesitsel morfolojik özellik.

Sorumlu Yazar/Corresponding Author:
Sevil DURDAĞI
E-mail: sporikli@erzincan.edu.tr

Geliş Tarihi/Received 30.04.2025
Kabul Tarihi/Accepted 19.06.2025
Yayın Tarihi/Publication Date 27.06.2025

Cite this article
Çimen, O., Keskin Çimen, F., Durdağı, S., & Gedik, H. (2025) Differentiation of gallbladder stones according to their external structure and cross-sectional morphological features such as color, size and shape. *Journal of Anatolian Physics and Astronomy,* 4(1), 24-31.

Introduction

Gallstones, also known as cholelithiasis, are masses that form in the gallbladder or biliary tract caused by abnormally high cholesterol or bilirubin levels in bile (Jones et al., 2025). Gallstones are a common disease in general (approximately 10-20% of the global adult population), with >20% of people with gallstones (usually in adulthood) developing symptoms (including biliary colic or infections) during their lifetime (Lamert et al., 2016). While black pigment stones can be caused by chronic hemolysis, brown pigment stones usually develop in blocked and infected bile ducts (Trotman B. W., 1991). Although the localization of gallstones in the bile ducts is more important than the composition for treatment, determining their structure is also important for subsequent treatment planning. Gallstone disease is defined by the occurrence of symptoms or complications caused by gallstones in the gallbladder and/or bile ducts (Internal Clinical Guidelines, 2014). From a clinical perspective or treatment algorithms, those with asymptomatic stones are usually not classified as having gallstone disease (Lee et al., 2022). Gallstone disease is among the gastrointestinal conditions associated with high costs (Shaffer et al., 2006).

In some cases, increased bilirubin levels can lead to the formation of stones. The process of gallstone formation can be summarized as follows: hard chemical particles that form and develop inside the gallbladder after a complex series of events, including bile supersaturation, nucleation, stone accumulation, and stone growth. Each gallstone has its own causes and formation mechanisms. Factors that affect the composition of gallstones can be classified as follows: age, diet, geographic region, obesity, weight loss, and ethnicity. It is difficult to define a clear classification system according to the types of an ideal gallstone, but we can group them generally according to their main chemical composition.

While gallstones are classified according to their composition and location, more than 90% of gallstones are mainly composed of cholesterol gallstones (Gu et al., 2020). Other types of stones (less than 10%) are represented by black and brown pigment stones (Sebghatollahi et al., 2023). In other words, gallstones (cholecystolithiasis) consist of cholesterol and black pigment gallstones (consisting of polymerized calcium bilirubinate). Brown pigment stones containing bilirubin and calcium fatty acid soaps are formed in infected bile ducts (Carey, 1992). Another classification type of bile duct stones is made as extrahepatic stones (choledocholithiasis) and intrahepatic stones (hepatolithiasis) (Tazuma, 2006).

Some of the risk factors for gallstones are female gender, age, pregnancy, physical inactivity, obesity, and overnutrition (Di Ciaula et al., 2018; Jukić et al., 2023). Although factors associated with metabolic syndrome also increase the risk of developing gallstones, primary prevention can be achieved through lifestyle changes (Portincasa et al., 2006). Diagnosis is mainly based on clinical symptoms, abdominal ultrasonography, and liver biochemistry tests. Symptoms usually precede the onset of the three common and potentially life-threatening complications of gallstones (acute cholecystitis, acute cholangitis, and biliary pancreatitis) (Lamert et al., 2016). Although knowledge of the genetics and pathophysiology of gallstones has increased thanks to recent studies, current treatment algorithms remain predominantly invasive and surgical (Costa et al., 2024). Therefore, our future efforts should focus on new preventive strategies, especially in at-risk patients.

Methods

Gallstone classification systems vary in terms of nomenclature and are divided into different categories based on changes in geographical location, stone composition, structure, and color. Traditionally, gallstones are divided into three main types: (a) Cholesterol stones, (b) Pigment stones and, (c) Mixed stones, but with the advancement of scientific technology, new gallstone classes such as calcium carbonate stones, phosphate stones, calcium stearate stones, protein stones, and cystine stones have been added to these three classification systems (Jones et al., 2025). The reasons for the characteristic variation of gallstones within the population of a single country have not yet been elucidated. Studies on gallstones will be able to determine the causal factors and suggest preventive measures against stone formation. This study was conducted to examine the structures of gallstones collected as a result of operations performed on patients living around Erzincan.

Gallstone samples were collected from 60 patients hospitalized in the Department of General Surgery, Mengücek Gazi Training and Research Hospital, Erzincan Binali Yıldırım University, between February 2025 and April 2025, who underwent cholecystectomy due to symptomatic gallbladder disease without evidence of gallbladder malignancy. All patients were included in the study after obtaining written and informed consent. Ethical approval for the study was obtained from the Non-Interventional Clinical Research Ethics Committee of Erzincan Binali Yıldırım University (Date: 09.01.2025, No: 2025-

01/03). All these patients had regular liver function tests and normal complete blood counts before surgery. Sample preparation steps play a critical role in gallstone analysis; therefore, potential errors were minimized through the precision demonstrated in sample preparation. The extracted gallstone samples were placed in sterile containers immediately after surgery. The stones were cleaned with deionized water and air-dried on sterile gauze. The dried samples were then transferred to dry bottles. The samples were then cleaned using isopropyl alcohol (70%) to remove blood clots on the surface and washed several times with deionized water. All collected gallstones were then dried in an oven at 50 ºC for one hour to remove moisture, and photographs were taken of the dried stone samples. After photography, they were placed back into storage bottles, and multiple gallstones removed from a patient were considered as a single sample. Large stones (>10 mm) were cut using a sterile saw to access the core. Core and surface samples were photographed separately.

The external and cross-sectional morphological features of gallstones, such as color, size, shape, and number of stones were examined with the naked eye, and their photographs were taken with high sensitivity and resolution. Selected gallstones showing distinct layering as core, middle layer, and shell were separated according to these factors. All photographs taken are given in Figure 1.

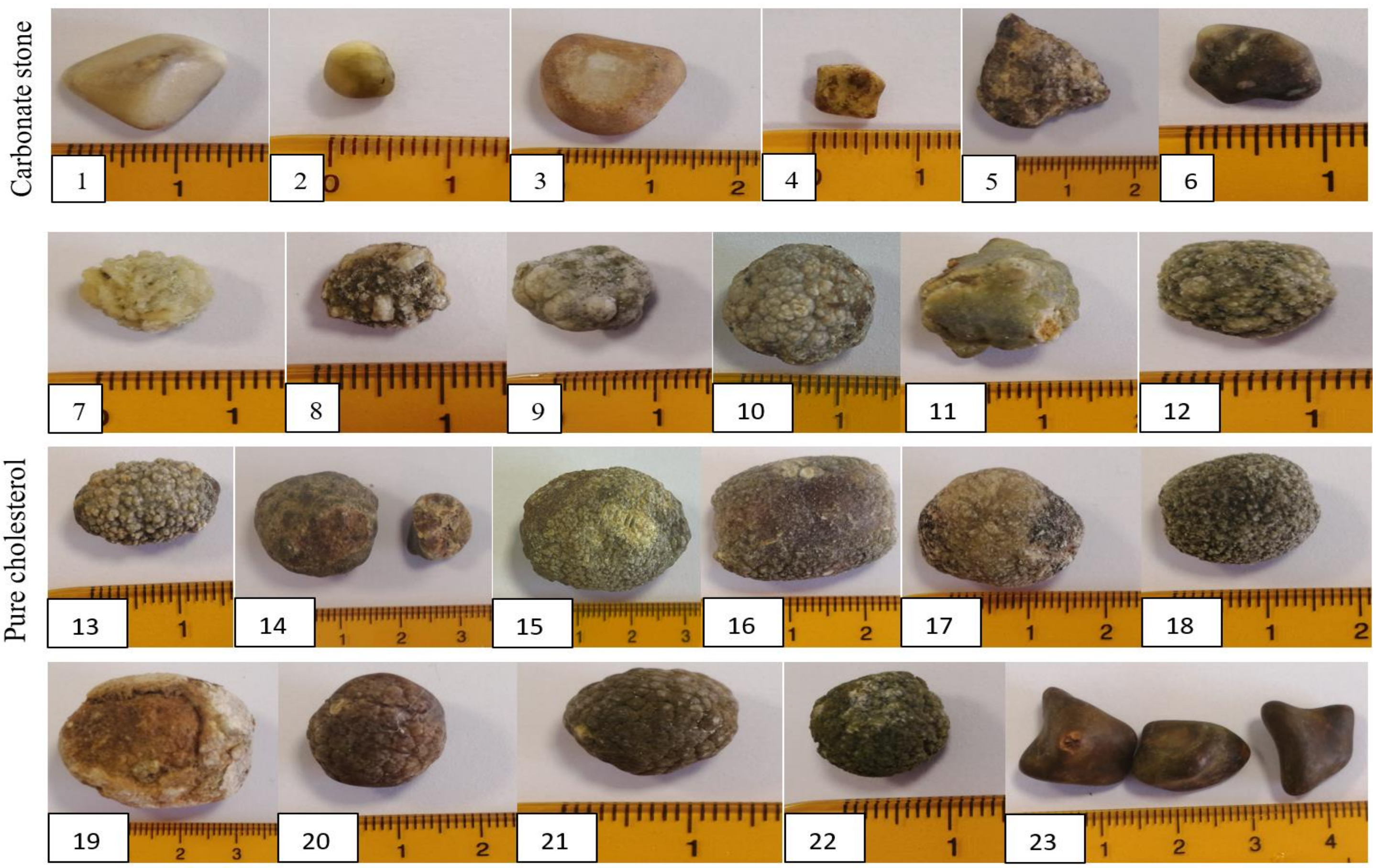

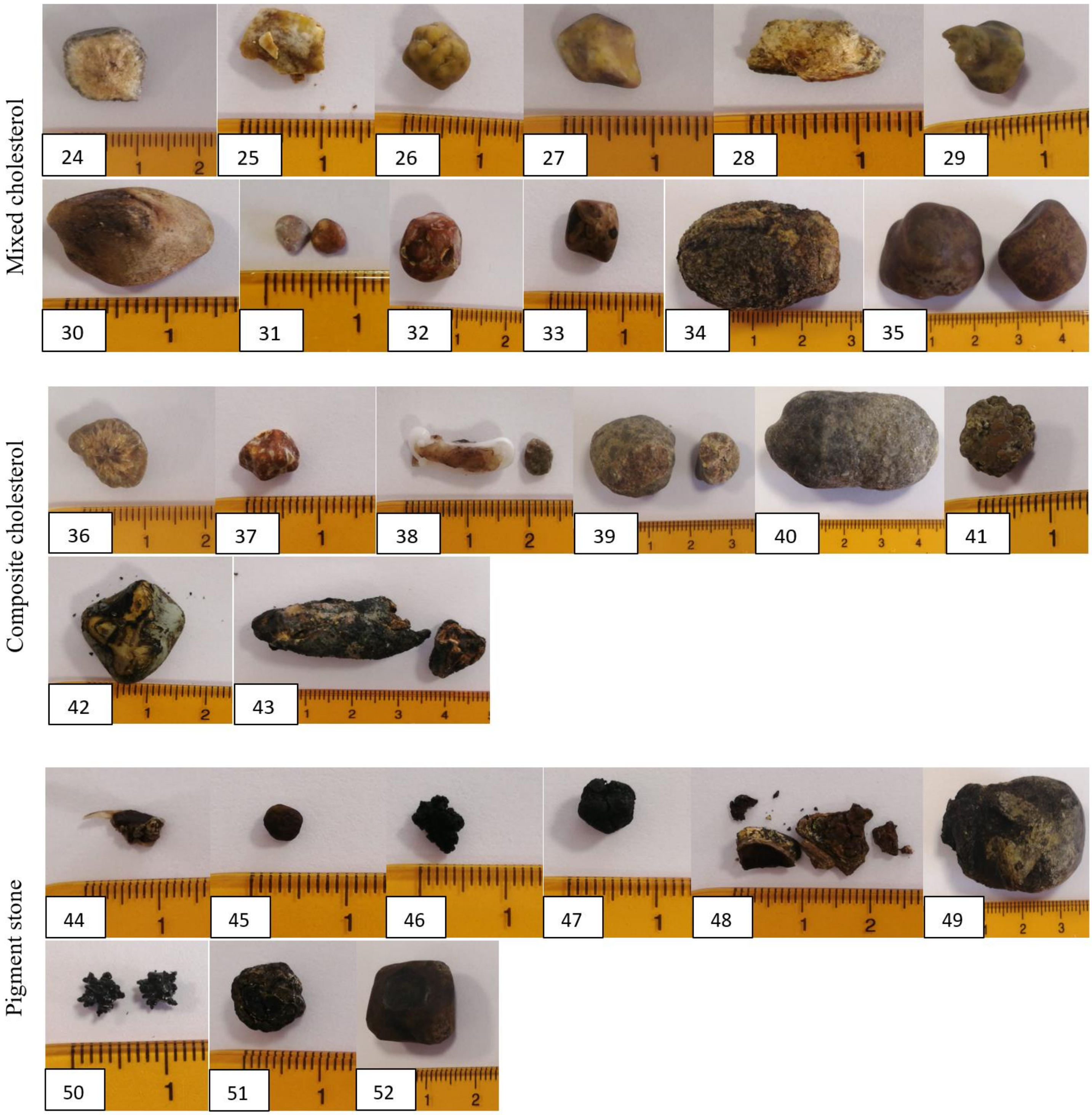

Figure 1. Classification of the different types of gallstones examined as pure cholesterol stones, mixed cholesterol stones, compound cholesterol stones and, pigment stones and images representing each type.

Results

The appearance, shape, size, color, number of stones, and distinct morphological and structural features of gallstones vary. The examined samples were initially divided into five groups according to morphological and internal structural features as pure carbonate stones (n=6; 11.5%), pure cholesterol stones (n=17; 32.7%), mixed cholesterol stones (n=12; 23.1%), composite cholesterol stones (n=8; 15.4%) and pigment stones (n=9; 17.3%) (Table 1). Table 1 shows the distribution of investigated gallstones by gender, age, and stone group. The percentage of female patients is 61.5%, and the percentage of male patients is 38.5%. It has been determined that the risk of gallstone disease is higher in female patients. While 40.6% of female patients were observed to have carbonate cholesterol-type stones, most male patients were observed to have composite cholesterol group stones. When determining cholesterol stones, a range was taken in which the surfaces were smooth, and their colors mainly varied from pale white or yellow to a yellowish-brown. When determining pigment stones, dark colors dominated by different black and brown tones were primarily taken as the basis. When determining mixed stones, situations with various colors, such as yellow to brown, black and greenish were mainly taken as the basis (Liu et al., 2002; Ha et al., 2018; Jayasoma et al., 2022).

Table 1. İnformation about the studied gallstones and the distribution of gallstone types**.**

	Female	**Male**
Number of the samples	32	20
Sample (%)	61.5	38.5
Mean age (year)	52.28	52.45
Min age (year)	24	37
Max age (year)	80	68
>50 years old (%)	50	60
Mean age of the pure cholesterol group	47.4	55.3
Mean age of the mixed cholesterol group	56.3	46.7
Mean age of the composite cholesterol group	61.7	48.8
Mean age of the pigment stone group	60.5	57.9
Mean age of the carbonate stone group	48.6	39
Samples from the pure cholesterol group (%)	40.6	20
Samples from the mixed cholesterol group (%)	28.1	15
Samples from the composite cholesterol group (%)	9.4	25
Samples from the pigment stone group (%)	6.3	35
Samples from the carbonate stone group (%)	15.6	5

The sizes and number of stones examined in this study were found to be quite variable. While the diameter of pure cholesterol stones varied between 0.77 and 3.2 cm, it was determined that most of them showed a polyhedral shape (Figure 1). The situation was different in cholesterol stones that were extracted as a single piece, and a generally spherical or oval structure was encountered. On the other hand, it was observed that most of the pigment stones in the examined samples were amorphous and brittle, with diameters smaller than 3 mm, and they were composed of many stones (Figure 1). While the small-sized pigment stones predominantly exhibited a rough surface appearance, the others showed an irregular shape. No clear conclusion could be reached in the shapes of the mixed stones; different types were recorded as irregular, round, or oval. In fact, many stones varying in size from a few mm to 2 cm were observed. Most of the cholesterol and mixed stones showed a dark-colored core resembling the core of the stone.

When examining the photographs of the gallstones, it is evident that the stones coded as 1, 2 and 3 are white carbonate stones with sharp surfaces. 16 stones coded between 7 and 23 are included in the pure cholesterol class due to their white/whitish color and rough surfaces, and their structure mainly consists of cholesterol. Gallstones coded between 24 and 35 are classified as mixed cholesterol stones due to their yellowish/yellowish-light brown color. Cholesterol is the most abundant phase following bilirubin salts and is concentrated more in the periphery than in the center of the stone, as shown in Figure 2. Stones coded between 36 and 43 are included in the compound cholesterol group because their outer surfaces are rough and dark brown (Peter et al., 2020; Kim et al., 2003). Although these stones are similar in structure to mixed cholesterol stones, cholesterol, and bilirubin remain the primary components in them. The reason for the black color observed in the central parts of gallstones is the presence of Cu in the form of copper bilirubinate (Singh et al., 2020; Liu et al., 2025) (Figure 2, like stone number 13). Gallstones, coded between 34 and 52, are easily distinguishable by their black, irregular shapes and have a harder structure than other stones.

When we look at their cross-sectional views, a radial arrangement of mineral/minerals can be seen in the middle region (Figure 2). Generally, a three-layered structure (shell, middle part, and core) and a concentric ring pattern with different thicknesses were observed, contrasting between these regions.

Figure 2 shows the cross-sectional views of the gallstones examined, and random circular arrangements were observed in some stones, such as 7, 8, 9, and 10. In addition, the yellow-brown crystallization and structure of these stones were found in layered concentric deposits, and an aggregate with a dense shell and a distinct central part was detected. In stones between 1 and 6, especially in stone number 5, a rare morphological structure, such as aragonite helictites (mineral aggregates with branched cylindrical or conical dendritic extensions) or corallites (aggregates of individual dendrite branches and clusters joined to each other, located between them) was encountered.

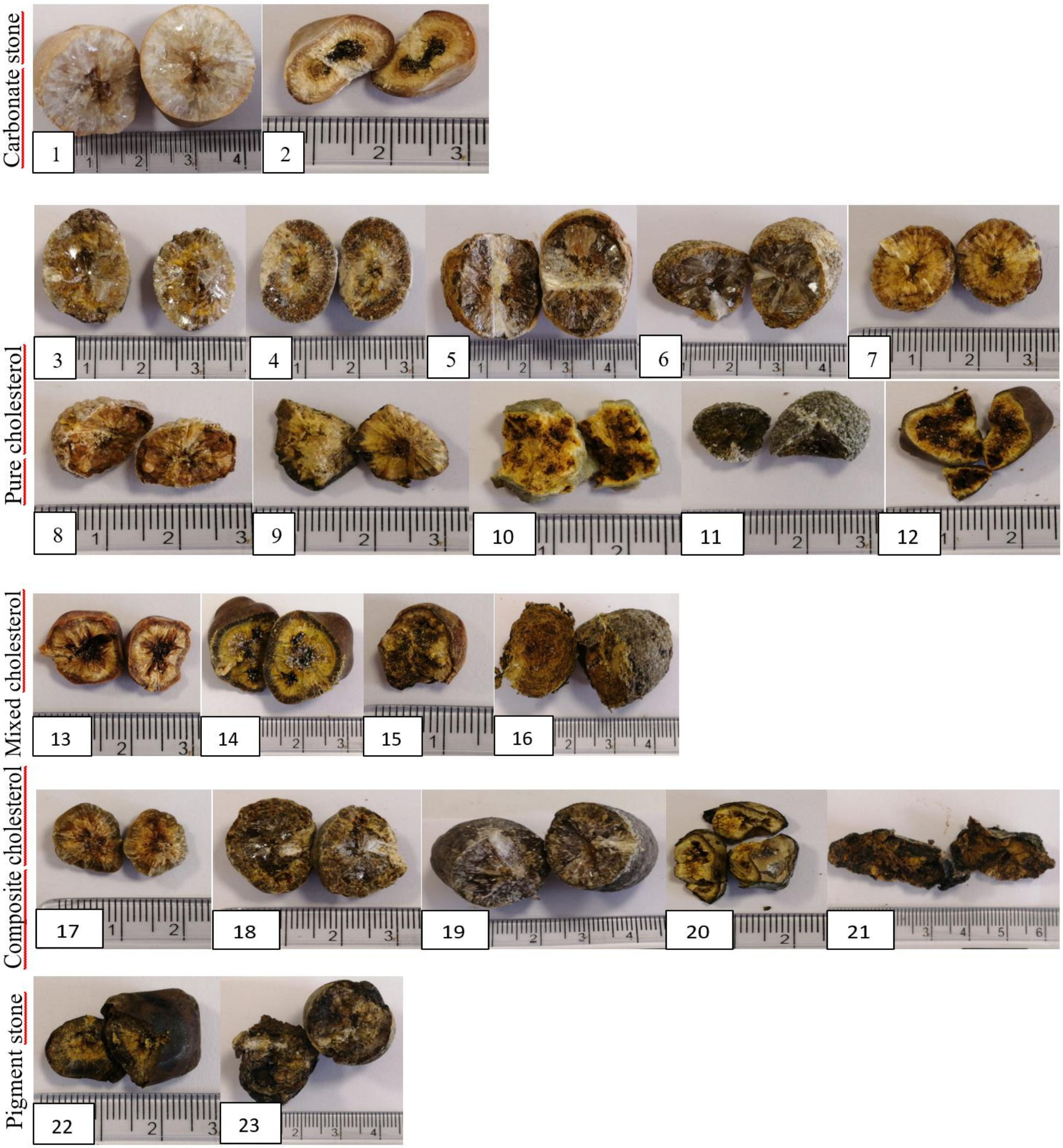

Figure 2. Section pictures after the gallstones are cut.

Conclusions

Based on this study, as previously stated by Jayasoma et al., (2022), we can say that the dark and light-colored layered structure of the stones may be related to some behaviors of the individuals, such as eating and drinking habits, quality of drinking water consumed, medication intake and dietary supplements and that the compositional structure of each gallstone is different. The direction of stone growth originates from the nucleus and follows a radial pattern outward. This study has shown that the formation mechanism of each stone has a unique microstructural feature.

To date, it has been established that gallstone disease has a direct relationship with the patient's age and gender, nutritional and obesity factors, heredity, gallbladder, and biliary tract dyskinesia, and violation of water and salt balance in the organism (Nakeeb et al., 2002; Parra-Landazury et al., 2021; Stinton et al., 2012; Pak et al., 2016). With the increasing incidence of this disease, the potential for intravital diagnosis of the phase and chemical composition of gallstones is growing. We emphasize the need for research to enhance the effectiveness of organ-preserving techniques in gallstone treatment.

Gallstone analysis is a test performed to find out what gallstones are made of, and this information helps the doctor develop a plan to reduce the risk of developing more stones in the future. In addition to determining the type of gallstone, high levels of different kinds of molecules in the urine or blood can also indicate which type of stone you have. Stone analysis can be used to determine whether you have another stone, i.e., recurrence. In addition, gallstone analysis can inform dietary changes, medication intake can be determined, and appropriate supplements (vitamins, etc.) can be recommended. Furthermore, fluid consumption (water, milk, cola, etc.) can be adjusted as needed. In other words, recurrence can be prevented by informing you of the necessary changes to your health conditions and daily life.

This study, conducted to investigate the structures of gallstones in the population of Erzincan and its surrounding districts, is part of a multidisciplinary research conducted between the Department of Surgical Medical Sciences, the Department of Medical Pathology, and the Faculty of Arts and Sciences at Erzincan Binali Yıldırım University. With the correct information provided by physicists and chemists analyzing gallstones, physicians will be able to help determine the cause(s) of stone formation and growth. After evaluating possible metabolic diseases or risk factors, physicians can make rough estimates about the stone structure without resorting to analysis by looking at metabolic disorders, and blood, and urine biochemistry. It is essential to have information about the components of gallstones to provide stone-specific treatment, identify the etiology of stone formation, prevent recurrence, and offer individualized treatment.

Etik Komite Onayı: Bu çalışma için etik komite onayı Erzincan Binali Yıldırım Üniversitesi'nden (Tarih: 09.01.2025, Sayı: 2025-01/03) alınmıştır.
Hasta Onamı: Yazılı hasta onamı bu çalışmaya katılan hastalardan alınmıştır.
Hakem Değerlendirmesi: Dış bağımsız.
Yazar Katkıları: Konsept – SD, HG, OÇ, FKÇ; Tasarım – SD, HG, OÇ, FKÇ; Denetim - SD, HG, OÇ, FKÇ; Kaynaklar – SD, HG, OÇ, FKÇ; Malzemeler - OÇ, FKÇ; Veri Toplama ve/veya İşleme – SD, OÇ, FKÇ; Analiz ve/veya Yorum - FKÇ, SD; Literatür Taraması - SD, OÇ,; Yazma - OÇ, SD; Eleştirel İnceleme - OÇ, SD.
Çıkar Çatışması: Yazarlar, çıkar çatışması olmadığını beyan etmiştir.
Finansal Destek: Bu çalışma için herhangi bir kurumdan finansal destek alınmamıştır.

Ethics Committee Approval: Ethics committee approval was received for this study from the ethics committee of Erzincan Binali Yıldırım University (Date: 09.01.2025, No: 2025-01/03).
Informed Consent: Written informed consent was obtained from patients who participated in this study.
Peer-review: Externally peer-reviewed.
Author Contributions: Concept - SD, HG, OÇ, FKÇ; Design- SD, HG, OÇ, FKÇ; Supervision- SD, HG, OÇ, FKÇ; Resources- SD, HG, OÇ, FKÇ; Materials - OÇ, FKÇ; Data Collection and/or Processing- SD, OÇ, FKÇ; Analysis and/or Interpretation- FKÇ, SD; Literature Search- SD, OÇ,; Writing Manuscript-OÇ, SD; Critical Review-OÇ, SD..
Conflict of Interest: The authors have no conflicts of interest to declare.
Financial Disclosure: No financial support was received from any institution for this study.

References

Carey M.C. (1992). Pathogenesis of gallstones. *Recenti Prog Med*., 83(7-8), 379-91. PMID: 1529152.

Costa C.J., Nguyen M.T.T., Vaziri H. & Wu G.Y. (2024). Genetics of Gallstone Disease and Their Clinical Significance: A Narrative Review. *J Clin Transl Hepatol.,* 12(3), 316-326. doi: 10.14218/JCTH.2023.00563.

Di Ciaula A. & Portincasa P. (2018). Recent advances in understanding and managing cholesterol gallstones [version 1; peer review: 2 approved]. *F1000Research,* 7(F1000 Faculty Rev), 1529. https://doi.org/10.12688/f1000research.15505.1

Gu Q., Zhou G. & Xu T. (2020). Risk factors for gallstone disease in Shanghai: an observational study. *Medicine,* 99(3), e18754.

Ha B.J. & Park S. (2018). Classification of gallstones using Fourier-transform infrared spectroscopy and photography. *Biomater Res.*, 22,18. doi: 10.1186/s40824-018-0128-8. PMID: 30038795; PMCID: PMC6052647.

Internal Clinical Guidelines T. National Institute for Health and Care Excellence: Clinical Guidelines. Gallstone Disease: Diagnosis and Management of Cholelithiasis, Choledocholithiasis and Choledocholithiasis. London: National Institute for Health and Care Excellence (UK) Copyright (c) *National Clinical Guideline Centre*, 2014;2014.

Jayasoma K., Koralegedara N.H., Dharmapala A. & Chandrajith R. (2022). Microstructural and Geochemical Characterization of Gallstones: Implication for Biomineralization. *Biol Trace Elem Res.,* 200(12):4891-4902. doi: 10.1007/s12011-021-03076-4. Epub 2022 Jan 28. PMID: 35089502.

Jones M.W., Weir C.B. & Ghassemzadeh S. Gallstones (Cholelithiasis) [Updated 2024 Aug 17]. In: StatPearls [Internet]. Treasure Island (FL): *StatPearls Publishing*; 2025.

Jukić T., Margetić B.A., Jakšić N. & Boričević V. (2023). Personality differences in patients with and without gallstones. *J Psychosom Res.,* 169,111322. doi: 10.1016/j.jpsychores.2023.111322. Epub 2023 Mar 27. PMID: 37018955.

Kim I.S., Myung S.J., Lee S.S., Lee S.K. & Kim M.H. (2003). Classification and nomenclature of gallstones revisited. *Yonsei Med J.*, 44(4),561-70. doi: 10.3349/ymj.2003.44.4.561. PMID: 12950109.

Lammert F., Gurusamy K., Ko C.W., Miquel J.F., Méndez-Sánchez N., Portincasa P., van Erpecum K.J., van Laarhoven C.J. & Wang D.Q. (2016). Gallstones. *Nat Rev Dis Primers*., 28(2), 16024. doi: 10.1038/nrdp.2016.24. PMID: 27121416.

Lee B.J.H., Yap Q.V., Low J.K., Chan Y.H., Shelat V.G. (2022). Cholecystectomy for asymptomatic gallstones: Markov decision tree analysis. *World J Clin Cases.,* 10(29),10399-10412. doi: 10.12998/wjcc.v10.i29.10399. PMID: 36312509; PMCID: PMC9602237.

Liu J.S., Huang C.S. & Lien H.H. (2002). Structural analysis of gallstones with thin-section petrographic microscopy: a study of 100 gallstones from Taiwanese patients. *J Lab Clin Med*., 140(6), 387-90. doi: 10.1067/mlc.2002.129309. PMID: 12486405.

Liu, J.-X., Liu, Y., & Shen, Q.-H. Study on the correlation of electron spin resonance with pigment gallstones and trace Cu2+, Fe3+ in diet. *2025 Scientific Reports*, 15(1). https://doi.org/10.1038/s41598-025-93870-0

Nakeeb A., Comuzzie A.G., Martin L., Sonnenberg G.E., Swartz-Basile D., Kissebah A.H. & Pitt H.A. (2002). Gallstones: genetics versus environment. *Ann Surg*., 235(6), 842-9. doi: 10.1097/00000658-200206000-00012. PMID: 12035041; PMCID: PMC1422514.

Pak M. & Lindseth G. (2016). Risk Factors for Cholelithiasis. *Gastroenterol Nurs*., 39(4), 297-309. doi: 10.1097/SGA.0000000000000235. PMID: 27467059; PMCID: PMC8802735.

Parra-Landazury N.M., Cordova-Gallardo J. & Méndez-Sánchez N. (2021). Obesity and Gallstones. *Visc Med.*, 37(5), 394-402. doi: 10.1159/000515545. Epub 2021 Apr 23. PMID: 34722722; PMCID: PMC8543292.

Portincasa, P., Moschetta, A. & Palasciano, G. (2006). Cholesterol gallstone disease. *Lancet* 368, 230–239.

Peter A., Cozmuta L.M., Nicula C., Cozmuța A.M., Vulpoi A., Barbu-Tudoran L., Magyari K., Todea M., Baia L. & Pop FG. (2006). Multi-analyses of gallstones and correlation between their properties with the laboratory results. *Anal Biochem.*, 15;593, 113587. doi: 10.1016/j.ab.2020.113587. Epub 2020 Jan 21. PMID: 31978457.

Sebghatollahi V., Parsa M., Minakari M. & Azadbakht S. (2023). A clinician's guide to gallstones and common bile duct (CBD): A study protocol for a systematic review and evidence-based recommendations. *Health Sci Rep.,* 6(9),e1555. doi: 10.1002/hsr2.1555.

Shaffer EA. (2006). Gallstone disease: Epidemiology of gallbladder stone disease. *Best Pract Res Clin Gastroenterol.,* 20(6), 981-96. doi: 10.1016/j.bpg.2006.05.004. PMID: 17127183.

Singh V.K., Jaswal B.S., Sharma J. & Rai P.K. (2020).Analysis of stones formed in the human gall bladder and kidney using advanced spectroscopic techniques. *Biophys Rev.,* 12(3), 647-668. doi: 10.1007/s12551-020-00697-2. Epub 2020 May 14. PMID: 32410185; PMCID: PMC7311631.

Stinton L.M. & Shaffer E.A. (2012). Epidemiology of Gallbladder Disease: Cholelithiasis and Cancer. *Gut and Liver*, 6,172-187.

Tazuma S. (2006). Gallstone disease: Epidemiology, pathogenesis, and classification of biliary stones (common bile duct and intrahepatic). *Best Pract Res Clin Gastroenterol.,* 20(6), 1075-83. doi: 10.1016/j.bpg.2006.05.009. PMID: 17127189.

Trotman BW. (1991). Pigment gallstone disease. *Gastroenterol Clin North Am.*, 20(1):111-26. PMID: 2022417.

Research Article *Araştırma Makalesi* DOI: 10.5281/zenodo.15739497

Photometric Observations and Refined System Parameters of the High-Density Gas Giant Hat-P-20 b

Yüksek Yoğunluklu Gaz Devi HAT-P-20 b'nin Fotometrik Gözlemleri ve İyileştirilmiş Sistem Parametreleri

Nazlı KARAMAN
Adıyaman University, Golbasi Vocational School, Department of Electric and Energy, Adıyaman, Türkiye

Abstract

HAT-P-20 b is a dense, hot Jupiter discovered by the HATNet project, orbiting a K-type main-sequence star with high stellar activity. It exhibits an unusually high density (~13.8 g/cm³), a short orbital period (~2.9 days), and a close-in orbit (~0.0361 AU), making it a notable case among similar gas giants. With a mass of ~7.25 M_J and a radius of 0.867 R_J, the planet presents key challenges in understanding planetary structure and composition. This study presents a photometric analysis of HAT-P-20 b based on transit observations conducted on January 15, 2017, using the ground-based ADYU60 telescope. Data reduction was performed with AstroImageJ (AIJ), and transit modeling was carried out using EXOFAST. The derived light curve yielded refined system parameters: $M_P = 7.09^{+0.26}_{-0.24}\, M_J$, $R_P = 0.84 \pm 0.2\ R_J$, $a = 0.0357 \pm 0.0006\, AU$. These results are in agreement with previous studies within the expected uncertainties. Transit timing analysis was also performed to explore potential variations, yielding a refined minimum transit time of $T_0 = 2457769.357408^{+0.001403}_{-0.001476}$ BJD_{TDB}.These findings enhance the structural and dynamical understanding of the HAT-P-20 system and offer valuable input for future investigations of possible additional bodies.

Keywords: Stars: planetary systems, Exoplanets, Individual: HAT-P-20, Transit Observations

Öz

HAT-P-20 b, HATNet projesi kapsamında keşfedilen ve yüksek yıldız aktivitesine sahip bir K tipi ana kol yıldızının etrafında dolanan yoğun bir sıcak Jüpiter gezegendir. Yaklaşık 13,8 g/cm³ gibi sıra dışı yüksek bir yoğunluğa, kısa bir yörünge periyoduna (~2,9 gün) ve yıldızına yakın (~0,0361 AU) bir yörüngeye sahiptir; bu özellikleriyle benzer gaz devleri arasında dikkat çekmektedir. Yaklaşık 7,25 Jüpiter kütlesinde ve 0,867 Jüpiter yarıçapında olan gezegen, iç yapısına ilişkin önemli soruları gündeme getirmektedir. Bu çalışmada, 15 Ocak 2017 tarihinde yer tabanlı ADYU60 teleskobuyla gerçekleştirilen geçiş gözlemlerine dayalı fotometrik analiz sunulmaktadır. Veri indirgeme işlemleri AstroImageJ (AIJ) yazılımı ile yapılmış, geçiş modellemeleri ise EXOFAST yazılımı kullanılarak gerçekleştirilmiştir. Elde edilen ışık eğrisinden sistemin güncellenmiş parametreleri hesaplanmıştır: $M_P = 7.09^{+0.26}_{-0.24}\, M_J$, $R_P = 0.84 \pm 0.2\ R_J$, $a = 0.0357 \pm 0.0006\, AU$. Bu sonuçlar, beklenen belirsizlikler dahilinde önceki çalışmalarla uyumludur. Ayrıca, geçiş zamanlaması analizi yapılarak potansiyel varyasyonlar araştırılmış ve minimum geçiş zamanı $T_0 = 2457769.357408^{+0.001403}_{-0.001476}\ BJD_{TDB}$ olarak belirlenmiştir. Bu bulgular, HAT-P-20 sisteminin yapısal ve dinamik özelliklerinin daha iyi anlaşılmasına katkı sağlamaktadır ve sistemde olası ek cisimlerin araştırılması için değerli veriler sunmaktadır.

Anahtar Kelimeler: Yıldızlar: Gezegen Sistemleri, Ötegezegenler, HAT-P-20 sistemi, Geçiş Gözlemi

Sorumlu Yazar/Corresponding Author:
Nazlı Karaman
E-mail:nkaraman@adiyaman.edu.tr

Geliş Tarihi/Received 01.05.2025
Kabul Tarihi/Accepted 20.06.2025
Yayın Tarihi/ Publication Date 27.06.2025

Cite this article
Karaman N. (2025) Photometric Observations and Refined Systems Parameters of The High-Density Gas Giant HAT-P-20b. *Journal of Anatolian Physics and Astronomy*, 4(1), 32-37

Introduction

Exoplanets are defined as planetary systems orbiting stars outside the Solar System. The first exoplanet was discovered in 1992 around the pulsar PSR B1257+12 (Wolszczan & Frail, 1992), but the real breakthrough in this field occurred with the discovery of 51 Pegasi b in 1995 (Mayor & Queloz, 1995). Since that time, thousands of exoplanets have been discovered, and many of their various physical properties have been studied in detail. The investigation of exoplanets is significant not only for understanding the structure and dynamics of planets but also for identifying potentially habitable environments beyond the Solar System. Various methods have been developed for the discovery of exoplanets. Among these methods, the transit method is one of the most common and successful techniques for exoplanet detection. This method relies on observing how much a planet obscures or dims the light of its host star as it passes in front of it. During the transit event, when a planet passes in front of the star, there is a small yet measurable decrease in the star's brightness. This decrease varies depending on the size of the planet, with larger planets blocking more starlight. Recently, there has been a rapid increase in the discovery rate of exoplanets using the transit method (Huang et al., 2015). The transit method typically consists of several basic stages. First, the star's brightness is continuously monitored. If a repetitive and regular decrease in the star's light is observed, this may indicate that a planet is passing in front of the star. The duration and depth of the light reduction provide information about the planet's size and its distance from the star (Seager, 2010). For example, by analyzing the changes in light during a planet's transit in front of a star, it is possible to calculate the planet's diameter and orbital period. The transit method has achieved significant success, particularly through space-based observation projects such as the Kepler Space Telescope (Borucki et al., 2009). Kepler has proven the efficiency of this method by discovering numerous exoplanets. However, the transit method also has some limitations (Fischer, ExoDetectTech). In particular, planets can only be detected when they transit at specific angles; therefore, if planets are not in the correct plane of the system, they may go undetected. Additionally, the light changes observed during the transit event can be affected by other factors (such as star spots or other astronomical events), complicating detection and analysis processes.

The TTV (Transit Timing Variation) method is a type of transit method used to discover and characterize exoplanets (Agol et al., 2005). This method aims to gather information about the presence of other planets by examining variations in a planet's transit timing, and it is especially effective in multi-planet systems. The TTV method begins with careful documentation of the transits of a planet as it passes in front of its star. These transits are expected to occur within a certain time interval. However, if there are multiple planets in the system, the gravitational interactions between their masses and orbits cause small but measurable changes in the timings of the planets' transits. This phenomenon is known as TTV. For instance, if one planet approaches another, its transit timing may shift forward or backward. Detailed examination of the changes in transit timings can provide insights into the presence of other planets in the system. According to Veras et al. (2011), it is suggested that at least 50 consecutive transit observations are necessary to precisely detect a third body (planet) and its orbit if it is thought to exist in the system. Therefore, precise determination of mid-transit times across numerous events is crucial for detecting both the system's orbital parameters and the presence of additional bodies. The TTV method provides information by evaluating the relationship between the gravitational effects of planets and geometry. Changes in transit timings result from the gravitational influences of planets, and this data can help us learn more about the mass and orbital characteristics of these planets (Agol et al., 2005). The advantages of the TTV method include the ability to detect the presence of other planets in multi-planet systems and to estimate the masses of these planets. Additionally, it offers opportunities to study orbital dynamics, aiding our understanding of the structure of the system. The TTV method has led to the discovery of a large number of exoplanets using data obtained from missions such as the Kepler Space Telescope, and it continues to be an important tool in future exoplanet research with the potential to contribute to the discovery of hidden planets within systems. HAT-P-20 b stands out as an interesting planet discovered in 2010.

This gas giant orbits the K-type main-sequence star HAT-P-20. Recent studies have contributed to our better understanding of its physical and orbital characteristics. HAT-P-20 b has a mass of approximately 7.25 MJ and a radius of 0.867 RJ, making it one of the densest known exoplanets (average density: ~13.8 g/cm^3). It orbits very close to its star (0.0361 AU) and completes a revolution in about 2.9 days (Bakos et al., 2010). This study shares the results obtained from transit observation data of the HAT-P-20 exoplanet taken on January 15, 2017, using the ADYU60 telescope. Section 2 provides the characteristics of these observations, as well as the processes of data reduction and modeling for the light curves. In Section 3, the newly obtained system parameters from the modeling results are presented and discussed.

Observation

The transit observation of HAT-P-20 b was conducted using the ADYU60 telescope, which has a 60 cm diameter primary mirror and is equipped with a high-speed and high-sensitivity 1K x 1K Andor iKon-M 934 CCD camera, at the Adıyaman University Astrophysics Application and Research Center. The details of the observations are given in Table 1. The observation was made on January 15, 2017, using the Johnson R filter with an exposure time of 60 s. The scheduling of the observation times for exoplanet transit was facilitated by the Exoplanet Transit Database (ETD; April 24, 2025). The times listed on the ETD site indicate the start and end times of the transit. Therefore, the observations were made starting earlier and ending later than the durations specified on the ETD to ensure better results for the light curves. Additionally, nights with stable atmospheric conditions and low sky background were selected to maximize data quality.

Table 1. Observation Details for HAT-P-20 b Transit on January 15, 2017

Obs. Date	Obs. Start→End (UT)	Predicted TT (UT)	Filter	Exposure	N_{obs} (Total Frame)	Airmass
15.01.2017	19:00→21:45	21:18→23:04	R	60	156	1.19→1.06→1.03

*Obs: Observation, TT: Transit Time, UT: Universal Time

Data Reduction

Calibration, photometry, and detrending were performed using AstroImageJ (AIJ; Collins et al., 2017a). During the data reduction process, bias subtraction and flat field corrections were applied. Three reference stars were used during the data reduction (see Table 2). All selected reference stars were analyzed in the same order for each analysis. During these analyses, the aperture and annulus radii of the target star and the reference stars were determined using the Radial Profile feature of the AIJ program. To minimize modeling residuals during differential photometry (Collins et al., 2017a), a variation of the aperture sizes was allowed, changing by a factor of 1.2 times the FWHM (full-width-half-maximum) value for each image. Detrending was applied to achieve the best modeling for the light curves. The determination of the detrending parameters that yielded the best modeling results was based on changes in the BIC (Bayesian Information Criterion) values from the "Fitting" module of AIJ (Collins et al., 2017b). Among the tested detrending parameters, only "airmass" yielded statistically significant improvements; therefore, it was the sole detrending factor applied in the light curve modeling. Additionally, the time conversions from JD_{UTC} to BJD_{TDB} were performed using AIJ. The light curve and its model with the EXOFAST software (Eastmann et al., 2013) obtained as detailed in the next section are presented in Figure 1.

Table 2. Some properties of target and comparison stars for the HAT-P 20 b system

Source Name	Source type	RAJ2000	DEJ2000	K (mag)
HAT-P 20	Target	111.916469	+24.336630	8.601
TYC 1910-871-1	Comparison	111.961697	+24.318037	10.225
2MASS 07274451+2418097	Comparison	111.935496	+24.302706	10.938
2MASS 07272798+2419213	Comparison	111.866586	+24.322594	11.925

Light Curve Analysis

To model the transit light curves of the star-planet system, the EXOFAST program (Eastman et al., 2013) was utilized, which allows the calculation of certain physical parameters of the system and the estimation of their uncertainties. The EXOFAST program **uses** the Markov Chain Monte Carlo (MCMC) method for parameter estimation. The Monte Carlo algorithm generates random values for the parameters iteratively, ensuring that the newly generated values are independent of the previous ones. EXOFAST constructs probabilities that indicate how likely these randomly produced independent parameters are within the data (Eastman et al., 2013).

The radial velocity (RV) data needed to model the HAT-P-20 system were obtained from the work of Bakos et al. (2010). Additionally, some initial values (logg*, Teff, and [Fe/H]) were provided during the EXOFAST modeling. Some of these initial values were used from the literature (Bakos et al., 2010). In modeling with EXOFAST, the orbit of the system was assumed to be circular. The updated system parameters resulting from the modeling and their comparison with literature values are given in Table 3.

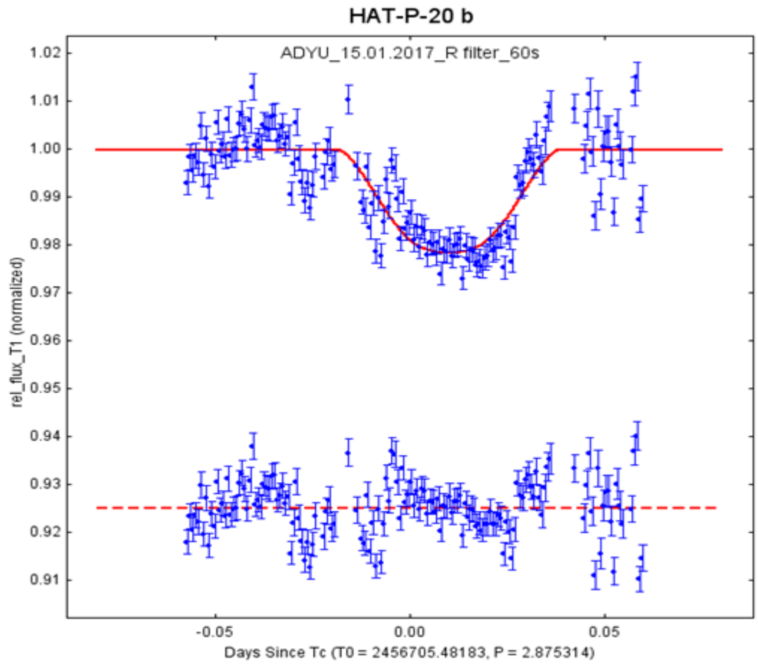

Figure 1. Transit light curve of HAT-P-20 b from ADYU60 (top, blue points with error bars) and residuals from the EXOFAST model (bottom, red line).

The mid-transit times required for TTV (Transit Timing Variation) analyses used to detect the presence of a third body in the system and to enhance the precision of the orbital parameters were also determined for the transit light curve obtained in this study. The mid-transit time obtained is given in Table 3.

Table 3. HAT-P-20 system parameters from this study compared with Bakos et al. (2010) and Esposito et al. (2017).

Parameters	Units	This work	Bakos et al. (2011)	Esposito et al. (2017)
Stellar Parameters				
M_*	Mass $(M_\odot)$	$0.728^{+0.041}_{-0.036}$	0.756 ± 0.028	0.742 ± 0.042
R_*	Radius $(R_\odot)$	$0.665^{+0.019}_{-0.018}$	0.694 ± 0.021	0.6796 ± 0.0054
$\log g_*$	Surface gravity (cgs)	$4.655^{+0.015}_{-0.014}$	4.450 ± 0.200	4.643 ± 0.020
ρ_*	Density (cgs)	$3.501^{+0.19}_{-0.17}$	…	2.36 ± 0.16
Planetary Parameters				
M_P	Mass (M_J)	$7.095^{+0.266}_{-0.243}$	7.246 ± 0.187	7.22 ± 0.36
R_P	Radius (R_J)	$0.843^{+0.026}_{-0.025}$	0.867 ± 0.033	1.025 ± 0.053
$\log g_P$	Surface gravity (cgs)	4.393 ± 0.018	4.38 ± 0.03	4.231 ± 0.019
ρ_P	Density (cgs)	$14.69^{+1.03}_{-0.98}$	13.78 ± 1.50	8.31 ± 0.38
T_{eq}	Equilibrium temperature (K)	950 ± 18	970 ± 23	964 ± 10
Orbital Parameters				
P	Period (days)	2.875314 ± 0.000003	2.875317 ± 0.000004	$2.875316938 \pm 0.00000019$
a	Semi-major axis (AU)	$0.0357^{+0.0007}_{-0.0006}$	0.0361 ± 0.0005	0.03593 ± 0.00029
Transit Parameters				
R_P/R_*		0.1304 ± 0.0016	0.1284 ± 0.0016	0.155 ± 0.010
a/R_*		$11.56^{+0.20}_{-0.19}$	11.17 ± 0.29	11.36 ± 0.25
i	Inclination (deg)	$86.4^{+0.2}_{-0.1}$	86.8 ± 0.2	86.88 ± 0.31
b	Impact parameter	$0.725^{+0.029}_{-0.031}$	$0.631^{+0.025}_{-0.028}$	0.622 ± 0.059
T_{14}	Transit duration (days)	$0.0688^{+0.0025}_{-0.0024}$	0.0770 ± 0.0008	0.07900 ± 0.00052
T_0	Mid-Transit Time (BJD_{TDB})	$2457769.357408^{+0.001403}_{-0.001476}$		

Results and Conclusion

The discovery of exoplanets plays a critical role in understanding the structure of the universe and the potential for extraterrestrial life; therefore, detailed studies of planets such as HAT-P-20 b present significant opportunities for the scientific community. In this context, the light curve obtained from ADYU60 was processed using the AIJ program for reduction and differential photometry. It is modeled with the EXOFAST program to update the system parameters of the HAT-P-20 system. The obtained reduced and modeled light curve is given in Figure 1.

The scatter observed in the light curve is may be attributed to the high stellar activity reported by Bakos et al. (2011) and the atmospheric conditions on the nights of observation. Furthermore, it can be seen that the light curve modeling results obtained from EXOFAST are in agreement with the literature.

The updated physical parameters of the system, compared with data from the literature, are presented in Table 3. For HAT-P-20 b, some of these system parameters include $M_P = 7.095^{+0.266}_{-0.243}$, $R_P = 0.843^{+0.026}_{-0.025} R_J$, $a = 0.0357^{+0.0007}_{-0.0006} AU$. A review of these values indicates compatibility within the range of uncertainties when compared with literature values.

The minimum values of the transit times required for TTV (Transit Timing Variation) analysis are shared in Table 3. Further observations will continue in the coming periods with various projects to achieve more precise analyses of the physical and system parameters for this system and to facilitate TTV analyses.

Acknowledgements: *I would like to thank the Adıyaman University Astrophysics Application and Research Center for their support in obtaining the observational data.*

Hakem Değerlendirmesi: *Dış bağımsız.*
Çıkar Çatışması: *Nazlı KARAMAN, çıkar çatışması olmadığını beyan etmiştir.*
Finansal Destek: Bu çalışma için herhangi bir kurumdan finansal destek alınmamıştır.

Peer-review: *Externally peer-reviewed.*
Conflict of Interest: *Nazlı KARAMAN has no conflicts of interest to declare.*
Financial Disclosure: No financial support was received from any institution for this study.

References

Agol, E., Steffen, J., Sari, R. & Clarkson, W. (2005) On detecting terrestrial planets with timing of giant planet transits, *Monthly Notices of the Royal Astronomical Society (MNRAS), 359*(2), 567-579. http://dx.doi.org/10.1111/j.1365-2966.2005.08922.x

Bakos, G.A., Hartman, J., Torres, G., Latham, D. W., Kovács, G., Noyes, R. W., Fischer, D. A., Johnson, J. A., Marcy, G. W., Howard, A. W., Kipping, D., Esquerdo, G. A., Shporer, A., Béky, B., …& Sári, P. (2011). HAT-P-20b–HAT-P-23b: Four Massive Transiting Extrasolar Planets. *The Astrophysical Journal*,742(2) 116-135. http://dx.doi.org/10.1088/0004-637X/742/2/116

Borucki, W. J., Koch, D., Jenkins, J., …& Tarter, J. (2009). Kepler's Optical Phase Curve of the Exoplanet HAT-P-7b. *Science*, 325(5491), 709. https://doi.org/10.1126/science.1178312

Collins, K. A., Kielkopf, J. F., Stassun, K. G. & Hessman, F.V. (2017a). Astroimagej: Image Processing and Photometric Extraction for Ultra-Precise Astronomİcal Light Curves. *The Astronomical Journal*, 153(2), 77-90. http://dx.doi.org/10.3847/1538-3881/153/2/77

Collins, K.A., Kielkopf, J.F. & Stassun, K.G., (2017b). Transit Timing Variation Measurements Of Wasp-12b And Qatar-1b: No Evidence Of Additional Planets. *Astronomical Journal*, 153(2), 78. http://dx.doi.org/10.3847/1538-3881/153/2/78.

Eastman, J., Gaudi, B.S. & Agol, E., 2013. EXOFAST: A Fast-Exoplanetary Fitting Suite in IDL, *Publications of the Astronomical Society of the Pacific*, 125(923), 83-109. http://dx.doi.org/10.1086/669497.

Esposito, M., Covino, E., Desidera, S., Mancini, L., Nascimbeni, V., …& Turner, O.D. (2017). The GAPS Programme with HARPS-N at TNG XIII. The orbital obliquity of three close-in massive planets hosted by dwarf K-type stars: WASP-43, HAT-P-20 and Qatar-2. *Astronomy&Astrophysics* 601 (A53), 16. https://doi.org/10.1051/0004-6361/201629720 ETD,2025, April

24. http://var2.astro.cz/ETD/

Huang, C. X., Hartman, J. D., Bakos, G. Á., Penev, K., Bhatti, W. ; Bieryla, A., de Val-Borro, M., Latham, D. W., Buchhave, L. A., …& Sári, P. (2015). HAT-P-56b: An Inflated Massive Hot Jupıter Transiting A Bright F Star Followed Up with K2 Campaign 0 Observations. *The Astronomical Journal*,150 (3), 85-96. https://doi.org/10.1088/0004-6256/150/3/85

Mayor, M. and Queloz, D., (1995). A Jupiter-mass companion to a solar-type star. Nature, 378(6555), 355−359. https://doi.org/10.1038/378355a0

Seager, S. (2010). Exoplanets, *The Univercity of Arizona Press*, p.55-78.

Veras, D., Ford, E. B. & Payne, M. J. (2011). Quantifying the Challenges of Detecting Unseen Planetary Companions with Transit Timing Variations, The Astrophysical Journal, 727 (2), 74-98. https://doi.org/10.1088/0004-637X/727/2/74

Wolszczan, A. and Frail, D.A., 1992. A planetary system around the millisecond pulsar PSR1257 + 12. *Nature*, 355 (6356), 145−147. https://doi.org/10.1038/355145a0

Research Article *Araştırma Makalesi* DOI: 10.5281/zenodo.15739554

ATATÜRK ÜNİVERSİTESİ YAYINLARI ATATURK UNIVERSITY PUBLICATIONS

Analysis of Absorbing Aerosols for Ground-Based Astronomical Observatories in Türkiye

Türkiye'deki Yer Tabanlı Astronomi Gözlemevleri için Soğurucu Aerosollerin Analizi

Sima AYDIN
Atatürk University, Faculty of Science, Department of Astronomy and Space Sciences, Erzurum, Türkiye

Fethullah POLAT
Atatürk University, Faculty of Science, Department of Astronomy and Space Sciences, Erzurum, Türkiye

Kazım KABA
Atatürk University, Faculty of Science, Department of Astronomy and Space Sciences, Erzurum, Türkiye

Abstract

In this study, the impact of aerosols on ground-based astronomical observations in Türkiye was examined, and their spatial and temporal variations were assessed. Satellite data was used in the study due to its advantage of wide area coverage. The absorbing aerosol index (AAI) product, derived from multi-sensor observations, was used in the research. Positive AAI (PAAI) is a measurement of the concentration of absorbing aerosols (such as dust, smoke, volcanic ash, etc.) in the atmosphere. High PAAI values are often indicative of significant weather events, such as dust storms, forest fires, and volcanic eruptions. Therefore, PAAI data can serve as an important indicator for atmospheric conditions affecting astronomical observations. PAAI values can provide significant insights into the evaluation of the accuracy of astronomical observation data, the planning of observation programs, and selection of suitable observation sites. Understanding the impact of atmospheric aerosols on photometric and spectroscopic data is critical for improving the success of future high-precision astronomical observations. The present study reveals the current aerosol characteristics of the observatories in detail. The global average PAAI value for 2024 is calculated to be 0.34, which is lower than the 45-year long-term global average of 0.38. However, the average PAAI value for Türkiye in 2024 was 0.39, which is consistent with the long-term global average. These findings indicate that the observatories in Türkiye are closely aligned with the global average aerosol conditions.

Keywords: Absorbing Aerosol Index, Astronomy, Remote Sensing, Spatiotemporal Analysis, Türkiye

Öz

Bu çalışmada, Türkiye'deki yer tabanlı astronomik gözlemevleri için, aerosollerin mekânsal ve zamansal değişimleri değerlendirilmiştir. Çalışmada geniş alanları kapsaması nedeniyle uydu verileri tercih edilmiş, çoklu sensör gözlemlerinden türetilen soğurucu aerosol indeksi kullanılmıştır. İndeksin pozitif değerleri, atmosferdeki ışığı soğuran aerosollerin (toz, duman, volkanik kül gibi) yoğunluğunu ölçen bir parametredir. Yüksek indeks değerleri, genellikle toz fırtınaları, orman yangınları ve volkanik patlamalar gibi büyük ölçekli atmosferik olayların varlığını göstermektedir. Bu nedenle, bu veriler astronomik gözlemler için atmosferik koşulların belirlenmesinde önemli bir gösterge olarak kullanılabilir. Aerosol değerleri, astronomik gözlem verilerinin doğruluk düzeylerinin değerlendirilmesi, gözlem programlarının planlanması ve uygun gözlem yerlerinin seçimi açısından önemli katkılar sunabilir. Atmosferik aerosollerin fotometrik ve spektroskopik veriler üzerindeki etkilerinin anlaşılması, gelecekteki yüksek hassasiyetli astronomik gözlemlerin başarısını artırmak için kritik öneme sahiptir. Bu çalışma ile Türkiye'deki gözlemevlerinin mevcut aerosol özellikleri ayrıntılı biçimde ortaya konmuştur. 2024 yılı için küresel ortalama aerosol değeri 0.34 olarak hesaplanmış ve bu değer 45 yıllık uzun dönem küresel ortalama olan 0.38'in altında bulunmuştur. Öte yandan, Türkiye'nin 2024 yılı ortalama aerosol değeri 0.39 olarak ölçülmüş ve uzun dönem küresel ortalama ile uyumlu olduğu belirlenmiştir. Bu bulgular, Türkiye'deki gözlemevlerinin, atmosferik aerosol koşulları açısından dünya ortalamasına yakın değerlere sahip olduğunu göstermektedir.

Anahtar Kelimeler: Soğurucu Aerosol İndeksi, Astronomi, Uzaktan Algılama, Mekansal-Zamansal Analiz, Türkiye

Sorumlu Yazar/Corresponding Author: Sima Aydın
E-mail: simaaydin20@gmail.com

Geliş Tarihi/Received 28.04.2025
Kabul Tarihi/Accepted 19.06.2025
Yayın Tarihi/ Publication Date 27.06.2025

Cite this article
Aydın, S., Polat, F., & Kaba, K. (2025) Analysis of Absorbing Aerosols for Ground-Based Astronomical Observatories in Türkiye. *Journal of Anatolian Physics and Astronomy*, 4(1), 38-50.

Introduction

Atmospheric aerosols (AA), defined as tiny particles suspended in the atmosphere, are a critical factor influencing the quality of observations at ground-based astronomical observatories. These tiny suspended particles, which include dust, soot, sea salt, and organic matter, interact with incoming electromagnetic radiation, causing scattering and absorption that reduce the clarity and accuracy of astronomical data. In particular, aerosols affect the extinction of light, sky brightness, and seeing conditions, which are essential parameters for high-resolution imaging and spectroscopy (Sánchez et al., 2007; Zhang et al., 2013; Mikhalev et al., 2019).

The impact of aerosols on optical and near-infrared wavelengths is of particular significance, because the scattering effects of these particles can significantly reduce the signal-to-noise ratio of faint celestial objects. Additionally, aerosol-related phenomena, such as Rayleigh and Mie scattering, result in wavelength-dependent distortions, which complicate data calibration and interpretation. The geographical location of observatories, including altitude, proximity to urban areas, and local meteorological conditions, plays a key role in determining aerosol concentrations and their optical properties (Sánchez et al., 2007; Zhang et al., 2013; Mikhalev et al., 2019).

Aerosols play a significant role in the diffusion of artificial light, contributing to the increased brightness of the night sky, which consequently diminishes the contrast of celestial objects against the sky (Cavazzani et al., 2020; Kocifaj and Bará, 2020). The diffusion process is influenced by the dimensions, shape, and composition of the aerosol particles. Deviations in the shapes of aerosol particles can substantially modify the spectral and angular properties of scattered light, thereby affecting observational results. The transparency of the atmosphere is a crucial factor in astronomical observations, and the presence of aerosols can significantly impact this transparency. Aerosols, by their nature, absorb and scatter incoming light, leading to increased extinction and decreased signal-to-noise ratios in collected data. Atmospheric aerosols are among the most significant parameters to be monitored in modern ground-based astronomy because of their potentially adverse impacts on observations. To summarize, the presence of atmospheric aerosols has been determined to have a substantial influence on ground-based astronomical observations, given their capacity to affect night sky brightness and atmospheric transparency. It is vital, therefore, that continuous monitoring and analysis of aerosol properties be performed in order to minimize their impact and ensure the accuracy of astronomical data.

The study of atmospheric aerosols is an area of research that is cross-disciplinary, covering aspects of physics, chemistry, atmospheric sciences and astronomy. It is therefore crucial to accurately determine the temporal and spatial variations of atmospheric aerosols. Various techniques are employed for the measurement of aerosols, including ground-based monitoring, aircraft sampling, and remote sensing. Ground-based monitoring frequently employs instruments such as sun photometers, which are commonly used to measure aerosol properties at specific locations (Holben et al., 1998; Verma et al., 2019). The use of remote sensing from satellites, such as the Moderate Resolution Imaging Spectroradiometer (MODIS) and the Visible Infrared Imaging Radiometer Suite (VIIRS), facilitates the acquisition of aerosol data on a large scale, thereby providing invaluable insights into the spatial and temporal aspects of aerosol distribution (Jackson et al., 2013; Levy et al., 2007; Remer et al., 2005).

In this regard, there are many valuable studies that use aerosol data in the literature. For example, Yoshioka et al. (2005) conducted a study on the effects of vegetation change and human land use on dust sources in North Africa, by absorbing aerosol index data. Balarabe et al. (2016) compared the temporal and spatial variability of the monthly mean aerosol index obtained from the OMI in Nigeria during the period 1984 - 2013. Kooreman et al. (2020) conducted a study to investigate the effects of clouds on the absorbing aerosol index at both small and large scales. Liu et al. (2020) conducted a study into the relationship between aerosol optical depth (AOD) and land use, as well as vegetation, in Central Asia using MODIS aerosol data. Shaylor et al. (2022) conducted a twenty-year (2001-2020) AOD assessment for Australia using MODIS data. Jiadan et al. (2023) investigated the spatiotemporal changes in AOD over Ukraine during the Russia-Ukraine war. Gan et al. (2024) conducted an analysis of the characteristics and changes in the three-dimensional spatial and temporal distribution of aerosol types in Central Asia using the Cloud–Aerosol Lidar and Infrared Pathfinder Satellite (CALIPSO) data from 2007 to 2021. Furthermore, a significant number of studies have been conducted on the subject of aerosol in Türkiye. Ozdemir et al. (2020) utilised aerosol classification methodologies based on AERONET products in the Eastern Mediterranean and Black Sea regions. Tutsak and Koçak (2020) conducted a study of the optical and microphysical properties of aerosols in the Eastern Mediterranean with the objective of distinguishing between different types of aerosols. Tuygun and Elbir (2020) conducted a long-term temporal analysis of the relationship between the AOD, and surface aerosol concentration, and the planetary boundary layer height along the southern coastline of Türkiye. Aslanoğlu et al. (2022) conducted a study of the dust climatology of the Eastern Mediterranean Basin utilising products derived from CALIPSO observations. Tariq et al. (2023)

analysed the AOD and dominant meteorological factors during the summer in Türkiye using remote sensing data. Osgouei and Kaya (2023) presented a comprehensive analysis of the spatiotemporal variation of satellite-based AOD in the Marmara Region of Türkiye between 2000 and 2021. Tuygun and Elbir (2023) investigated the long-term spatial and temporal variations in the atmospheric aerosol properties over Türkiye by reanalysis data from the Modern-Era Retrospective analysis for Research and Applications, Version 2 (MERRA-2). Tuygun and Elbir (2024) analysed of Copernicus Atmosphere Monitoring Service (CAMS) and AERONET data for the Eastern Mediterranean region. Işık et al. (2024) presented a long-term analysis of the MODIS and AERONET AOD data.

In this study, we examined of absorbing aerosols for the ground-based astronomical observations in Türkiye by reviewing their spatial and temporal variability. The study used satellite data, which is advantageous due to its wide area coverage. In this regard, the absorbing aerosol index (AAI) product, derived from multi-sensor observations, was employed. Consequently, this study represents a novel contribution to the scientific community in Türkiye by examining the absorbing aerosol time series of the observatory sites and using Positive AAI (PAAI) data for astronomical purposes for the first time. The study reveals the current aerosol properties of the observatories in detail. However, it is important to note that Türkiye is a neighboring country to the Sahara Desert, the world's largest aerosol/dust source, and is therefore affected by the dust transportation from the desert. Consequently, there is a necessity for more intensive monitoring and management of aerosols for the purpose of improving our understanding of climate, weather, air quality, agriculture and astronomy.

Data Sources and Methodology

This study investigates the aerosol values of major ground-based astronomical observatories in Türkiye during the period 1979-2024. Figure 1 and Table 1 provide coverage and information about the observatories that are of particular significance in this context. Türkiye is located between 26-45 east longitude and 36-42 north latitude, and consists of seven regions. The examined observatories differ in altitude and location, and cover six geographical regions of Türkiye.

The study used monthly average AAI data were obtained from multiple sensors. The multi-sensor AAI (MS-AAI) data comprise AAI data from the TOMS, GOME-1, SCIAMACHY, OMI, GOME-2A, GOME-2B and GOME-2C instruments (see Table 2). The dataset under consideration covers the period from 1978-November to the present, with the current software version being 1.9. The data demonstrate global coverage, with a pixel resolution of 1 degree (~100 km) (https://www.temis.nl/airpollution/absaai/#MS_AAI). The presence of highly absorbing aerosols in the Earth's atmosphere is indicated by the AAI. The most prevalent aerosol types in the AAI are desert dust and biomass-burning aerosols. The AAI data were calculated from reflectances measured at 340 and 380 nm by GOME-1, SCIAMACHY and GOME-2, and from reflectances measured at 354 and 388 nm by OMI (https://www.temis.nl/airpollution/absaai/).

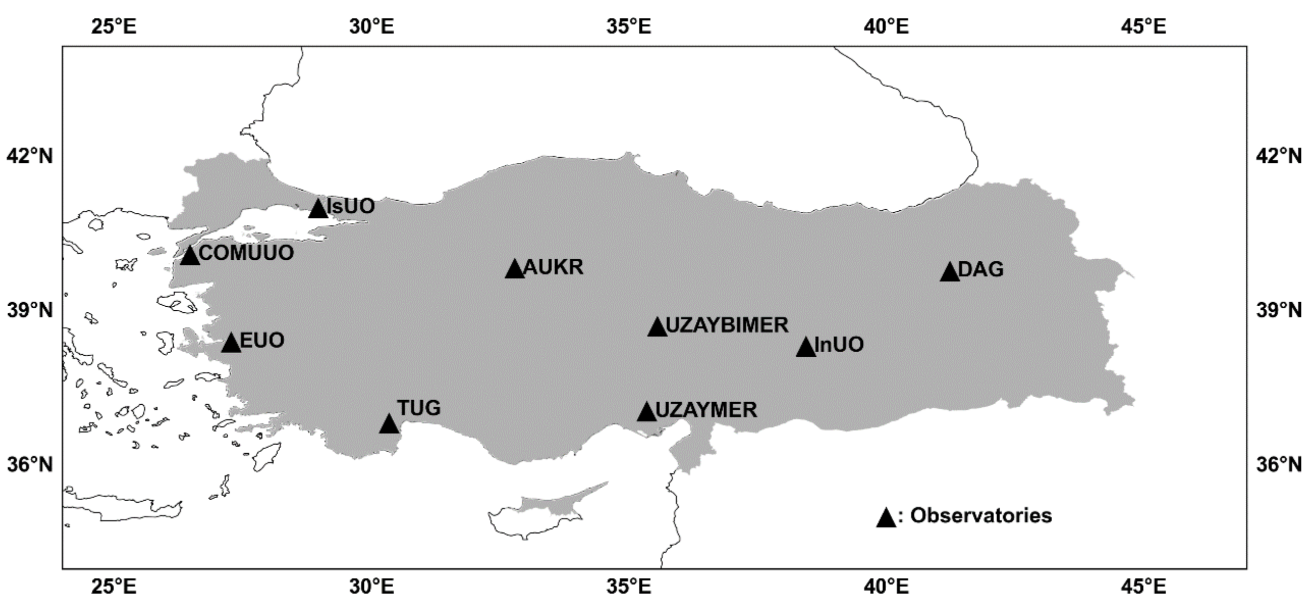

Figure 1 Spatial distribution of major ground-based astronomical observatories in Türkiye.

Table 1 Information of major ground-based astronomical observatories in Türkiye.

Observatory Site	City	Latitude (Degree)	Longitude (Degree)	Elevation (Meter)
Ankara University Kreiken Observatory (AUKR)	Ankara	39.84	32.78	1261
Çanakkale Onsekiz Mart University Ulupınar Observatory (COMU UO)	Çanakkale	40.10	26.48	397
Eastern Anatolia Obsevatory (DAG)	Erzurum	39.78	41.23	3144
Ege University Observatory (EUO)	İzmir	38.40	27.28	787
İnönü University Observatory (InUO)	Malatya	38.32	38.44	1013
İstanbul University Observatory (IsUO)	İstanbul	41.01	28.97	59
TÜBİTAK National Observatory (TUG)	Antalya	36.83	30.34	2461
Astronomy and Space Sciences Observatory Application and Research Center (UZAYBİMER)	Kayseri	38.71	35.55	1105
Space Sciences and Solar Energy Research and Application Center (UZAYMER)	Adana	37.06	35.35	125

The AAI is an index based on the comparison of measured UV reflectances with simulated Rayleigh reflectances. The simulated reflectances are calculated for an atmosphere that is both cloud-free and aerosol-free. The AAI is derived from a value termed “residue”, r, which is defined as follows (Tilstra et al., 2010). In the equation, the superscripts 'obs' and 'Ray' refer to measured and modelled reflections, respectively. The letter 'λ' is used to denote the first member of the wavelength pair (i.e. the shorter wavelength, 340 nm). It is hypothesized that the surface albedo employed in the simulations at this wavelength is equivalent to the surface albedo at the second wavelength, 380 nm. The surface albedo at 380 nm was determined by requiring the simulated reflectance to be equal to the measured reflectance at this wavelength (Tilstra et al., 2010). Positive r values in the equation are indicate the presence of absorbing aerosols, while negative or zero r values indicate their absence. Positive values of *r* are defined as PAAI (Tilstra et al., 2010).

$$r = -100 \log\left(\frac{R_\lambda^{obs}}{R_\lambda^{Ray}}\right) \tag{1}$$

Table 2 Satellite and sensor information used in producing aerosol product.

Platform	Agency	Instrument	Launch date	End of life date	Resource
Nimbus-7	NASA	TOMS, others	1978	1995	https://www.eoportal.org/satellite-missions/nimbus-7
ERS-2	ESA	GOME, others	1995	2011	https://www.eoportal.org/satellite-missions/ers-2
ENVISAT	ESA	SCIAMACHY, others	2002	2012	https://www.eoportal.org/satellite-missions/envisat
AURA	NASA, others	OMI, others	2004	Operational	https://www.eoportal.org/satellite-missions/aura
METOP-A	ESA, others	GOME-2, others	2006	2021	https://www.eoportal.org/satellite-missions/metop
METOP-B	ESA, others	GOME-2, others	2012	Operational	https://www.eoportal.org/satellite-missions/metop

TEMIS is a web-based service that facilitates the browsing and downloading of atmospheric satellite data. The satellite data products consist primarily of tropospheric trace gases and aerosol concentrations, but also encompass UV products, cloud information and surface albedo climatology. The satellite instruments used for these data sets were GOME, GOME-2, SCIAMACHY and OMI (https://www.temis.nl/intro.php). This study presents a data analysis of PAAI data with global coverage and a long temporal archive. Maps, tables, graphs and basic statistical indexes were used to illustrate the spatial and temporal analysis of the data. The data are presented as monthly averages, with a length of 528 months. In this study, time series methods were used for data analysis.

In this study, the monthly average absorbing aerosol index data obtained were analysed in both spatial and temporal dimensions. The analysis process can be divided into two main stages: firstly, spatiotemporal analysis to reveal spatial-temporal patterns; and secondly, time series analysis to determine long-term changes in the observatory locations. The global and Türkiye spatial distribution patterns for 2024 were created, and principal statistics were extracted. In the second stage of the study, time series were created for the astronomical observatories. Initially, the monthly, seasonal and annual variations of the series under consideration were subjected to rigorous examination, followed by the implementation of time series analysis utilising the monthly data. In this regard, the process entailed the separation of trends, seasonality and irregular components, followed by a thorough evaluation of the trends. The data processing, analysis and visualisation steps were performed utilising the Python programming language

Result and Discussion

Ground-based astronomical observations are of critical importance for understanding the nature of the universe and collecting important data on cosmological processes. However, such observations are vulnerable to the effects of physical and chemical processes in the atmosphere. In particular, aerosols in the atmosphere have the capacity to greatly affect the optical quality and accuracy of observations. Aerosol particles have the capacity to scatter, absorb and re-emit light from the Sun and other astronomical sources. These processes are critical factors that directly affect the quality of the photometric and spectroscopic data obtained at ground-based observing site.

Astronomical observatories in the Türkiye were determined as the study area. The dataset used in this study covers the period 1979-2024 (45 years). Using this large data archive, an average global and Türkiye PAAI map for 2024 year was created. This global map is shown in Figure 2 upper panel and the map of Türkiye, which is a sub-area of this map, is shown in the lower panel in the figure with values normalised to the range 0 - 1. The principal statistical values of the maps are presented in Table 3. PAAI is a measurement of the concentration of absorbing aerosols (dust, smoke, volcanic ash, etc.) in the atmosphere. The presence of high PAAI values are a reliable indicator of significant weather events, including dust storms, forest fires, and volcanic eruptions. The color dark blue on the map indicates a low aerosol concentration, whereas the red-maroon denotes high concentration.

The regions with the highest PAAI (i.e. of most severe conditions) are as follows: West Africa (particularly the Sahara Desert) due to dust, West Central Africa (i.e. the Congo Basin) due to biomass burning and forest fires in general, the Middle East and Central Asia due to drought and wind-blown agricultural soils, northern India and eastern China due to intense human activities, smoke and industrial pollutants, and the Amazon and parts of South America associated with dry season fires. Low PAAI regions (i.e. regions exhibiting optimal conditions) include southern South America, Chile and Argentina, inland Australia, parts of southern Africa, Greenland, Antarctica, the Arctic regions, and extensive areas of the Pacific and Atlantic oceans. The optimal conditions for ground-based astronomical observatories are characterized by a low PAAI, i.e., a clean, absorbing aerosol-free atmosphere. It has been determined that the Atacama Desert in Chile, Hawaii, Namibia (where levels of PAAI are comparatively low), and the Canary Islands (where medium levels of PAAI occur, and occasional effects from Saharan dust may be experienced) are all areas that offer optimal observation opportunities. The regions that present significant challenges (i.e. high PAAI) include northern India and central Africa (e.g. Congo and Chad), as well as eastern China. In summary, low PAAI values are particularly evident on the map in the western slopes of the Andes (on the Chilean side), Hawaii, southern Namibia, and certain inland regions of Australia. In order to facilitate the collection of scientific observations (particularly those derived from optical and infrared telescopes), it is crucial to incorporate PAAI maps as a complement to existing resources such as maps detailing cloud cover, humidity, and light pollution.

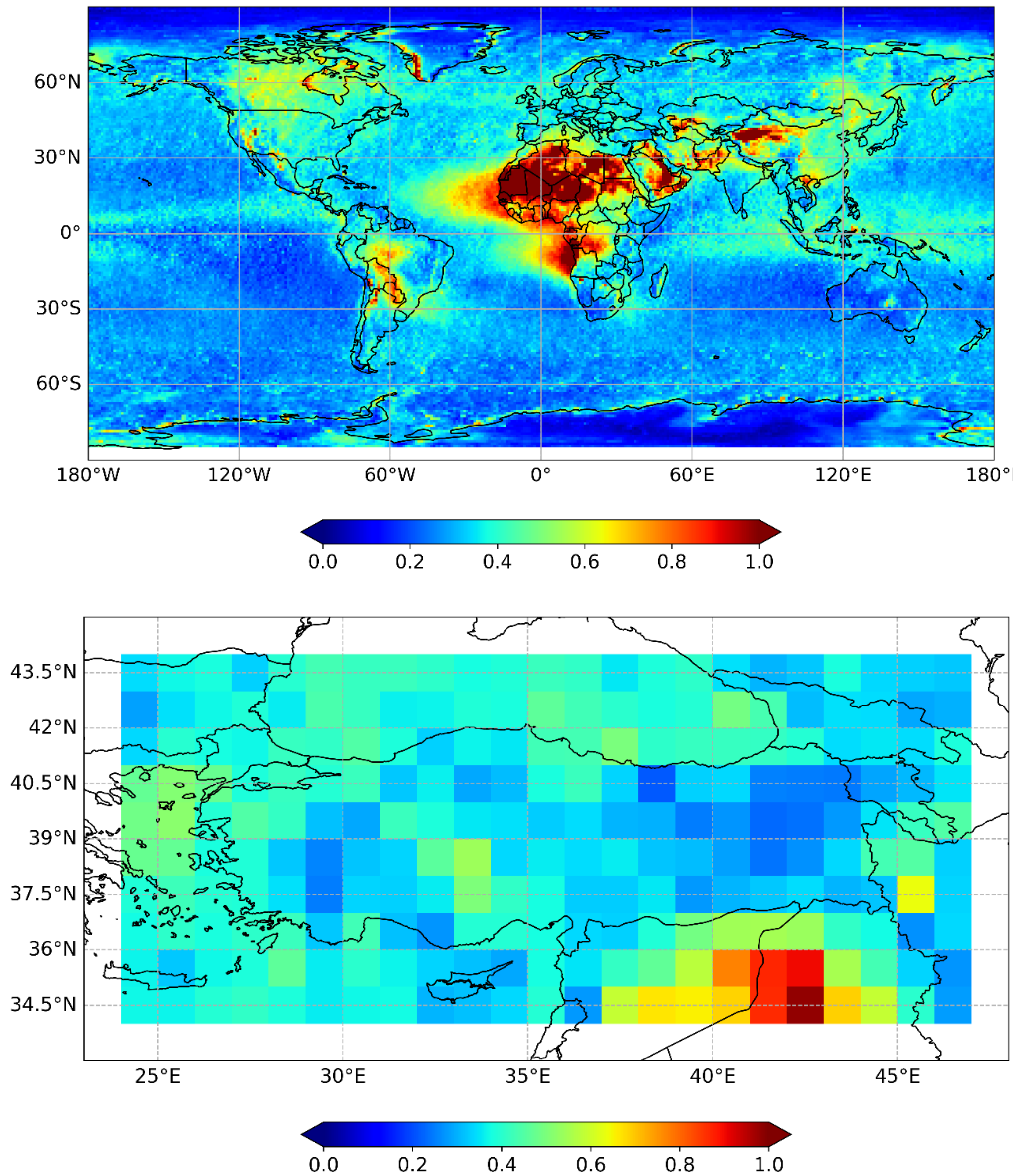

Figure 2 Global and Türkiye mean PAAI maps for 2024.

Table 3 Statistical values of the 2024 mean PAAI maps

	Minimum	Maximum	Mean	Median	Standart Deviation
Türkiye	0.21	0.98	0.39	0.37	0.11
Global	0.02	2.48	0.34	0.31	0.17

PAAI values are of critical importance in the context of optical and infrared observations, given that they serve as a reliable indicator of the extent to which the atmosphere is affected by absorbing aerosols. Upon examination of the PAAI map of Türkiye, it is evident that regions exhibiting low PAAI values (0.0 - 0.3) (indicated in blue and light blue) are particularly conducive to sky observation. Conversely, medium-level PAAI values (0.3 - 0.6) may, on occasion, give rise to certain challenges in the southern region of Central Anatolia, the eastern Mediterranean region, and the westernmost region of the Southeast. High PAAI (>0.6) values were observed in the region surrounding Şanlıurfa, Mardin, and the Syrian border, where dust transport and dense aerosols make the area unsuitable for optical observation. TUG has a light blue value of 0.2–0.3 on the map and is considered to be suitable in terms of atmospheric conditions. However, it is occasionally affected by Saharan dust. As illustrated DAG in the map, light blue and blue values ranging from 0.1 to 0.3 are indicative of relatively low intensity. The DAG site is advantageous in terms of aerosols and has a suitable atmospheric environment for optical and infrared observations. As demonstrated on the EUO map, there is an occurrence of moderate levels of aerosols in light blue and greenish (0.3 – 0.4) values. However, sea effect may result in rapid atmospheric cleaning at the site. The EUO site is generally considered suitable, although it should be noted that on certain days, the quality of observation may be reduced. As illustrated in the IsUO map, light blue values ranging from 0.2 to 0.3 are evident. COMUUO has light blue and green (0.3–0.4) values on the map. In summary, DAG can be classified as very good, TUG and COMUUO as good, and EUO and IsUO as moderate in terms of PAAI. The Southeastern Anatolia Region, particularly the Şanlıurfa–Mardin line, is considered to be at high risk with regard to PAAI. The presence of dust and local aerosols from Syria has been observed in this region. The central Black Sea and the east of Eastern Anatolia are notable for low PAAI, but meteorological conditions and cloudiness should also be considered in these regions. The global average PAAI value for 2024 is calculated as 0.34, which is lower than the 45-year long-term average of 0.38. However, the Türkiye average for 2024 is 0.39, which is nearly equivalent to the long-term global average.

The long-term monthly average graphs for observatories, Türkiye and the global values are presented in Figure 3, and the primary statistics associated with these data are provided in Table 4. An analysis of the graphs indicates that the highest aerosol values are generally observed in Türkiye, UZAYBİMER, COMUUO, IsUO and TUG sites. Conversely, the lowest aerosol values were observed in the EUO, Global, and DAG areas. Furthermore, the high values of the locations under consideration occurred approximately during the April-July period. It is evident that, due to the close proximity of Turkish terrain to deserts and the transportation of dust, high PAAI values are observed during the months when the deserts are active. While values at TUG were recorded at levels above the Türkiye average for the initial six months of the year, values at DAG were comparatively lower. The values of the DAG site exhibit a peak during the period from December to April, with a decrease in the other months.

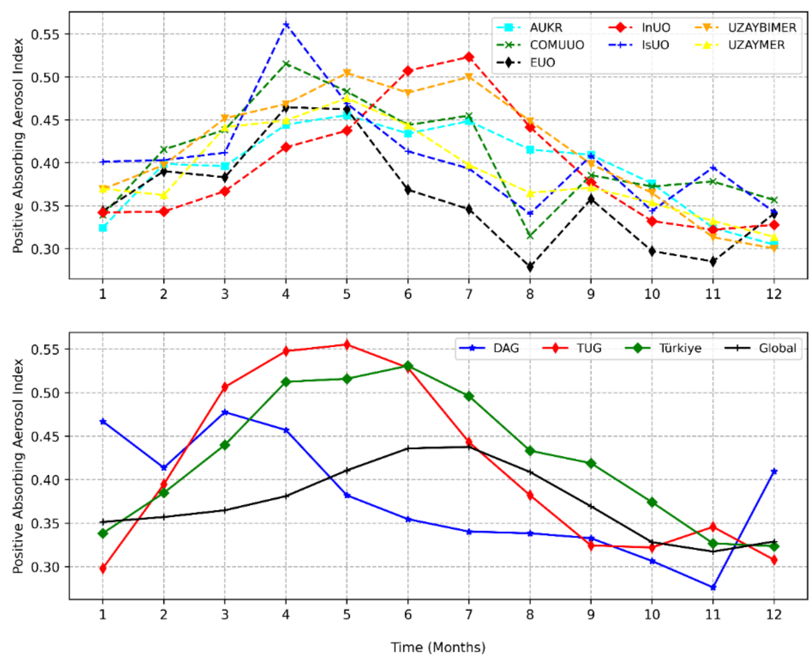

Figure 3 Long-term monthly mean PAAI values for the observatories.

Table 4 Statistical values of the long-term monthly mean PAAI.

Index / Site	Count	Mean	Std	Min	25%	50%	75%	Max
AUKR	12	0.39	0.05	0.30	0.36	0.40	0.44	0.46
COMUUO	12	0.41	0.06	0.32	0.37	0.40	0.45	0.52
DAG	12	0.38	0.07	0.28	0.34	0.37	0.42	0.48
EUO	12	0.36	0.06	0.28	0.33	0.35	0.39	0.46
InUO	12	0.39	0.07	0.32	0.34	0.37	0.44	0.52
IsUO	12	0.41	0.06	0.34	0.38	0.40	0.41	0.56
TUG	12	0.41	0.10	0.30	0.32	0.39	0.51	0.56
UZAYBIMER	12	0.42	0.07	0.30	0.37	0.42	0.47	0.50
UZAYMER	12	0.39	0.05	0.31	0.36	0.37	0.44	0.48
TUR	12	0.42	0.08	0.32	0.37	0.43	0.50	0.53
Global	12	0.37	0.04	0.32	0.35	0.37	0.41	0.44

(Std: Standard deviation, Min: Minimum, Max: Maximum)

Figure 4 shows the bar plots of long-term seasonal PAAI values for the sites and statistical values of the plots can also be seen in Table 5. For all study regions, high aerosol values are observed in spring and summer seasons and low aerosol values are observed in fall and winter seasons. In the spring period, high aerosol values were observed at TUG, COMUUO, IsUO and UZAYBIMER sites, while low aerosol values were observed at InUO, AUKR, DAG and EUO sites. During the summer period, high aerosol levels were recorded in the InUO, UZAYBIMER, TUG and AUKR sites, while low aerosol levels were observed in the DAG, EUO and IsUO sites. During autumn, EUO and DAG sites demonstrated low aerosol levels, while other locations exhibited comparable and lower values. During the winter period, the locations exhibited low and comparable values. The PAAI dataset provides important information for understanding regional and global aerosol distribution and monitoring air quality. Monthly and annual variations of aerosol levels in different regions of Türkiye are critical in determining the extent to which observations are affected by atmospheric disturbances. It shows in detail the annual and seasonal averages of aerosol concentrations in specific regions. High aerosol averages are associated with the mixing of desert dust into the atmosphere, especially in desert regions. The average values of observation points in Türkiye vary depending on local environmental and meteorological factors. This information is important for monitoring and managing air quality.

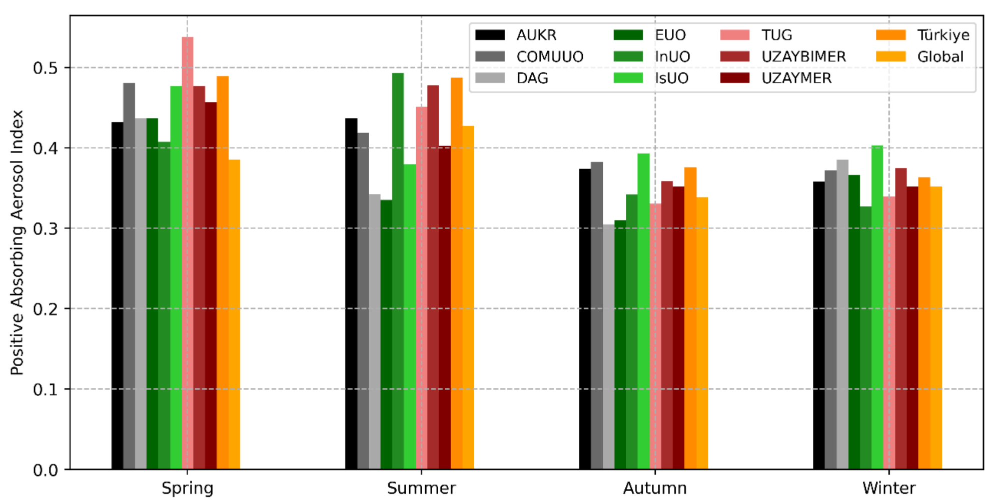

Figure 4 Long-term seasonally mean PAAI values for the observatories.

Table 5 Statistical values of the long-term seasonally mean PAAI.

Season / Site	Spring	Summer	Autumn	Winter
AUKR	0.43	0.44	0.37	0.36
COMUUO	0.48	0.42	0.38	0.37
DAG	0.44	0.34	0.30	0.39
EUO	0.44	0.34	0.31	0.37
InUO	0.41	0.49	0.34	0.33
IsUO	0.48	0.38	0.39	0.40
TUG	0.54	0.45	0.33	0.34
UZAYBIMER	0.48	0.48	0.36	0.37
UZAYMER	0.46	0.40	0.35	0.35
TUR	0.49	0.49	0.38	0.36
Global	0.39	0.43	0.34	0.35

Figure 5 shows the yearly mean temporal variations of absorbing aerosol values for Türkiye's major observatories, Türkiye, and the global. When the graphs in Figure 5 are analyzed, it can be seen that all PAAI values increase between 1979 and 2005, decrease between 2005 and 2010, and remain relatively stable after 2010. The annual average PAAI values for Türkiye range from 0.30 to 0.60 (1982 and 2001) and from 0.28 to 0.55 for the world (1986 and 2005). However, it can be seen from the graphs that Türkiye's average PAAI values are above the global average values. The reason for this is that dust is frequently transported from the large deserts around Türkiye (African and Middle Eastern deserts). An analysis of the annual PAAI values of the observatories indicates that high values were observed in UZAYBIMER, COMUUO, IsUO, and TUG sites, respectively, while low PAAI values were observed in EUO and DAG sites. When the values of the observatories and Türkiye are analyzed from the figure, it can be seen that the DAG values are generally below and parallel to the values of Türkiye. Values at TUG, on the other hand, exhibited a more fluctuating change over the years and were mostly above the Türkiye average.

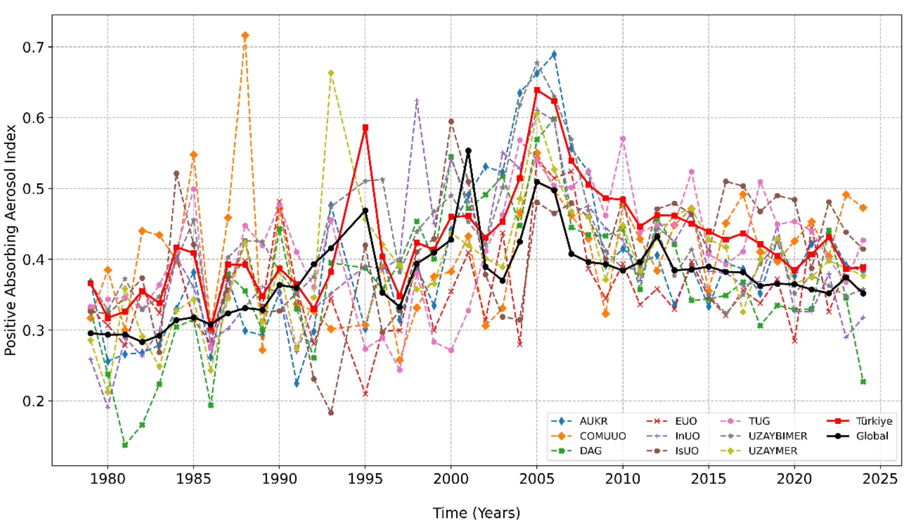

Figure 5 Yearly mean PAAI values for the observatories.

Seasonal decomposition is defined as the separation of time series data into trend, seasonal and residual components. Temporal data may depend on previous values, seasons and external factors. Figures 6 and 7 show the seasonal decomposition of monthly mean PAAI values for the observatories, Türkiye and Global. The graphs are ordered from top to bottom as original observation, trend, seasonal and residual components. A thorough examination of the PAAI values at DAG presented in the figure indicates the presence of a highly irregular structure within the DAG PAAI data. It appears that the level has remained relatively consistent since the 2000s. The present study has revealed an upward trend in the PAAI values at DAG between 1980 and 2005. Following 2005, a slight fluctuation is observed, with a more pronounced decrease evident after 2020. The seasonal component is quite distinct and exhibits a structure that repeats itself on an annual basis. The wave height is typically constant, exhibiting a consistent seasonal pattern on an annual basis. It is evident that the components under consideration are generally symmetrical and randomly distributed in the center (around zero). There are notable high deviations in some periods, especially in the 1990s and early 2010s. The DAG PAAI series has been observed to exhibit a distinct seasonal structure, characterized by an initial increase that extends until approximately 2005, following which a decline is initiated. The seasonal effects are constant and robust. It is possible to make similar evaluations of the values at DAG for other observatories, Türkiye and global PAAI values from Figures 6 and 7.

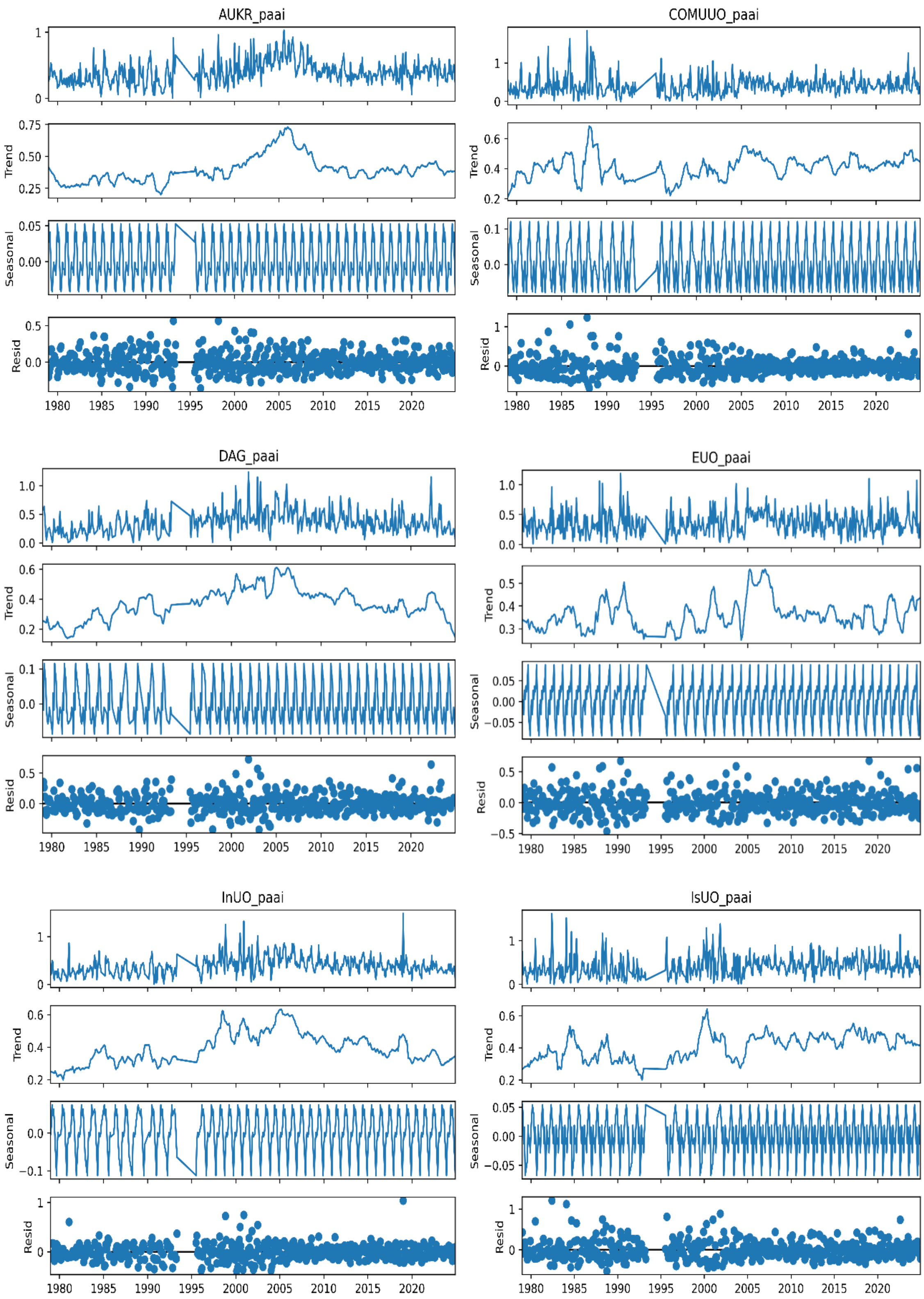

Figure 6 Seasonal decomposition of observatories -1

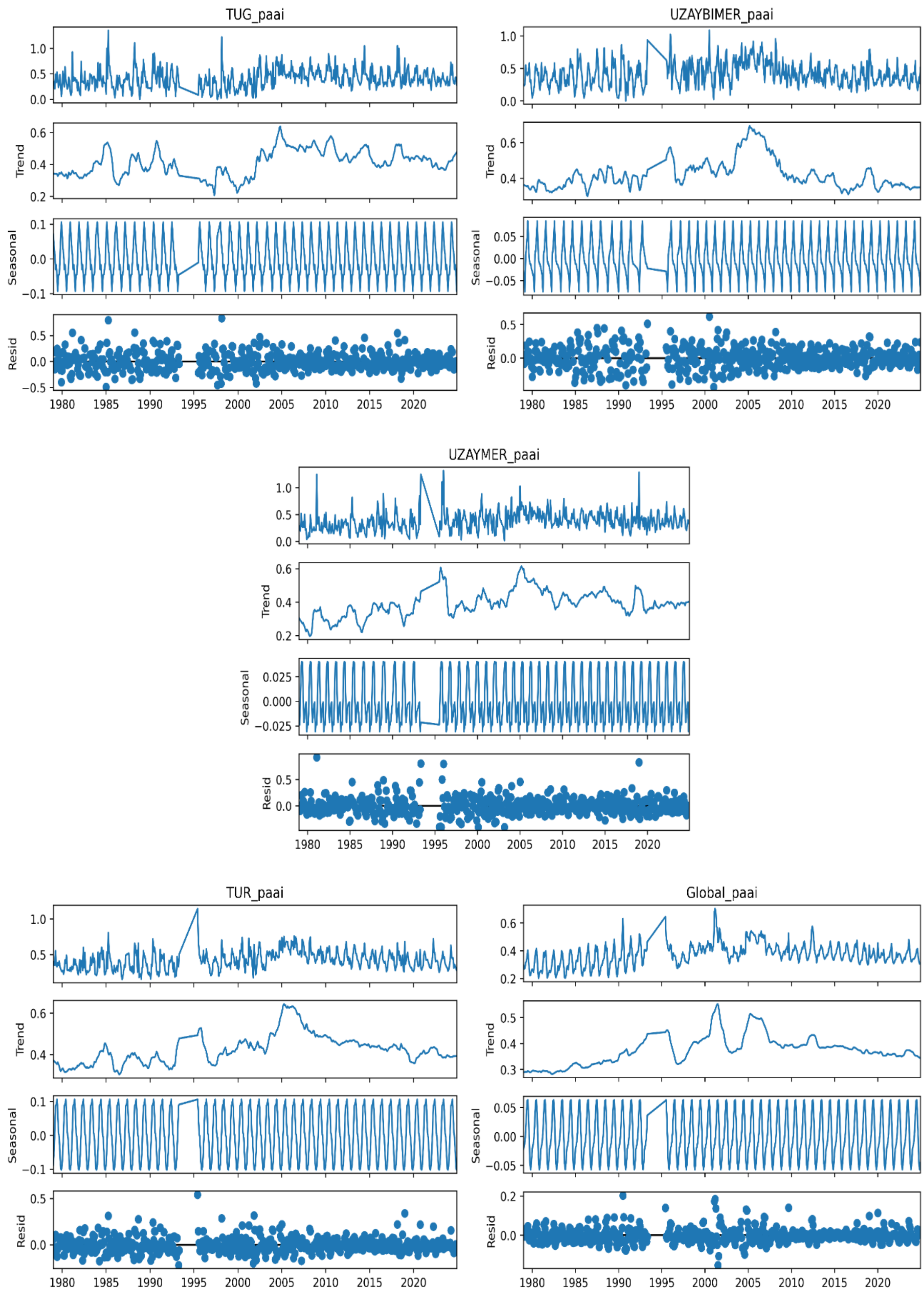

Figure 7 Seasonal decomposition of observatories -2

Conclusion

Türkiye and its major observatories are affected by dust transported from both local and distant sources. To determine the severity of this effect, we examine of absorbing aerosols for the ground-based astronomical observations in Türkiye by reviewing their spatial and temporal variability. The optimal conditions for ground-based astronomical observatories are the Atacama Desert in Chile, Hawaii, Namibia (where levels of PAAI are comparatively low), and the Canary Islands (where medium levels of PAAI occur, and occasional effects from Saharan dust may be experienced) and significant challenges include northern India, central Africa and eastern China for global scale. For the Türkiye scale, low PAAI values occur in high altitude areas, medium-level PAAI values (0.3 - 0.6) occur in the southern region of Central Anatolia, the eastern Mediterranean region, and the westernmost region of the Southeast and high PAAI (>0.6) values are observed in the region surrounding Şanlıurfa, Mardin, and the Syrian border. DAG site can be classified as very good, TUG and COMUUO as good, and EUO and IsUO as moderate in terms of PAAI. The global average PAAI value for 2024 is calculated as 0.34, which is lower than the 45-year long-term average of 0.38. However, the Türkiye average for 2024 is 0.39, which is nearly equivalent to the long-term global average. The long-term highest monthly aerosol values are generally observed in UZAYBİMER, COMUUO, IsUO and TUG sites, respectively. Conversely, the lowest aerosol values were observed in the EUO, and DAG areas. The long-term seasonal PAAI values for these sites indicate that high aerosol levels are observed in spring and summer seasons, while low aerosol levels are recorded in autumn and winter seasons. PAAI values increased between 1979 and 2005, decreased between 2005 and 2010, and remain relatively stable after 2010 for the all sites. PAAI values at DAG indicate the presence of a highly irregular structure. The present study has revealed an upward trend in the PAAI values at DAG between 1980 and 2005. Following 2005, a slight fluctuation is observed, with a more pronounced decrease evident after 2020. The seasonal component is quite distinct and exhibits a structure that repeats itself on an annual basis.

Hakem Değerlendirmesi: *Dış bağımsız.*
Yazar Katkıları: *Konsept – SA, FP, KK; Tasarım - SA, FP, KK; Denetim - SA, FP, KK ; Kaynaklar - SA; Malzemeler - SA, FP, KK; Veri Toplama ve/veya İşleme - SA, FP, KK; Analiz ve/veya Yorum - SA, FP, KK; Literatür Taraması - SA, FP, KK; Yazma - SA, FP, KK; Eleştirel İnceleme - SA, FP, KK; Diğer – SA, FP, KK*
Çıkar Çatışması: *Yazarlar, çıkar çatışması olmadığını beyan etmiştir.*
Finansal Destek: *Yazarlar bu çalışma için finansal destek almadıklarını beyan etmişlerdir.*
Peer-review*: Externally peer-reviewed.*
Author Contributions: *Concept – SA, FP, KK; Design – SA, FP, KK; Supervision – SA, FP, KK; Resources – SA; Materials – SA, FP, KK; Data Collection and/or Processing – SA, FP, KK; Analysis and/or Interpretation – SA, FP, KK; Literature Review – SA, FP, KK; Writing – SA, FP, KK; Critical Review – SA, FP, KK; Other – SA, FP, KK.*
Conflict of Interest: *The authors have no conflicts of interest to declare.*
Financial Disclosure: *The authors declared that this study has received no financial support.*

References

Aslanoğlu, S. Y., Proestakis, E., Gkikas, A., Güllü, G., & Amiridis, V. (2022). Dust climatology of Turkey as a part of the Eastern Mediterranean Basin via 9-year CALIPSO-derived product. *Atmosphere*, 13(5), 733. https://doi.org/10.3390/atmos13050733

Balarabe, M., Abdullah, K., Nawawi, M., & Khalil, A. E. (2016). Monthly temporal-spatial variability and estimation of absorbing aerosol index using ground-based meteorological data in Nigeria. *Atmospheric and Climate Sciences*, 6(03), 425. https://doi.org/10.4236/acs.2016.63035

Cavazzani, S., Ortolani, S., Bertolo, A., Binotto, R., Fiorentin, P., Carraro, G., & Zitelli, V. (2020). Satellite measurements of artificial light at night: Aerosol effects. *Monthly Notices of the Royal Astronomical Society*, 499(4), 5075–5089. https://doi.org/10.1093/mnras/staa3157

Gan, Y., Zhang, Z., Liu, F., Chen, Z., Guo, Q., Zhu, Z., & Ren, Y. (2024). Analysis of characteristics and changes in three-dimensional spatial and temporal distribution of aerosol types in Central Asia. *Science of The Total Environment*, 927, 172196. https://doi.org/10.1016/j.scitotenv.2024.172196

Holben, B. N., Eck, T. F., Slutsker, I. A., Tanre, D., Buis, J. P., Setzer, A., ... & Smirnov, A. (1998). AERONET—A federated instrument network and data archive for aerosol characterization. *Remote Sensing of Environment*, 66(1), 1-16. https://doi.org/10.1016/S0034-4257(98)00031-5

Isik, A. G., Aslanoğlu, S. Y., & Güllü, G. (2024). Long-term evaluation of aerosol optical properties in the Levantine region: A comparative analysis of AERONET and Aqua/MODIS. *Remote Sensing*, 16(14), 2651. https://doi.org/10.3390/rs16142651

Jackson, J. M., Liu, H., Laszlo, I., Kondragunta, S., Remer, L. A., Huang, J., & Huang, H. C. (2013). Suomi-NPP VIIRS aerosol algorithms and data products. *Journal of Geophysical Research: Atmospheres*, 118(22), 12-673. https://doi.org/10.1002/2013JD020449

Jiadan, D., Liqiao, T., Fang, C., Xiaobin, C., Xiaoling, C., Qiangqiang, X., & Xinghui, X. (2023). Spatio-temporal variations of aerosol optical depth over Ukraine under the Russia-Ukraine war. *Atmospheric Environment*, 314, 120114. https://doi.org/10.1016/j.atmosenv.2023.120114

Kocifaj, M., & Bará, S. (2020). Night-time monitoring of the aerosol content of the lower atmosphere by differential photometry of the anthropogenic skyglow. *Monthly Notices of the Royal Astronomical Society: Letters*, 500(1), L47–L51. https://doi.org/10.1093/mnrasl/slaa181

Kooreman, M. L., Stammes, P., Trees, V., Sneep, M., Tilstra, L. G., de Graaf, M., ... & Veefkind, J. P. (2020). Effects of clouds on the UV Absorbing Aerosol Index from TROPOMI. *Atmospheric Measurement Techniques Discussions*, 2020, 1-31. https://doi.org/10.5194/amt-13-6407-2020

Levy, R. C., Remer, L. A., Mattoo, S., Vermote, E. F., & Kaufman, Y. J. (2007). Second-generation operational algorithm: Retrieval of aerosol properties over land from inversion of Moderate Resolution Imaging Spectroradiometer spectral reflectance. *Journal of Geophysical Research: Atmospheres*, 112(D13). https://doi.org/10.1029/2006JD007811

Liu, J., Ding, J., Li, L., Li, X., Zhang, Z., Ran, S., Ge, X., Zhang, J., Wang, J., 2020. Characteristics of aerosol optical depth over land types in central Asia. Science of the Total Environment 727, 138676. https://doi.org/10.1016/j.scitotenv.2020.138676

Mikhalev, A. V., Tashchilin, M. A., & Sakerin, S. M. (2019). Effect of atmospheric aerosol on ground-based airglow observations. *Atmospheric and Oceanic Optics*, 32, 410–415. https://doi.org/10.1134/S1024856019040109

Osgouei, P. E., & Kaya, Ş. (2023). A comprehensıve analysıs of the spatıo-temporal varıatıon of satellıte-based aerosol optıcal depth ın marmara regıon of turkıye durıng 2000–2021. *The Int. Archives of the Photogrammetry, Remote Sensing and Spatial Information Sciences*, 48, 509-514. https://doi.org/10.5194/isprs-archives-XLVIII-M-1-2023-509-2023

Ozdemir, E., Tuygun, G. T., & Elbir, T. (2020). Application of aerosol classification methods based on AERONET version 3 product over eastern Mediterranean and Black Sea. *Atmospheric Pollution Research*, 11(12), 2226-2243. https://doi.org/10.1016/j.apr.2020.06.008

Remer, L. A., Kaufman, Y. J., Tanré, D., Mattoo, S., Chu, D. A., Martins, J. V., ... & Holben, B. N. (2005). The MODIS aerosol algorithm, products, and validation. *Journal of the Atmospheric Sciences*, 62(4), 947-973. https://doi.org/10.1175/JAS3385.1

Sánchez, S. F., Aceituno, J., Thiele, U., Pérez-Ramírez, D., & Alves, J. (2007). The night sky at the Calar Alto Observatory. *Publications of the Astronomical Society of the Pacific*, 119(860), 1186–1198. https://doi.org/10.1086/522378.

Shaylor, M., Brindley, H., & Sellar, A. (2022). An evaluation of two decades of aerosol optical depth retrievals from MODIS over Australia. *Remote Sensing*, 14(11), 2664. https://doi.org/10.3390/rs14112664

Tariq, S., Shahzad, H., Mehmood, U., & Haq, Z. U. (2023). Linear and wavelet analysis of aerosol optical depth (AOD) and prevailing meteorological factors during summer (2003–2016) over Turkey using Remote Sensing. *Air Quality, Atmosphere & Health*, 16(12), 2509-2528. https://doi.org/10.1007/s11869-023-01422-0

Tilstra, L. G., Tuinder, O. N., & Stammes, P. (2010, September). GOME-2 absorbing aerosol index: Statistical analysis, comparison to GOME-1 and impact of instrument degradation. *The 2010 EUMETSAT Meteorological Satellite Conference* (p. 57). Retrieved from https://www-cdn.eumetsat.int/files/2020-04/pdf_conf_p57_s4_12_tilstra_p.pdf

Tutsak, E., & Koçak, M. (2020). Optical and microphysical properties of the columnar Aerosol burden over the Eastern Mediterranean: Discrimination of Aerosol types. *Atmospheric Environment*, 229, 117463. https://doi.org/10.1016/j.atmosenv.2020.117463

Tuygun, G. T., & Elbir, T. (2020). Long-term temporal analysis of the columnar and surface aerosol relationship with planetary boundary layer height at a southern coastal site of Turkey. *Atmospheric Pollution Research*, 11(12), 2259-2269. https://doi.org/10.1016/j.apr.2020.09.008

Tuygun, G. T., & Elbir, T. (2023). Long-term spatiotemporal variation in atmospheric aerosol properties over Türkiye based on MERRA-2 reanalysis data: aerosol classification based on city type. *Environmental Science and Pollution Research*, 31(28), 40655-40668. https://doi.org/10.1007/s11356-023-27920-3

Tuygun, G. T., & Elbir, T. (2024). Comparative analysis of CAMS aerosol optical depth data and AERONET observations in the Eastern Mediterranean over 19 years. *Environmental Science and Pollution Research*, 31(18), 27069-27084. https://doi.org/10.1007/s11356-024-32950-6

Verma, S., Prakash, D., Soni, M., & Ram, K. (2019). Atmospheric aerosols monitoring: Ground and satellite-based instruments. In Advances in environmental monitoring and assessment. *IntechOpen*. https://doi.org/10.5772/intechopen.80489.

Yoshioka, M., Mahowald, N., Dufresne, J. L., & Luo, C. (2005). Simulation of absorbing aerosol indices for African dust. *Journal of Geophysical Research: Atmospheres*, 110(D18). https://doi.org/10.1029/2004JD005276

Zhang, H. H., Liu, X. W., Yuan, H. B., Zhao, H. B., Yao, J. S., Zhang, H. W., & Xiang, M. S. (2013). Atmospheric extinction coefficients and night sky brightness at the Xuyi Observation Station. *Research in Astronomy and Astrophysics*, 13(4), 490–502. https://doi.org/10.1088/1674-4527/13/4/010